uOttawa

L'Université canadienne
Canada's university

Biomass Fast Pyrolysis Fluidized Bed Reactor: Modelling and Experimental Validation

Johnny Matta

Thesis Submitted to the Faculty of Graduate and Postdoctoral Studies in Partial Fulfillment of the Requirements for the Degree

M.A.Sc. in Chemical Engineering

Department of Chemical and Biological Engineering

Faculty of Engineering

University of Ottawa

Abstract

Of the many thermochemical conversion pathways for utilizing biomass as a renewable energy source, fast pyrolysis is a promising method for converting and upgrading carbonaceous feedstocks into a range of liquid fuels for use in heat, electricity and transportation applications. Experimental trials have been carried out to assess the impact of operational parameters on process yields. However, dealing with larger-scale experimental systems comes at the expense of lengthy and resource-intensive experiments. Luckily, the advances in computing technology and numerical algorithm solvers have allowed reactor modelling to be an attractive opportunity for reactor design, optimization and experimental data interpretation in a cost-effective fashion. In this work, a fluidized bed reactor model for biomass fast pyrolysis was developed and applied to the Bell's Corners Complex (BCC) fluidized bed fast pyrolysis unit located at NRCan CanmetENERGY (Ottawa, Canada) for testing and validation. The model was programmed using the Microsoft Visual Basic for Applications software with the motivation of facilitating use and accessibility as well as minimizing runtime and input requirements. The application of different biomass devolatilization schemes within the model was conducted, not only for biomass fast pyrolysis product quantity but also liquid product composition (quality), to examine the effect of variable reaction kinetic sub-models on product yields. The model predictions were in good agreement with the results generated from the experimental work and mechanism modifications were proposed which further increased the accuracy of model predictions. Successively, the formulation of the modelled fluid dynamic scheme was adapted to study the effect of variable hydrodynamic sub-models on product yields for which no significant effect was observed. The work also looked into effect of the dominant process variables such as feedstock composition, bed temperature, fluidizing velocity and feedstock size on measurable product outputs (bio-oil, gas and biochar) and compared the results to those generated from the experimental fast pyrolysis unit. The ideal parameters for maximizing bio-oil yield have been determined to be those which: minimize the content of lignin and inorganic minerals in the feedstock, maintain the dense-bed temperature in a temperature range of 450-520 ºC, maximize the fluidization velocity without leading to bed entrainment, and limit the feedstock particle size to a maximum of 2000 μm.

Résumé

Parmi les nombreuses voies de conversion thermochimique pour l'utilisation de la biomasse comme source d'énergie renouvelable, la pyrolyse rapide est une méthode prometteuse pour la conversion et la mise à niveau des matières premières carbonées dans une gamme de combustibles liquides pour l'utilisation dans des applications thermiques, d'électricité et de transport. Des essais expérimentaux ont été effectués pour évaluer l'impact des paramètres opérationnels sur le rendement des procédés. Toutefois, l'expérimentation avec des systèmes à grande échelle se fait au détriment des expériences longues et considérables en ressources. Heureusement, les progrès de la technologie informatique et de solveurs d'algorithmes numériques ont permis à la modélisation de devenir un outil indispensable pour la conception de réacteurs, l'optimisation et l'interprétation des données expérimentales d'une manière rentable. Dans ce travail, un modèle de réacteur à lit fluidisé pour la pyrolyse rapide de la biomasse a été développé et appliqué au système expérimental à lit fluidisé de pyrolyse rapide au complexe de Bells Corners, situé à RNCan CanmetÉNERGIE (Ottawa, Canada) pour valider les essais. Le modèle a été programmé en se servant du logiciel Microsoft Visual Basic pour Applications avec la motivation de faciliter son utilisation et son accessibilité ainsi que de minimiser les exigences d'exécution et de l'entrée des données. La mise en œuvre des différents schémas de dévolatilisation de la biomasse au sein du modèle a été menée, pour déterminer non seulement la quantité de produit de la pyrolyse rapide de la biomasse et la composition du produit liquide (qualité) mais aussi pour examiner l'effet des variations des sous-modèles de cinétiques de réaction sur les rendements des produits. Les prédictions du modèle concordent très bien avec les résultats générés par les travaux expérimentaux et des modifications du mécanisme ont été proposées ce qui a davantage augmenté la précision des prédictions du modèle. Successivement, la formulation du schéma dynamique du fluide modélisé a été adaptée afin d'étudier l'effet des variations des sous-modèles hydrodynamiques sur les rendements des produits pour lesquels aucun effet significatif n'a été observé. Le travail a examiné l'effet des variables de procédés telles que la composition des matières premières, la température du lit, la vitesse de fluidisation et la taille des matières premières sur le rendement des produits (bio-huile, gaz et biocharbon) et a comparé les résultats à ceux générés par le système expérimental de pyrolyse rapide. Les paramètres idéaux pour maximiser le rendement en bio-huile sont été ceux qui: minimisent la teneur en lignine et en minéraux inorganiques dans les matières premières, maintiennent la

température du lit dans une plage de température entre 450-520 ºC, maximisent la vitesse de fluidisation sans conduire à l'entraînement du lit, et limitent la taille d'une particule de matière première à un maximum de 2000 µm.

Acknowledgments

I would like to express my sincere gratitude to my supervisors Dr. Poupak Mehrani (University of Ottawa) and Dr. Jules Thibault (University of Ottawa) for their incredible amount of support and guidance provided throughout this study. Their work ethic and integrity, has thought me a lot about self-respect and professionalism. Thank you very much for all your hard work and commitment; this work would not have been possible without you.

I would also like to thank my supervisors in the Bioenergy Research Group at NRCan CanmetENERGY's Bells Corner Complex, Dr. Peter Gogolek and Benjamin Bronson for their expertise and assistance. Peter, I would like to thank you for your recommendations with setting up the models. Benjamin, I would like to thank you for all your hard work in helping with experiments, data collection, sample analysis and document preparation. Your cooperation with experiments and companionship during conferences made this study an enjoyable experience. Additionally, I would like to thank all of the coop students that assisted with the experiments.

I would like to gratefully acknowledge all of the analytical services provided by the characterization laboratories at CanmetENERGY's Bells Corner Complex as well as FPInnovation's Point-Claire branch.

A special thanks to Mark Goodchild for his help in testing and validating part of the model for his undergraduate thesis.

This work was only possibly with financial assistance from the Natural Sciences and Engineering Research Council of Canada (NSERC) and Ontario Graduate Scholarship (OGS) as well as NRCan CanmetENERGY (Ottawa, Canada) and The University of Ottawa.

Finally, I would like to thank all of my friends and family for their love and encouragement.

Table of Contents

List of Figures

List of Tables

Nomenclature

Symbol	Definition	Units
a	Ranz-Marshall correlation constant	-
A_c	Cross-sectional area of reactor	m^2
a_i	Surface-to-Volume ratio for particle "i"	m^2/ m^3
A_0	"Catchment Area" – Area of distributor plate per orifice	m^2
Ar	Archimedes number	-
b	Ranz-Marshall correlation constant	-
C_D	Drag coefficient	-
C_{iB}	Concentration of gas component i in bubble phase	kg/m^3 bubble
C_{ie}	Concentration of gas component i in emulsion phase	kg/m^3 emulsion gas
C_{ib}	Concentration of gas component i in biomass phase	kg/m^3 biomass
Cp_i	Heat capacity of component "i"	J/kg/K
D	Diffusivity	m^2/s
d_B	Diameter of sphere having same volume as bubble	m
D_r	Diameter of reactor	m
d_s	Diameter of bed material	m
d_p	Diameter of bed particle	m
E_a	Activation energy	kJ/mol
e_{sb}	Effective emissivity	-
e_b	Emissivity of biomass	-
e_s	Emissivity of sand	-
g	Gravitational constant	m/s^2
h	Height above distributor plate	m
H	Fluidized bed height	m
H_{mf}	Fluidized bed height at minimum fluidization	m
h_i	Heat transfer coefficient for particle "i"	$W/m^2/K$
h_r	Heat transfer by radiation	W/m^2
ΔH_{rxn}	Heat of reaction	J/kg
k_i	Reaction rate constant for reaction "i"	1/s
k_g	Thermal conductivity of gas	W/m/K
K_{BE}	Bubble-emulsion mass exchange coefficient	1/s
$\dot{m}_{bio}$	Mass flow of biomass	kg/s
M_s	Mass of sand per cell	
n	Richardson-Zaki coefficient	-
ΔP_{bed}	Pressure differential in bed	Pa
Pr	Prandtl number	-
$\dot{Q}$	Heat flow by band heaters	J/s
R	Ideal gas constant	J/mol/K
R_{iB}	Rate of reaction of gas-gas phase reaction "i" within bubble	kg/m^3 bubble/ s
R_{ie}	Rate of reaction of gas-gas phase reactions "i" within emulsion	kg/m^3 emulsion/ s
R_{ib}	Rate of reaction of solid phase reaction "i"	kg/m^3 biomass/ s
Re_i	Particle "i" Reynolds number	-

$\widehat{S_1}$	Time-averaged volume of bubble segment	m^3
S_2	Volume of cell	m^3
t	Time	s
T_{bio}	Temperature of biomass	K
T_{gas}	Temperature of gas	K
T_{sand}	Temperature of sand	K
U	Superficial gas velocity	m/s
U_B	Bubble velocity	m/s
U_i	Velocity of biomass	m/s
U_t	Terminal velocity	m/s
U_{br}	Rise velocity of single bubble	m/s
U_{mf}	Minimum fluidization velocity	m/s
U_{tc}	Corrected terminal velocity	m/s
V	Volume of cell	m^3
V_b	Volume of biomass particle	m^3
Δz	Height of cell	m
ρ_b	Biomass particle density	kg/m^3
ρ_g	Gas density	kg/m^3
ρ_s	Solids particle density	kg/m^3
ε_b	Volume fraction of biomass	m^3 biomass/ m^3 cell
ε_B	Volume fraction of bubble	m^3 bubble/ m^3 cell
ε_e	Volume fraction of emulsion	m^3 emulsion/ m^3 cell
ε_s	Volume fraction of bed material	m^3 bed material/ m^3 cell
ε_{mf}	Minimum fluidization voidage	-
ϕ	Particle sphericity	-
γ	Velocity fraction for biomass particles	-
μ_g	Gas viscosity	Pa·s
σ	Stefan-Boltzmann constant	$W/m^2/K^4$

Chapter 1: Introduction

1.1. Biomass for Energy and Chemicals

Since the beginning of the industrial age, worldwide energy needs has largely been supplied from non-renewable sources such as oil, coal, peat, shale and natural gas. The dependence on fossil fuels has affected virtually every aspect of the economy and is only rising with the rapid increase in global primary energy consumption. In fact, the U.S. Energy Information Administration has projected that the world energy consumption will grow by 48 % by the year 2040 [1]. Accordingly, the increase in consumption has led to concerns of fuel reserve depletion. With the recent trend in reserves-to-production ratio presented in Figure 1, the oil, coal and natural gas reserves have been estimated to be sufficient to meet up to 50.7, 114 and 52.8 years of global production, respectively, whilst only considering the current energy consumption rate [2].

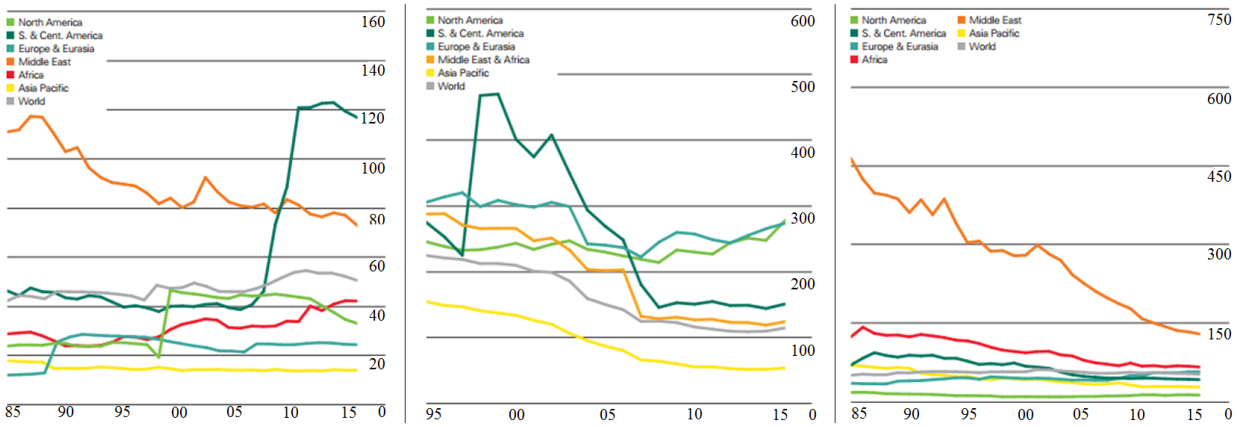

Figure 1: Yearly Global Fossil Fuel Reserves-to-Production Ratios for oil, coal and natural gas (excluding gas hydrates), respectively [2].

In addition, there has been much controversy around the environmental impact of fossil fuels including: climate change, air and water pollution, oil spills and acid rain. The most debated impact is the release of smog-causing pollutants and greenhouse gases which are believed to be linked to global warming. At the global scale, the sum of carbon emissions have increased by over 90 % since 1970, with those originating from fossil fuel combustion and industrial processes contributing to over 78 % of the increase [3]. Similarly, the release of other

by-products such as nitrous oxide, fluorinated gases and mercury have also increased, which has led to a significant need in finding cleaner and sustainable alternatives for energy production.

Within the current developments in renewable energy technologies, the exploitation of the energy stored in biomass to produce electricity, heat and biofuels is proving to be a promising alternative. Biomass is a biological resource derived from the carbonaceous waste of various human and natural activities [4]. Several types of biomass exist, the most common of which are: forestry crops and residues (wood, bark), agriculture crops and residues (straw, stover), animal by-products, sewage and municipal solid waste. Bioenergy generated from biomass offers several advantages over energy produced from fossil sources. For one thing, living biomass consumes carbon as it grows and releases carbon in the exploitation process, resulting in an ideal carbon-neutral cycle. Secondly, utilizing biomass for bioenergy is a good way to manage the disposal of materials that would otherwise be considered as waste. In addition, given its vast geographic distribution, biomass resources are readily available in rural and urban areas which provide appreciable employment opportunities as well as promote the sustainability of biomass conversion technologies. Just as biomass can substitute fossil fuels for energy production, it (and its by-products) can also provide a renewable alternative for industrial products. These bio-based products include foams, plastics, fertilizers, lubricants and speciality chemicals.

As shown in Figure 2, biomass currently contributes to over 10 % of the world's primary energy consumption making it the 4th largest contributor behind coal, oil, and natural gas.

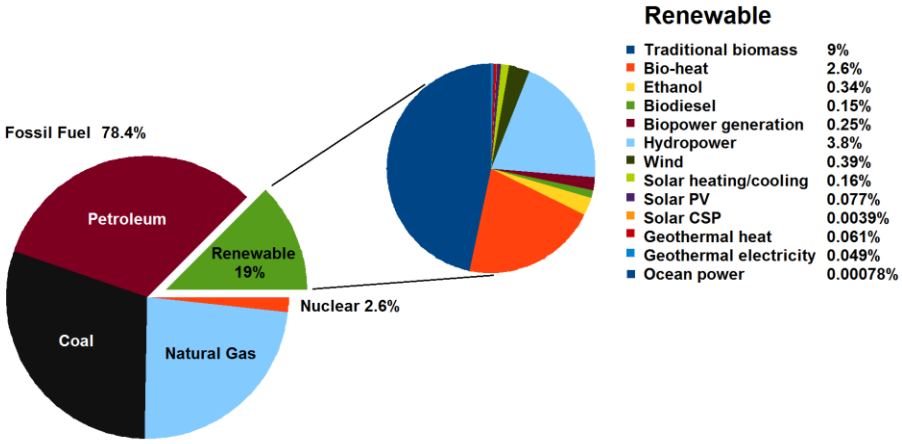

Figure 2: Total World Primary Energy Consumption Sources [3]

With its large landmass and active forest and agricultural industries, Canada is one of the countries that offer great potential for renewable energy resources. Presently, biomass is its third largest renewable source for power generation and bioenergy is the second most important form of renewable energy [5]. Specifically, the main source of biomass is industrial wood waste from the pulp and paper industry. In the beginning of 2015, Canada had 70 bioenergy power plants built around the use of woody biomass with a total capacity of 2043 megawatts [5].

While the long-term advantages of replacing fossil fuels with biomass in energy production can be quite rewarding, there exists a few limitations such as:

- The low energy density of biomass feedstocks
- The large variability in resources and supply
- The cost of transportation, storage, and handling systems
- Costly initial investments of conversion processes
- Difficult product purification and upgrading

Despite the latter, Canada remains of 17 countries participating in the International Energy Agency bioenergy research activities to improve biomass conversion development and deployment [5].

1.2. Thermochemical Conversion of Biomass

Converting biomass into bioenergy and fuels can be accomplished in several ways. The most common conversion methods are divided into two categories: biochemical pathways and thermochemical pathways. Biochemical conversion technologies, such as anaerobic digestion and fermentation, involve the use of microorganisms and enzymes to breakdown the structure of the biomass into gas and liquid products. However, with the various challenges faced to achieve high efficiencies such as developing reliable genetically modified microorganisms, reducing fermentation inhibitor formation during feedstock pre-treatment, and reducing the fraction of non-holocellulosic material, thermochemical conversion processes have been attractive alternatives for lignocellulosic biomass. Thermochemical conversion involves deconstructing biomass with controlled heating and/or oxidation and potentially upgrading the resulting

intermediates with the help of catalysts [6]. Some of the most common conversion processes are presented in Figure 3.

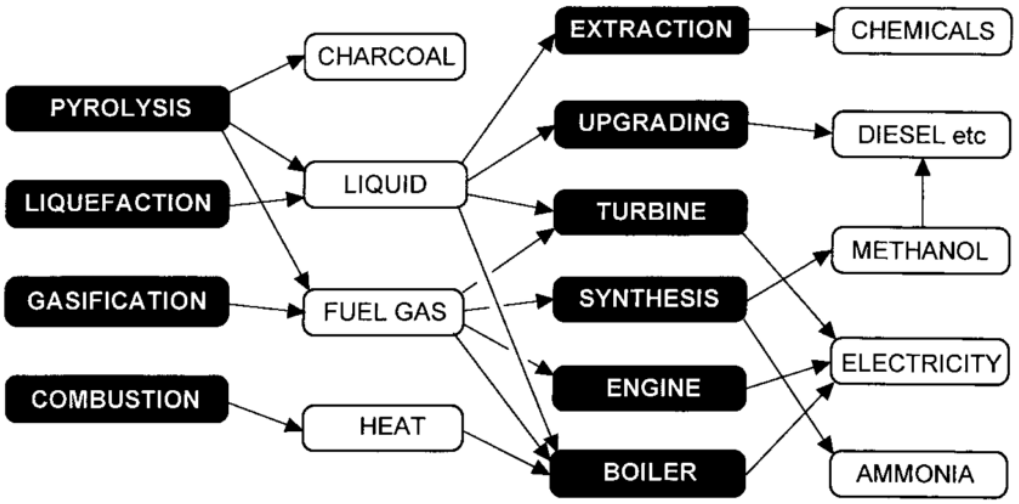

Figure 3: Different Biomass Thermochemical Conversion Pathways [7]

Each of the technologies are configured to produce either gaseous (fuel gas), liquid (bio-oil) or solid (biochar) products which may be further progressed into heating, power generation, or fuel synthesis applications. For the production of gaseous products, gasification is most commonly practiced. Biomass gasification yields the gaseous product via the incomplete combustion of biomass with a gasifying medium such as air, oxygen, steam, or carbon dioxide at elevated temperatures (ranging from 600 °C to 1100 °C). The producer gas is a mixture of a number of non-condensable components such as CO, CO_2, H_2 and CH_4. Gasification significantly increases the opportunities for using biomass as an energy source as compared to direct combustion since the producer gas can be used for a much greater range of purposes [8]. For instance, it can be upgraded to syngas for use in internal combustion engines, can be used as a substitute for furnace oil in direct heat applications and can be catalytically upgraded to produce, in an economically viable way, specialty chemicals such as methanol – an extremely attractive chemical which is useful both as fuel for heat engines as well as chemical feedstock for industries [9]. In addition, gasification producer gases can take advantage of advanced turbine designs and heat-recovery steam generators to achieve high energy efficiency [10].

In hopes of facilitating transportation and storage, a liquid product is desired. Furthermore, liquid products offer the advantage of supporting drop-in fuel applications. With

the increase in mandates for liquid biofuel production such as the US Renewable Fuel Standard requiring roughly 20 billion gallons of biofuel to be produced using cellulosic or advanced cellulosic biomass, there is a great incentive for generating liquid products [6]. For the production of liquid intermediates, liquefaction and fast pyrolysis are the methods used. The pyrolysis platform for bio-oil generation is quite well developed and has a great potential to leverage existing oil refinery infrastructure. Through liquefaction, such as hydrothermal liquefaction, the goal is to maximize liquid yields and quality than what is obtained with pyrolysis. Though, the process requires very high pressures, specific catalysts and is in relatively early stages of development.

1.2.1. Pyrolysis

Among the listed thermochemical conversion technologies exists pyrolysis. In pyrolysis, the biomass is heated in the absence of oxygen to (i) release trapped moisture, a phenomenon called drying and (ii) release organic volatiles, a phenomenon which is called devolatilization. The type of pyrolysis process depends on the heating rate of the biomass. In slow pyrolysis, the biomass is heated at low rates (5-100 °C/min), moderate temperatures and long residence time to maximize the yield of biochar, which are the solid carbonaceous remnants of biomass after devolatilization. However, to ultimately produce a liquid product, fast pyrolysis must be used. In fast pyrolysis, four conditions should be met [11]:

1) High heat transfer rates in reaction zone (up to 1000 °C/min)
2) Reactor temperature between 400-500 °C
3) Short vapour product residence time in reactor (typically below 2 seconds)
4) Rapid quenching of vapour phase products

The fast pyrolysis of lignocellulosic biomass, which is mildly endothermic, produces a 2nd generation bio-crude termed pyrolysis oil (or bio-oil), a heterogeneous oil mixture high in oxygen content. The bio-oil is made up of different components such as sugars and anhydrosugars, carbonyls and hydroxycarbonyls, acids, phenols and pyrolytic lignins [12]. With further treatment, such as hydroprocessing, separation and fractionation, the oil may be upgraded into a finished fuel suitable for a wide variety of applications including biofuels (naphtha or diesel) and biomaterials. Specifically, chemicals found in the bio-oil can be extracted and used

for food flavourings, resins, agri-chemicals, and fertilizers [7]. The bio-crude itself can be used in modified boilers, furnaces, engines and turbines for power generation. However, the performance achieved is based on the quality of bio-oil - which is heavily dependent on the type of feedstock. Typically, 60-75 wt% of the feedstock is converted into bio-oil which can have a volumetric energetic density of up to 20 times higher than the original biomass [13]. Table 1 presents typical characteristics and properties for woody biomass derived pyrolysis oil.

Table 1: Standard Physical Characteristics and Properties of Pyrolysis Oil [14]

Appearance	• Pyrolysis oil typically is a dark brown free flowing liquid • The colour can be almost black through dark red-brown to dark green depending on the initial feedstock, the presence of micro-carbon and chemical composition of the liquid • Hot vapour filtration to remove char gives the oil a more translucent red-brown appearance • High nitrogen content in the liquid can give the oil a dark green tinge
Odour	• Distinctive acrid smoky smell due to low molecular weight aldehydes and acids
Miscibility	• Contains varying quantities of water usually ranging from 15 wt% to an upper limit of 40 wt% while maintaining a stable single phase mixture • Phase separation can be induced by the addition of water • Miscible with polar solvents (methanol, acetone, etc.) • Immiscible with petroleum-derived fuels
Density	• Relatively high density of around 1200 kg/m^3 compared to light fuels
Viscosity	• The viscosity of the oil can vary from as low as 25 cSt to as high as 1000 cSt (at 40 °C) depending on the feedstock and water content

In addition to the bio-oil, roughly 10-15 wt% char and 10-15 wt% non-condensable gases are produced. The gaseous by-product consists mainly of CO_2, CO, and CH_4, as well as traces of H_2 and C_2 compounds. Both by-products can be used in heat recovery applications to minimize carbon loss and improve the efficiency process. Additionally, the char can be used as a metal reductant, soil additive, and in the production of activated carbon [11].

While the oil may seem attractive for its applications, it is quite unfavorable for its thermal instability. In fact, the nature/reactivity of the polar oxygen-containing functional groups in the oxygenated components is reported to be the main cause for the unstable character of the

oil. Coking on burner nozzles for the combustion of the oil or coking upon the injection into hot catalysts beds for the upgrading of bio-oil are frequently observed problems. In addition to the high level of oxygen in the oil, polymerisation of certain components causes an increase in fluid viscosity with time which is problematic for bio-oil storage. Finally, degradation products from the biomass constituents include organic acids, rendering the oil acidic in nature.

1.3. Fluidization for Biomass Fast Pyrolysis

At the heart of biomass conversion processes is the reactor and much thought must be put into the selection of a suitable unit. There are a variety of reactor configurations which can effectively carry out the process of biomass fast pyrolysis. These include: bubbling fluidized bed, circulating fluidized bed, transported bed, ablative, rotating cone, and vacuum moving bed [7,14]. The selection of the reactor configuration is based on satisfying the conditions that favour fast pyrolysis of the available feedstock. Typically, the particle size of the feedstock has the biggest impact on reactor selection. For finer powder-like feedstocks (< 200 μm), cyclonic reactors are typically used; for slightly larger sawdust-like feedstocks (< 2 mm), bubbling fluidized beds are best suited; for pellet-like feedstocks (< 6 mm), circulating fluid or transported beds are appropriate. Choosing the correct reactor configuration is crucial to meet the rapid heat transfer requirements of fast pyrolysis and avoid additional feedstock pre-treatment (such as grinding) which can be expensive.

Bubbling and circulating fluidized beds (Figure 4) are common to produce bio-oil on a commercial scale [15]. The biggest advantage of fluidized bed operation is the spatial parameter uniformity due to appropriate mixing. This reduces radial and axial concentration and temperature gradients, allowing for better fluid-solid contact and increasing biomass conversion. The excellent heat distribution of the bed also results in high heat transfer rates which minimizes the rate of by-product formation. Additionally, the flow of the fluidizing medium may be tuned to increase the gas carry-over velocity and reduce organic vapour residence time in the bed and diminish secondary bio-oil cracking reactions. Particles that elutriates from the bed, such as char, may be collected using cyclones. In the case of circulating beds, the char is typically combusted to recover heat which is recycled into the process to increase carbon efficiency [16]. In fact, the porous structure of char hosts active sites for catalysing secondary bio-oil cracking reactions and

is continuously separated before the organic vapour recovery units. While some fine char may be carried over from the cyclones, they can be removed downstream using hot vapour filters.

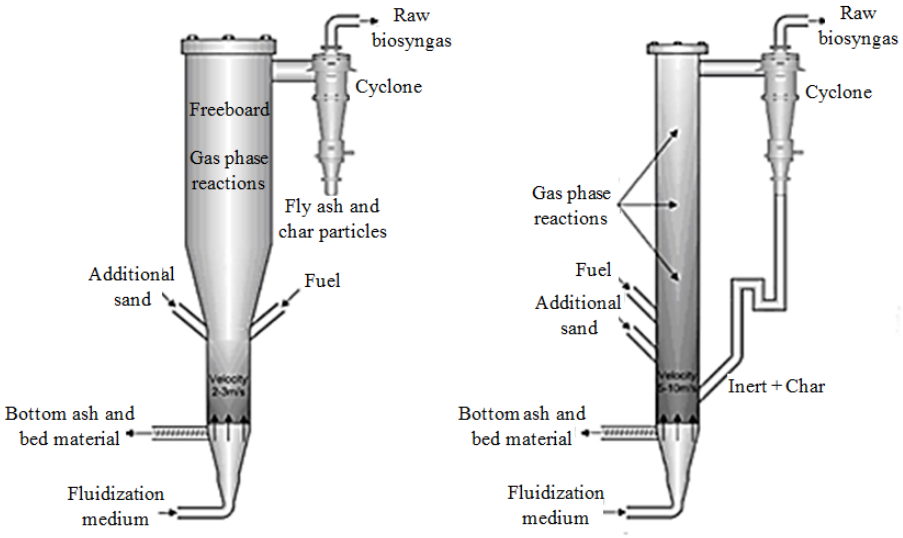

Figure 4: Bubbling (Left) and Circulating (Right) Fluidized Bed Reactors [17]

Bubbling and circulating fluidized bed reactor configurations have been reported to simplify scale-up procedures as opposed to other reactor configurations [18]. Though, the extent of the scale-up is limited considering the difficulty encountered with in-bed temperature uniformity at larger scale. Moreover, while the required smaller sized feedstocks offer the advantage of reducing internal heat transfer limitations, handling and feeding difficulties are commonly encountered.

1.4. Modelling Work for Biomass Fast Pyrolysis Reactors

1.4.1. Significance of Work

With the advances in computing technology and numerical algorithm solvers, reactor modelling is an attractive opportunity for reactor design, optimization and experimental data interpretation. Specifically, using reactor models allows for:

1) Minimizing expenses (cost and time) in the investigation of reactor performance
2) Studying systems that would otherwise be difficult or dangerous to examine
3) Examining the effect of explicit phenomena on reactor operation
4) Verifying and validating experimental data

Installing measuring instruments inside the fluidized beds is difficult without obstructing fluidization behaviour. Moreover, organic vapours from biomass fast pyrolysis causes trouble for visual reactor assessment as it darkens observation windows. Therefore, reactor simulations are beneficial to providing small-scale, local and detailed information such as particle temperatures, porosities, gas or particle velocities which improve the understanding of chemical and physical phenomena prevailing in complex processes such as fast pyrolysis [18].

1.4.2. Current Developments of Reactor Models

There is a good amount of literature on modelling the thermochemical conversion of biomass with fast pyrolysis [11,18–44]. Findings have determined that successfully modelling the thermochemical processing of biomass is considered a multi-scale task. For fast pyrolysis, three sub-models are typically required and are displayed in Figure 5.

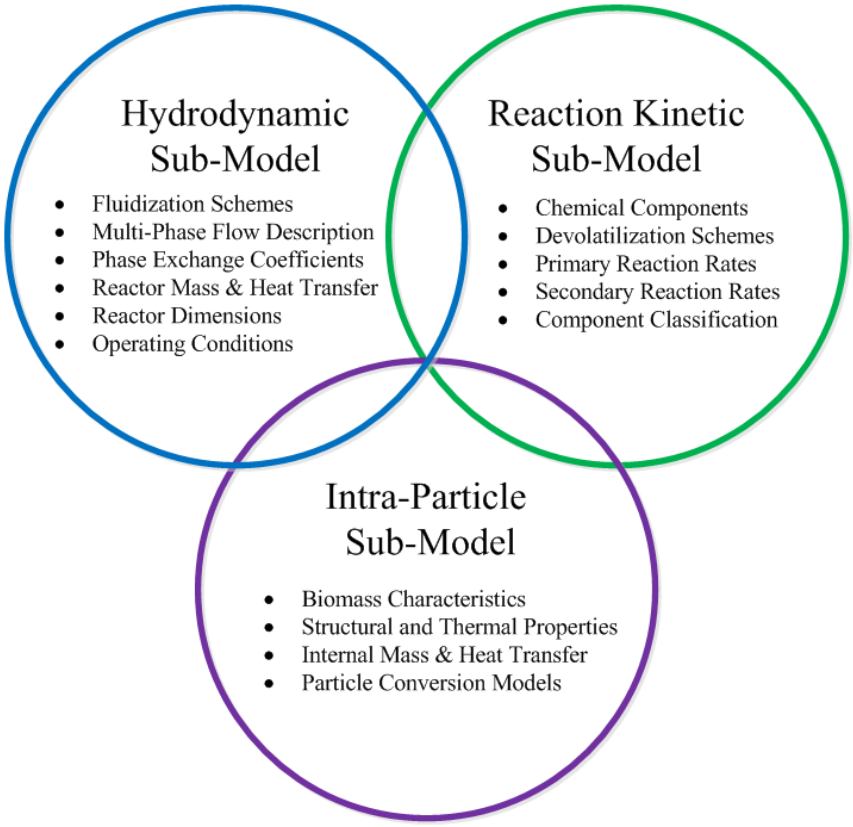

Figure 5: Overview of Primary Sub-Models for Biomass Fast Pyrolysis

Modelling the transport phenomena within the reactor is divided between the hydrodynamic and the intra-particle sub-models, each pertaining to a discrete scale. The species molecular characteristics, interactions and conversion mechanisms are handled by the reaction kinetic sub-model.

1.4.2.1. Hydrodynamic Sub-Models

The mechanism of gas-solid mixing in fluidization is quite sporadic, which inherently makes hydrodynamic modelling a difficult task. However, many efforts have been made to modelling the multi-phase flow and estimating fluidization parameters in different fluidization regimes. In the case of biomass fast pyrolysis, the current understanding and progress with the hydrodynamic models have been classified into three types of models [25]. They are sorted into Black, Grey and White Box models according to the adopted fluid-dynamic simplifications. Transitioning from Black to Grey to White box models increases the level of mechanistic insight

into the behaviour of the fluidized bed. However, the required computational efforts and model input parameters also increase.

1.4.2.1.1. Black-Box Models

In Black-Box Models (BBM), dynamics inside the reactors are not resolved and there is no knowledge about material distribution within the bed (Figure 6). BBMs consist only of overall mass and heat balances over the entire span of the reactor. The performance is based on kinetic data, equilibrium data or experimentally determined conversion equations and the goal is to predict product yields and composition. BBMs are typically used when certain processes are assumed to be dominant in different reactor zones and different models, based on equilibrium or kinetics, are applied [25].

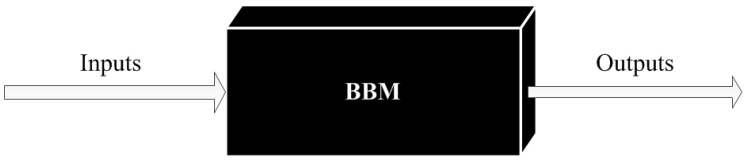

Figure 6: Visual Representation of Black-Box Models

1.4.2.1.2. Grey-Box Models

In Grey-Box Models (GBM), also known as Fluidization Models (FM), the fluid dynamics consists of comprehensive relations which are linked to experimental observations. In contrast to BBMs, multiphase flow patterns can be determined, though not to the extent of the more flexible White-Box Models (WBM). The bed is assumed to have a predefined topology for the different phases and no momentum balance is solved. Generally, the gas is dispersed between two phases, the bubble and emulsion, though some works have also incorporated a third phase (cloud-wake) as seen in Figure 7.

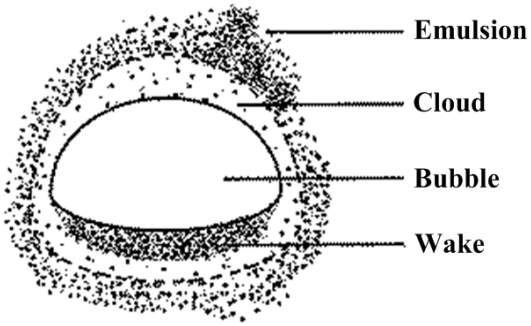

Figure 7: Distribution of Gas in Multi-Phase Models (Adapted from [45])

There exists many variations of GBMs, with some of the more popular ones including: the K-L Model [46], the Davidson-Harrison Model [47] and the Kato and Wen Model [48]. While there exists multi-dimensional and transient models, most models are one-dimensional and steady state, and the fluid-dynamics are based on the two-phase theory of fluidization [25]. In addition, there is no major fundamental difference between models but simply different correlations for phase properties such as bubble size, velocity and volumetric fractions. The most common assumptions are that solids are considered perfectly mixed in the bed and that the gas, in the bubbles and emulsion, follows plug flow behavior. Although sometimes the latter is taken as perfectly mixed, especially at high fluidization velocity within the bubbling flow regime [25]. Bubbles are also commonly stated to be solids-free. In some processes, the behavior of solids within the bed is of great importance and different models have been developed to better define solid movement phenomena such as backmixing [49]. Overall, the advantages of GBMs are that they are very easy to use, there are few inputs required and model runtime is very fast.

1.4.2.1.3. White-Box Models

White-Box Models, also known as Computational Fluid Dynamics Models (CFDM), are the most detailed types of models. However, they are also the most complex since they simultaneously solve equations for mass, energy, momentum using spatial discretization techniques. Initially, the domain is divided into a series of non-overlapping control volumes, each containing a single reference node, in a piecewise profile. Then, the general transport equations, which may vary depending on the surroundings (boundary conditions) of a control volume, are solved numerically. Different modelling approaches may be used to track the dynamics of the bubbling bed, under different regimes and at different scales, such as: direct

numerical solution (DNS), large eddy simulation (LES), discrete particle modelling (DPM), two-fluid modelling (TFM), Eulerian-Eulerian modelling (EEM), Eulerian-Lagrangian modelling (ELM) and Lagrangian-Lagrangian modelling (LLM). The advantage of WBMs is the flexibility of exploring hardware and fluid dynamic impacts in diverse scenarios such as those involving reactor modifications and scale-up. Altogether, while WBMs are expensive to run and not yet fully validated (uncertainty of some parameters in closure relations [25]), they are proving to be promising tools for fluidized bed modelling. Indeed, some proprietary and open source software has facilitated research advances in recent years including: CPFD Barracuda VR Solutions, ANSYS Fluent & CFX, OpenFOAM and MFiX.

1.4.2.2. Intra-Particle Sub-Models

The efforts in intra-particle modelling typically pertain to processes with large, slightly thermally conductive particles and low heating rates (slow pyrolysis) where the focus is on producing torrefied or char products. However, intra-particle modelling has also been the subject of work in woody biomass fast pyrolysis. Simulating the internal behavior of wood particles, which are naturally known to be anisotropic and susceptible to abrasion, is a complex task that requires assumptions and approximations. The particles are commonly taken to be homogeneous, isotropic and monosized [50]. In addition, the particle conversion pathway must also be approximated. Figure 8 presents three of the most common pathways (a) the uniform conversion model, (b) the shrinking unreacted particle model and (c) the shrinking unreacted core model. In the UCM model, conversion takes place equivalently throughout the non-shrinking particle and is linked to a change in particle density. In SUPM and SUCM, the reaction takes place at the surface of the particle core. For SUPM, the ash is assumed to peel off instantaneously and particle shrinks as it is converted whereas in SUCM, particle size is preserved since the ash remains attached to the particle and increases transport resistance. Merging the concepts from these models leads to more comprehensive pathways such as the progressive model with shrinking reacting particle (PMSP) and progressive model with shrinking reacting core (PMSC) [25].

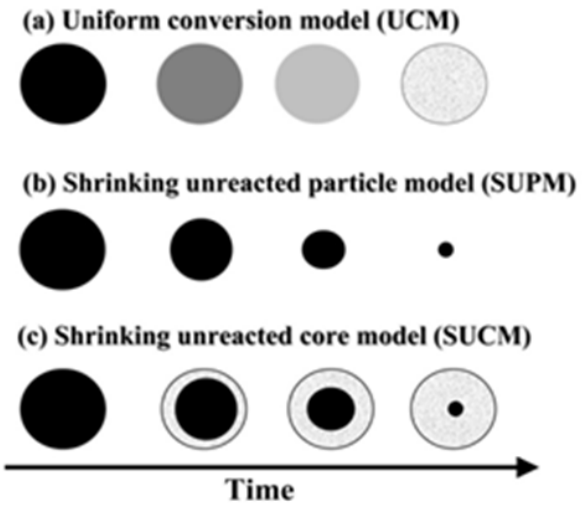

Figure 8: Biomass Particle Conversion Models (Adapted from [25])

One of the most important modelling considerations for the intra-particle sub-model is whether or not the particle is thermally resistive. This is determined based on the particle Biot number. If Biot number is much smaller than 1 (usually < 0.2) then the intra-particle heat transfer resistance is very low and a "thermally thin" particle assumption is valid. This signifies that the particle behaves isothermally. Since wood is not particularly thermally conductive, the size (characteristic length) of the feedstock must be quite small to minimize the Biot number. Typically, particles sizes up to 1.0 mm are considered thermally thin though others have found that intra-particle transport phenomena does not affect pyrolysis oil yields for particle sizes up to 2.0 mm [30,51]. For larger particles (thermally thick), the temperature profile is not uniform across the particle and volatiles are not extracted from within the particle immediately which increases their susceptibly to secondary cracking reactions.

In the end, intra-particle models on their own are unsuitable for reactor modelling efforts because they do not capture the effect of reactor operating conditions on product yields. Therefore, coupling simplified particle models within reactor models is an ideal compromise between precision and computational complexity.

1.4.2.3. Reaction Kinetic Sub-Models

The pyrolysis of wood is an intricate process that is still not completely understood [9]. The variety and complexity of fast pyrolysis reactions make kinetic modelling an interesting and challenging study. While there does exist certain difficulties defining intrinsic kinetic pathways and equation constants, some kinetic schemes have been proposed. Various forms of these devolatilization mechanisms are reviewed in depth and tested in Chapter 3. Remarkably, many biomass fast pyrolysis modelling studies incorporate complex hydrodynamic and intra-particle sub-models but fail to establish detailed reaction kinetic sub-models. Using simple devolatilization schemes is undeniably the most significant shortfall of those models. In addition, the few models that do include detailed mechanisms fail to validate the model performance against experimental findings. There is much work that needs to be done in this matter.

1.5. Thesis Objectives

In recent years, research involving pilot-scale biomass fast pyrolysis has been undertaken at Natural Resources Canada's CanmetENERGY Bells Corner Complex in Ottawa, Ontario. This unit is one of the largest pilot-scale fluidized bed fast pyrolysis reactors in Canada with a capacity of up to 10 kg/h. Though, dealing with such a large scale system comes at the expense of long and costly experiments. Attempting to run an experiment can take up to a week with as much as three working operators. The analysis and characterization of products is also a resource intensive task. Hence, the aim of this work is to develop a reactor model which can be used to interpret and predict their experimental results. The model should be simple to use, be easily accessible, does not require commercial software and should estimate not only the quantity of products but also the quality. The model will comprise of sub-models studying the influence of different operating parameters and feed properties on the quality of the bio-oil produced. To accomplish these objectives, further development of the currently established reaction kinetic sub-models is required and a method for experimental validation is necessary. Part of the work will also involve conducting experimental work with the pilot-scale fluidized bed fast pyrolysis reactor using specific woody biomass components such as cellulose and lignin to further understand their individual devolatilization pathways. To accomplish the objectives, the following tasks have been set:

1) Develop a generic fluidized bed reactor model with a versatile programming language; Visual Basic for Applications
2) Model and test the extension and performance of the reaction kinetic sub-model by using complex multi-component and multi-step devolatilization schemes
3) Compare the model outputs to experimental results from pilot-scale fluidized bed fast pyrolysis unit
4) Investigate the effect of the dominant independent model variables such as feed composition and bed temperature on measurable outputs
5) Propose further modifications for devolatilization mechanisms (explicitly for the cases with product specification)
6) Model and test the extension and performance of the hydrodynamic sub-model by adapting the initially developed fluid dynamic structure
7) Compare the new model outputs to experimental results from the pilot-scale fluidized bed fast pyrolysis unit
8) Investigate the effect of the dominant independent model variables such as fluidizing velocity and feedstock particle size on measurable outputs
9) Propose further modifications for new fluidized bed reactor model

Results generated from this work will help in overcoming the current limitations of existing biomass fast pyrolysis reactor models.

1.6. Thesis Outline

The thesis is divided into five chapters from which two chapters are prepared in manuscript form for publication in a refereed journal.

Chapter 1 introduces the current developments in renewable energy technologies. It describes current thermochemical conversion technologies such as biomass fast pyrolysis which is used to produce a liquid carbon-neutral bio-product. In addition, it covers the significance and current developments of biomass fast pyrolysis reactor modelling along with their advantages and downfalls.

Chapter 2 summarizes the experimental apparatus used to conduct the experiments as well as the equipment used to recover and sample the products. It also presents the properties of the biomass feedstocks and the characterization instruments, standards and methods used to quantify the pyrolysis products. The last section of the chapter is an overview of the graphical user interface with the inputs and outputs of the model.

Chapter 3 is a manuscript prepared for journal publication. The work explores the improvements in multi-step and multi-component fast pyrolysis kinetic mechanisms and compares their impacts on reactor measurable outputs such as product (bio-oil, gas and biochar) yields and distinctive compositional values. The effects of biomass composition and operating temperatures on reactor performance are examined. Additionally, mechanism modifications are suggested to minimize the differences in component class outputs and increase the accuracy of model predictions.

Chapter 4 is a manuscript prepared for journal publication. The work explores the overall effect of different multi-phase flow patterns and hydrodynamic assumptions on the performance of grey-box models. The effects of biomass particle size as well as the fluidization velocity on the yield of pyrolysis products are examined.

Chapter 5 concludes the thesis and summarizes the main findings of the work. Overall recommendations for future work are presented.

Chapter 2: Experimental Apparatus, Materials and Modelling Tools

2.1. Pilot-Scale Biomass Fast Pyrolysis System

All experiments are conducted on NRCan CanmetENERGY's pilot-scale fast pyrolysis system presented in Figure 9. The figure shows an overall layout of the system along with key monitoring instrument locations. There are three major sections to the system which are: the feeding section, the reaction section and the organic vapour recovery section.

2.1.1. Feeding Section

The feeding section contains the feed hopper and the metering auger. The feed hopper is slightly pressurized to avoid back flow from the hydrostatic pressure of the bed and is usually loaded with roughly 25 kg of feed per experiment. An electric vibrator is used to facilitate the flow of the feedstock into the metering auger. The metering auger which is driven by an adjustable electric motor is approximately 2.5 cm in diameter and feeds in-bed at nearly 10 cm above the distributor plate. The weight of the hopper is recorded through the control software and converted into a feed rate based on the time the auger was active. The weight is plotted against the time to verify that the feed rate is constant. Due to the low size and density of the biomass particles, in-bed feeding is required to achieve sufficient residence time for conversion and avoid premature entrainment and bed segregation.

2.1.2. Reaction Section

At the heart of the system is the fluidized bed reactor which is a 304 stainless steel schedule 40 pipe that is 0.10 m in diameter (ID) and 1.00 m in height from the distributor plate to the top of the freeboard. The column operates at atmospheric pressure, which is monitored along with the temperatures throughout the whole column. Figure 10 displays the key reactor parameter monitoring instruments. Heat is provided to the column using four 2250 W band heaters and ceramic fiber sheets are used for insulation. The bed material used in the reactor is olivine sand, with a Sauter mean diameter of approximately 615 microns, an average particle density of roughly 2830 kg/m^3 and an average bulk density of 1515 kg/m^3. According to

Geldart's classification of particles, the material falls into the class of type B particles. The particle size distribution for the material is shown in Figure 11. For every run, the bed material is emptied and replenished with 3.75 kg of fresh olivine sand resulting in a static bed height of approximately 30 cm. The olivine sand was chosen due to its acceptable mechanical stability during prolonged fluidization but mostly since it is a relatively inexpensive and inert bed material. Some authors have presumed that the alkali content of the sand may be slightly detrimental to the organic vapours by catalytically inducing secondary cracking [52,53]. However, these presumptions are believed to be inadmissible at pyrolysis operating temperatures. In fact, the experimental results were compared with results conducted with a different bed material (low porosity aluminosilicate beads - Mullite LD) and similarity of the results strongly suggest that neither of the bed materials have a catalytic influence at the operating conditions. Nitrogen gas is used to obtain an inert and oxygen-free fluidizing medium. The gas is pre-heated to the operating temperature before entering the column through the distributor plate. The flow of the gas can be varied, though a residence time of below 2 second is standard for fast pyrolysis applications. The moisture content of the fluidizing gas is quite small and is assumed to be completely dry for the mass balance calculations.

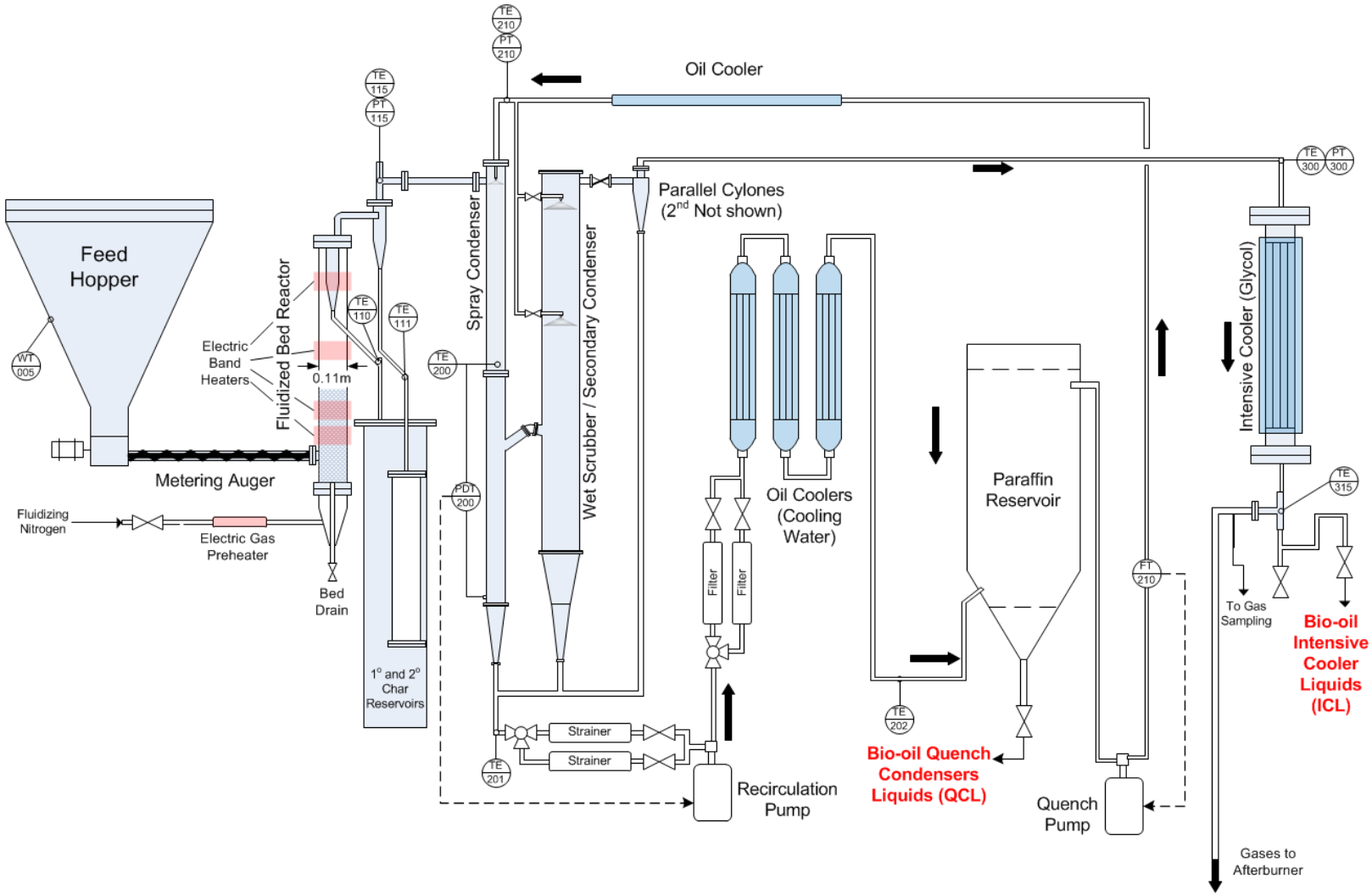

Figure 9: Schematic of Fluidized Bed Fast Pyrolysis System at CanmetENERGY's Bells Corner Complex Laboratories

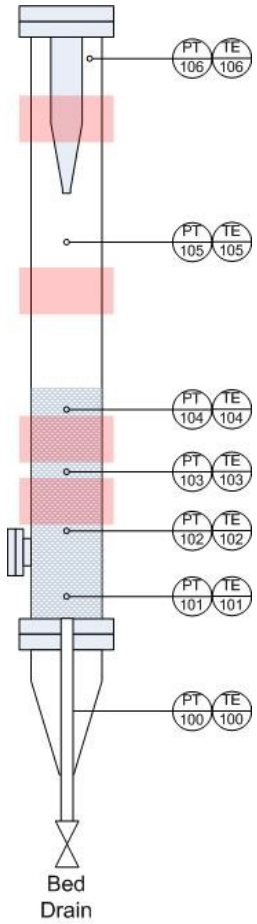

Instrument ID	Description
PT-100 & TE-100	Windbox Pressure Transducer and Thermocouple
PT-101 & TE-101	Bottom Bed Pressure Transducer and Thermocouple
PT-102 & TE-102	Feed Port Level Bed Pressure Transducer and Thermocouple
PT-103 & TE-103	Middle Bed Pressure Transducer and Thermocouple
PT-104 & TE-104	Top Bed Pressure Transducer and Thermocouple
PT-105 & TE-105	Middle Freeboard Pressure Transducer and Thermocouple
PT-106 & TE-106	Top Freeboard Pressure Transducer and Thermocouple

Figure 10: Key Reactor Instrument Location for Temperature and Pressure Monitoring

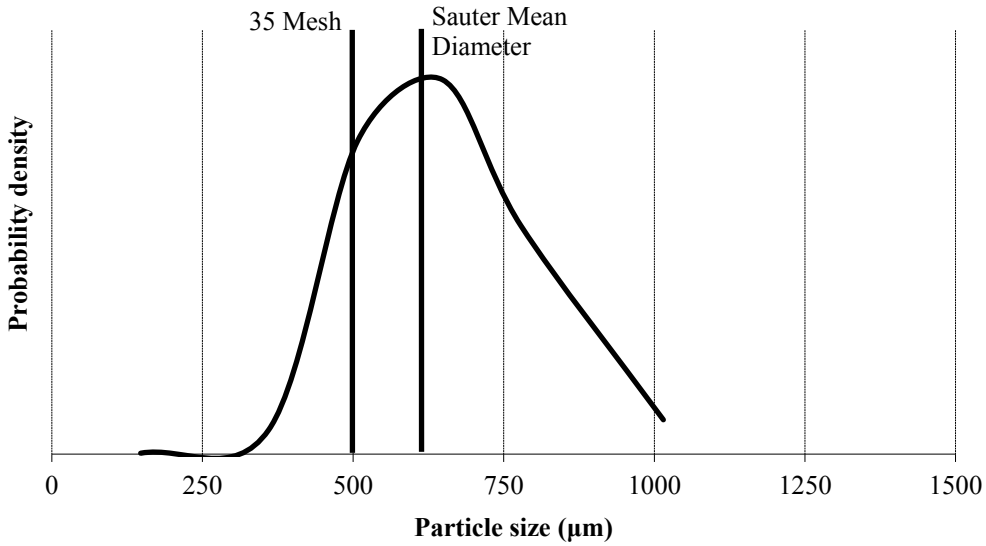

Figure 11: Particle Size Distribution for 32-B4 Olivine Sand

2.1.3. Organic Vapour Recovery Section

The purpose of this section is to separate the condensable organic vapours from the non-condensable gases and solids. Initially, most of the particles that are entrained from the bed are collected in a cyclone which is located at the top, inside of the reaction column. The recovered particles (which are mostly char) fall down a pipe into a char reservoir. To enhance solids removal, the reactor outlet stream passes through a second cyclone to remove any solids which may have carried over after the first cyclone. The recovered solids fall into a second char reservoir. Once the experiment is complete, the remaining bed material may be weighed and the difference in bed material mass is tared from the mass of solids in the char reservoirs to obtain the yield of char. Now that the solids have been removed, the gases then pass through two spray condensers (which serve as wet scrubbers) and a series of heat exchangers to rapidly quench the majority of the condensable organic vapours and recover bio-oil. An immiscible hydrocarbon, Isopar V (paraffin oil), at a temperature of approximately 25 ºC is used as a quench fluid for the vapours. A series of strainers and filters are used to further reduce the particulate content of the bio-oil. Finally, the majority of the bio-oil is then slowly recovered at the bottom of a settling reservoir while the Isopar V is recovered at the top and recycled back to the spray condensers. A second attempt at recovering the condensable organics from the gas stream is done using an intensive cooler with a refrigerant (glycol) at roughly -2 ºC to further cool the vapours to about 10 ºC. Though, the quantity of oil recovered at this stage is only a slight fraction of the amount recovered initially. Interestingly, while the vapours do pass through the wet scrubbers in the recovery process, a small amount of condensable material (bio-oil) is suspended in the gas as a very fine aerosolized mist which is not completely removed from the gas stream. Therefore, before sending the remaining gases (mostly non-condensable gases) to an afterburner to combust any remaining organic material before venting to the atmosphere, a slipstream of the gas is sampled through a refrigerated methanol absorption unit to quantify the fraction of aerosols which was lost with the non-condensable gas stream. The quantification of the bio-oil components within the methanol sample is done using rotary vacuum evaporation and gas sampling bags are used to capture the non-condensable gases for analysis.

2.2. Biomass Feedstocks

For efficient biomass fast pyrolysis experiments, the trials must be conducted using finely grinded feedstocks to ensure rapid devolatilization and maximize bio-oil yields. Three primary feedstocks were tested: maple-derived hardwood sawdust, Solka-Floc powdered cellulose and interior hog fines.

2.2.1. Maple-Derived Hardwood Sawdust

The first woody feedstock that was used was a maple-derived hardwood sawdust material from local mills around Holland Landing, Ontario. The feedstock, which has a particle density of roughly 500 kg/m^3, was not pretreated in any way (milling or drying) before use. A picture of the feedstock is presented in Figure 12, the cumulative size distribution graph is presented in Figure 13 and detailed characterization results are presented in Table 2.

Figure 12: Hardwood Sawdust Sample (2x2mm Grid)

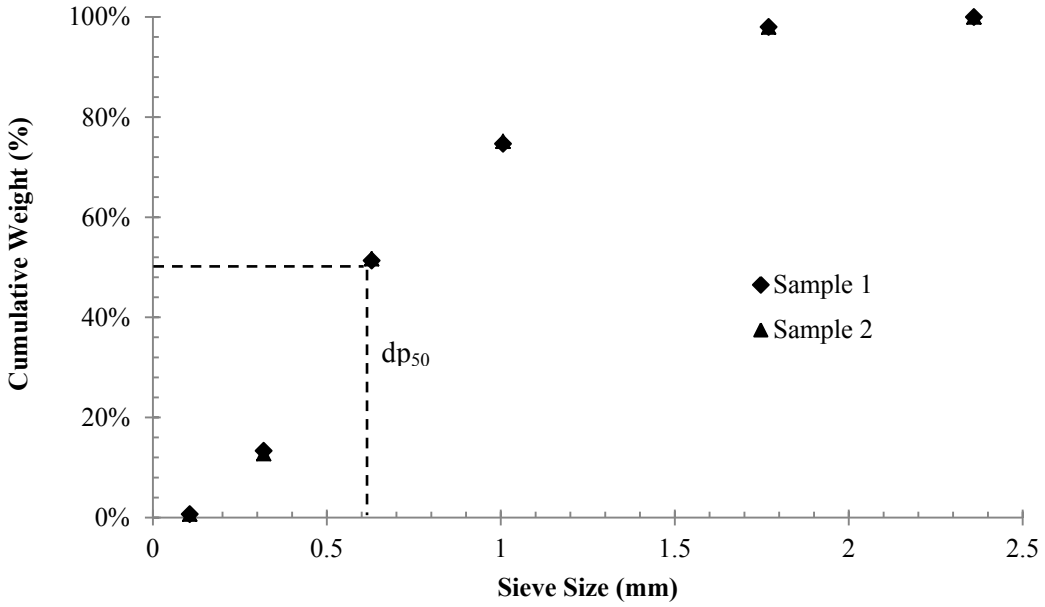

Figure 13: Cumulative Size Distribution for Hardwood Sawdust Sample

Table 2: Hardwood Sawdust Feedstock Characterization Results

Parameter	Method	Analyzed Value (wt%)	Dry - At 105°C (wt%)	Dry Ash-Free (wt%)
Proximate Analysis				
Moisture Content by TGA	ASTM D7582	7.27	-	-
Ash by TGA	ASTM D7582	0.36	0.39	-
Volatiles Content by TGA	ISO 562	79.04	85.24	85.57
Fixed Carbon Content by TGA	ASTM D7582	13.33	14.38	14.44
Ultimate Analysis				
Carbon	ASTM D5373	45.6	49.2	49.4
Hydrogen	ASTM D5373	5.54	5.98	6
Nitrogen	ASTM D5373	0.11	0.12	0.12
Total Sulfur	ASTM D4239	< 0.05	-	-
Oxygen by Difference	In-House	41.11	44.33	44.52
Biochemical Analysis				
Cellulose	In-House & TAPPI T-249	-	-	~ 40
Hemicellulose	In-House & TAPPI T-249	-	-	~ 38
Lignin	In-House & TAPPI T-222	-	-	~ 22
Ash Analysis				
SiO_2	ASTM D4326	2.06	-	-
Al_2O_3	ASTM D4326	0.25	-	-
Fe_2O_3	ASTM D4326	0.43	-	-
TiO_2	ASTM D4326	<0.03	-	-
P_2O_5	ASTM D4326	2.66	-	-
CaO	ASTM D4326	29.07	-	-
MgO	ASTM D4326	5.9	-	-
SO_3	ASTM D4326	2.62	-	-
Na_2O	ASTM D4326	0.37	-	-
K_2O	ASTM D4326	25.5	-	-
Barium (ppm)	ASTM D4326	2550	-	-
Strontium (ppm)	ASTM D4326	1502	-	-
Vanadium (ppm)	ASTM D4326	<50	-	-
Nickel (ppm)	ASTM D4326	<50	-	-
Manganese (ppm)	ASTM D4326	1395	-	-
Chromium (ppm)	ASTM D4326	<50	-	-
Copper (ppm)	ASTM D4326	242	-	-
Zinc (ppm)	ASTM D4326	1144	-	-
Loss on Fusion	ASTM D4326	29.2	-	-

2.2.2. Solka-Floc 200 MO Powdered Cellulose

The second feedstock that was used was Solka-Floc® 200 MO Powdered Cellulose. The material is a low-dust powder that is said to be anti-caking. While it may not have been derived explicitly from a woody source, it was nonetheless used to examine the behaviour of the cellulosic component of woody biomass. The feedstock, which has a particle density of 435 kg/m^3, was not pretreated in any way (milling or drying) before use. A picture of the feedstock is presented in Figure 14, the cumulative size distribution graph is presented in Figure 15 and detailed characterization results are presented in Table 3.

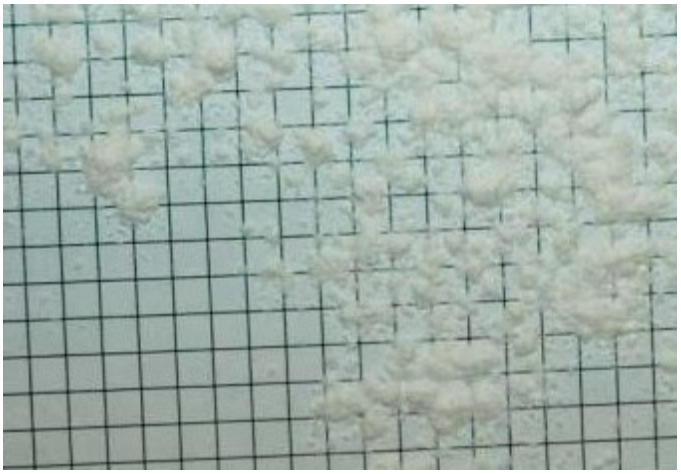

Figure 14: Solka-Floc Powdered Cellulose Sample (5x5 mm Grid)

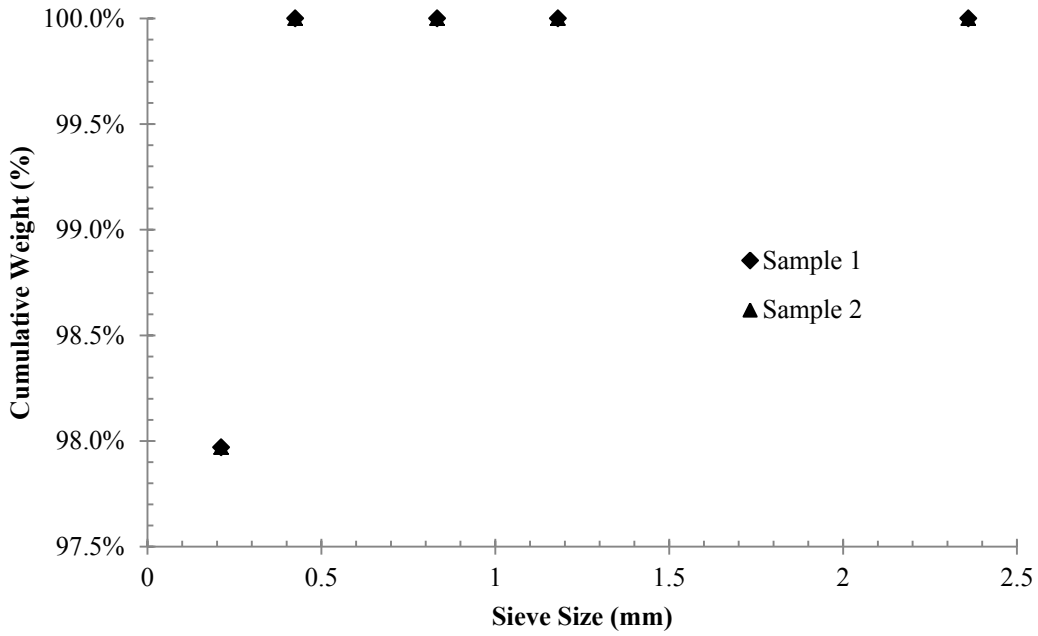

Figure 15: Cumulative Size Distribution for Powdered Cellulose Sample

Table 3: Powdered Cellulose Feedstock Characterization Results

Parameter	Method	Analyzed Value (wt%)	Dry - At 105°C (wt%)	Dry Ash-Free (wt%)
Proximate Analysis				
Moisture Content by TGA	ASTM D7582	5.97	-	-
Ash by TGA	ASTM D7582	0.19	0.20	-
Volatiles Content by TGA	ISO 562	84.80	90.18	90.36
Fixed Carbon Content by TGA	ASTM D7582	9.04	9.61	9.63
Ultimate Analysis				
Carbon	ASTM D5373	42.0	44.7	44.8
Hydrogen	ASTM D5373	5.83	6.20	6.21
Nitrogen	ASTM D5373	< 0.1	-	-
Total Sulfur	ASTM D4239	< 0.05	-	-
Oxygen by Difference	In-House	46.01	48.93	49.03
Biochemical Analysis				
Cellulose	In-House & TAPPI T-249	-	-	~ 100
Hemicellulose	In-House & TAPPI T-249	-	-	~ 0
Lignin	In-House & TAPPI T-222	-	-	~ 0
Ash Analysis				
SiO_2	ASTM D4326	2.91	-	-
Al_2O_3	ASTM D4326	0.26	-	-
Fe_2O_3	ASTM D4326	4.70	-	-
TiO_2	ASTM D4326	<0.03	-	-
P_2O_5	ASTM D4326	0.23	-	-
CaO	ASTM D4326	17.92	-	-
MgO	ASTM D4326	7.80	-	-
SO_3	ASTM D4326	7.85	-	-
Na_2O	ASTM D4326	26.84	-	-
K_2O	ASTM D4326	4.34	-	-
Barium (ppm)	ASTM D4326	518	-	-
Strontium (ppm)	ASTM D4326	1068	-	-
Vanadium (ppm)	ASTM D4326	<50	-	-
Nickel (ppm)	ASTM D4326	74	-	-
Manganese (ppm)	ASTM D4326	1308	-	-
Chromium (ppm)	ASTM D4326	61	-	-
Copper (ppm)	ASTM D4326	94	-	-
Zinc (ppm)	ASTM D4326	864	-	-
Loss on Fusion	ASTM D4326	21.32	-	-

2.2.3. Interior Hog Fines

The third feedstock that was used was Interior Hog Fines derived from hog fuel from the Canfor Northwood mill in Prince George, British Columbia. Hog fuel is a residual product, commonly sources from pulp mills, which is a mixture of bark and wood chips. The feedstock, which has a particle density of 500 kg/m^3, was created by sieving the hog fuel through a large rotary sieve shaker and recovering the fines. The purpose of this feedstock is to examine the behaviour of the lignin and ash components of woody biomass while maintaining similar physical traits to the hardwood sawdust. A picture of the feedstock is presented in Figure 16, the cumulative size distribution graph is presented in Figure 17 and detailed characterization results are presented in Table 4.

Figure 16: Interior Hog Fines Sample (2x2mm Grid)

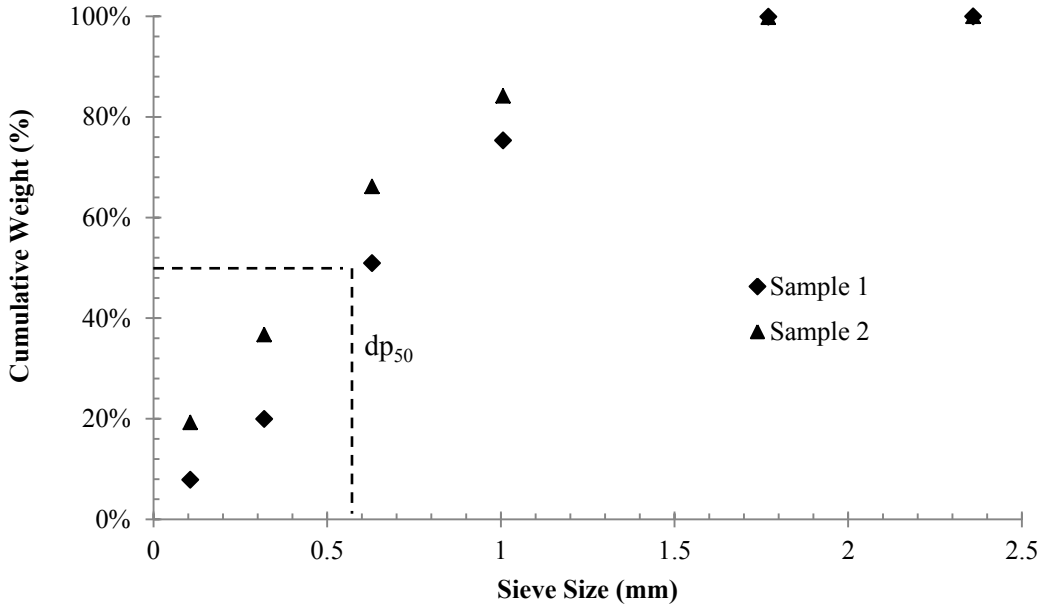

Figure 17: Cumulative Size Distribution for Interior Hog Fines Sample

Table 4: Interior Hog Fines Feedstock Characterization Results

Parameter	Method	Analyzed Value (wt%)	Dry - At 105°C (wt%)	Dry Ash-Free (wt%)
Proximate Analysis				
Moisture Content by TGA	ASTM D7582	10.45	-	-
Ash by TGA	ASTM D7582	10.69	11.94	-
Volatiles Content by TGA	ISO 562	64.01	71.48	81.17
Fixed Carbon Content by TGA	ASTM D7582	14.85	16.58	18.83
Ultimate Analysis				
Carbon	ASTM D5373	42	46.9	53.3
Hydrogen	ASTM D5373	4.8	5.36	6.09
Nitrogen	ASTM D5373	0.24	0.27	0.31
Total Sulfur	ASTM D4239	0.16	0.18	0.2
Oxygen by Difference	In-House	31.65	35.34	40.78
Biochemical Analysis				
Cellulose	In-House & TAPPI T-249	-	-	~ 27
Hemicellulose	In-House & TAPPI T-249	-	-	~ 23
Lignin	In-House & TAPPI T-222	-	-	~ 50
Ash Analysis				
SiO_2	ASTM D4326	16.94	-	-
Al_2O_3	ASTM D4326	3.73	-	-
Fe_2O_3	ASTM D4326	2.43	-	-
TiO_2	ASTM D4326	0.18	-	-
P_2O_5	ASTM D4326	10.05	-	-
CaO	ASTM D4326	29.95	-	-
MgO	ASTM D4326	15.17	-	-
SO_3	ASTM D4326	3.78	-	-
Na_2O	ASTM D4326	0.89	-	-
K_2O	ASTM D4326	5.69	-	-
Barium (ppm)	ASTM D4326	501	-	-
Strontium (ppm)	ASTM D4326	819	-	-
Vanadium (ppm)	ASTM D4326	<50	-	-
Nickel (ppm)	ASTM D4326	<50	-	-
Manganese (ppm)	ASTM D4326	2150	-	-
Chromium (ppm)	ASTM D4326	<50	-	-
Copper (ppm)	ASTM D4326	54	-	-
Zinc (ppm)	ASTM D4326	473	-	-
Loss on Fusion	ASTM D4326	10.78	-	-

2.3. Product Characterization Instruments

The current section presents the instruments, standards and methods used to quantify the produced char, non-condensable gases and bio-oil products. The majority of the analyses are conducted by the CanmetENERGY-Ottawa Characterization Laboratories.

2.3.1. Char Analysis

To know whether or not the biomass particles are being completely pyrolyzed, it is important to know the content of the char. The char is characterized based on an ultimate and proximate analysis using the same methods as the ones used to characterize the biomass feedstocks. A major part of the ultimate analysis is conducted using the ASTM D5373 method which is a standard test method for determination of carbon, hydrogen and nitrogen in the analysis of coal and coke. The sulfur content is measured using the ASTM D4239 method which is a standard test method for sulfur in the analysis sample of coal and coke using high-temperature tube furnace combustion. The proximate analysis is done following the ASTM D7582 method, which is a standard test method for determining ash and fixed carbon of coal and coke by macro thermogravimetric analysis, and ISO 562, which is a method of determining the volatile matter of hard coal and of coke.

2.3.2. Gas Analysis

The gas yields are calculated based on the average gas composition measured from gas bags taken during the experimental trials. A nitrogen balance, assuming that the amount of nitrogen generated in the process is insignificant, is used to determine a total gas flow. The concentration of the all the other gases besides nitrogen coupled with the flowrate of nitrogen were then used to determine the mass flow of pyrolysis gases produced. The analysis of these non-condensable gases was done using a Wasson RGA configured HP7890 gas chromatograph equipped with two thermal conductivity detectors (one for hydrogen) and one flame ionization detector. It utilizes several columns including a capillary column for hydrocarbons, a PLOT column for hydrogen and packed columns, primarily molecular sieves, to separate the fixed gases. The analyzer is set up for refinery gas analysis and is not capable of detecting trace levels below the limit of approximately the 100 ppm range.

2.3.3. Bio-Oil Analysis

The analysis of bio-oil samples is crucial to evaluate the quality of the fuel in terms of physiochemical properties and chemical composition. The bio-oil collected from both recovery taps in the system is mixed and refrigerated (below 0 ºC) after production to minimize potential chemical activity.

2.3.3.1. Physiochemical Properties

A major part of the ultimate analysis is conducted using the ASTM D5291 method which is a method for instrumental determination of carbon, hydrogen, and nitrogen in petroleum products and lubricants. Though, this method was slightly modified in-house for the analysis of pyrolysis oils. Afterwards, the oxygen content is calculated by difference. The water content, viscosity, density, ash content, solids content and higher heating value are calculated using the ASTM E203, ASTM D445, ASTM D4052, ASTM D482, ASTM D7579 and ASTM D240, respectively. ASTM E203 is a standard test method for water using volumetric Karl Fischer titration, ASTM D445 is a standard test method for kinematic viscosity of transparent and opaque liquids, ASTM D4052 method is as standard test method for density, relative density, and API gravity of liquids by digital density meter, ASTM D482 is a standard test method for ash from petroleum products, ASTM D7579 is a standard test method for pyrolysis solids content in pyrolysis liquids by filtration of solids in methanol and ASTM D240 is a standard test method for heat of combustion of liquid hydrocarbon fuels by bomb calorimeter. An in-house method is used for the determination of the pH of pyrolysis liquids via glass electrode.

2.3.3.2. Chemical Composition

The complex nature of bio-oil requires a characterization method able to simultaneously separate, identify and quantify the components. Yet, the characterization of chemicals in bio-oil is not standardized to the same extent as the measurement of the oil physiochemical properties. Chromatography, both gas and liquid, techniques are most commonly used to determine the component concentrations [54]. For this work, Gas Chromatography – Mass Spectroscopy (GC-MS) was relied upon. GC-MS allows for compositional analysis based on: the retention time of

components in the instruments column and the mass spectra, which can then be compared to a set of reference components.

To perform the GC-MS analyses, the bio-oil samples were first dissolved in methanol at a 5-10 times dilution ratio by weight. The samples were injected immediately following dilution to minimize interactions between the sample and solvent. The GC specifications are presented in Table 5.

Table 5: Gas Chromatograph Specifications

Column Type	DB5-MS, (Phenyl Arylene polymer virtually equivalent to (5 %-Phenyl)-methylpolysiloxane)
Column Dimensions	ID: 0.25 mm Length: 30 m Film: 250 µm
Injection Volume	1 µL
Split Injection Ratio	50:1
Injection Temperature	280 °C
Oven Parameters	Initial temperature 35 °C with zero hold Ramp at 0.5 °C/min to 46 °C Ramp at 1.0 °C/min to 124 °C Ramp 5 °C/min to 325 °C with a 4.8 min hold

After leaving the GC column, the sample passed through a mass spectrometer which scanned between 15-200 amu for the initial 20 minutes and 15-550 amu for the duration of the analysis. The mass spectra data was interpreted using Agilent Chemstation Data Analysis software and the NIST05 and W8N.08 Mass Spectral Libraries. The extent of the mass spectra match with the libraries (termed match quality) was expressed as a value between 0-99. Typically, a match quality greater than 90 is reliable for identification. To confirm correct component identification, a target group of common bio-oil compounds, with high match quality, were purchased (where possible) or prepared using pure compounds to be used as calibration materials. Initial quantitative measurements were performed using external standard calibration only, however an internal standard method was later created. Table 6 displays the components that were detected using the described GC-MS method. The pure compounds used for calibration are bolded. Relative response factors were used for all other compounds and are highlighted in the same colour as their corresponding pure compound.

Table 6: List of Detected Components by GC-MS Method

Component	Chemical Formula	Molecular Weight
EUC2 (possibly Acetaldehyde)	-	-
Hydroxy-acetaldehyde	$C_2H_4O_2$	60.052
Acetic acid	**$C_2H_4O_2$**	**60.052**
Hydroxyacetone	**$C_3H_6O_2$**	**74.079**
Acetic acid, hydroxy-, methyl ester (Glycolic Acid)	$C_3H_6O_3$	90.078
EUC1	-	-
Acetic acid, methyl ester (Methyl Acetate)	$C_3H_6O_2$	74.079
Propanoic acid, 2-oxo-, methyl ester (Methyl Pyruvate)	$C_4H_6O_3$	102.089
Furfural	**$C_5H_4O_2$**	**96.084**
Furan, tetrahydro-2,5-dimethoxy-	$C_6H_{12}O_3$	132.158
EUC4	-	-
2-Cyclopenten-1-one, 2-methyl-	C_6H_8O	96.127
Phenol	**C_6H_6O**	**94.111**
EUC3	-	-
2-Cyclopenten-1-one, 2-hydroxy-3-methyl- or 1,2-Cyclopentanedione, 3-methyl-	$C_6H_8O_2$	112.127
2-methoxyphenol (o-Guaiacol)	**$C_7H_8O_2$**	**124.137**
Phenol, 2-methoxy-4-methyl- (p-Creosol)	$C_8H_{10}O_2$	138.164
1,2-benzenediol (Catechol)	**$C_6H_6O_2$**	**110.111**
1,2-Benzenediol, 3-methyl-	$C_7H_8O_2$	124.137
1,2-Benzenediol, 4-methyl-	$C_7H_8O_2$	124.137
2-Methoxy-4-vinylphenol (p-Vinyl Guaiacol)	$C_9H_{10}O_2$	150.175
Phenol, 2,6-dimethoxy- (Syringol)	**$C_8H_{10}O_3$**	**154.163**
Eugenol	$C_{10}H_{12}O_2$	164.201
Succinic acid	**$C_4H_6O_4$**	**118.088**
Vanillin	**$C_8H_8O_3$**	**152.147**
Isoeugenol	**$C_{10}H_{12}O_2$**	**164.201**
Levoglucosan	**$C_6H_{10}O_5$**	**162.141**
Vanillic acid	**$C_8H_8O_4$**	**168.147**
Phenol, 2,6-dimethoxy-4-(2-propenyl)-	$C_{11}H_{14}O_3$	194.227
4-Hydroxy-2-methoxycinnamaldehyde	$C_{10}H_{10}O_3$	178.185

- EUC: Experimentally Unidentifiable Component
- Standards were prepared from pure components by Sigma Aldrich (>98 % purity, with the exception of Hydroxyacetone, >90 %)

There are practical limits to the number of components that can be quantified by GC-MS. In fact, GC-MS can only detect compounds that are volatilized at injection conditions and do not

permanently adhere to the stationary phase of the GC column. Some components are not volatile enough and some components polymerize or decompose before they evaporate and therefore will not be detected (or will be wrongly detected) by the GC-MS analysis. In addition, there are many components which are not matched by analysis software (lack of calibration to a certain extent) or are present in too small of amounts to be individually accounted for. For these reasons, hundreds of components are not detected and quantified which can form a significant portion of the bio-oil.

The absence of standardized methods in the analysis of pyrolysis oils is a well-known problem. The procedures employed for characterizing bio-oil are constantly evolving and improvements to these techniques are necessary for better accuracy and reliability. While there is a generally understanding of the prominent components making up the bio-oil, the quantification is variable and the repeatability is challenging. Several possible contributors to the variability are:

- The variability between fresh bio-oil produced from the same conditions and feedstock
- Reactions occurring due to aging or due to solvent interactions that are not being reproduced in the sampling methods
- Unrepresentative sampling methods
- Inherent variability in the GC-MS methods
- Non-repeatable thermal decomposition reactions occurring during the analysis

It should be noted that the chemical determination and quantification methods have underwent substantial change and improvement since the project began. Different columns, chromatography methods, sampling procedures and characterization standards have been tested.

2.4. Modelling Tools

Grey-Box Models were used to complete this work. An overview of the model graphic user interface, with the inputs and outputs, is presented in Appendix A.

Chapter 3: Comparison of Multi-Component Kinetic Relations on Bubbling Fluidized-Bed Woody Biomass Fast Pyrolysis Reactor Model Performance

The current chapter is a manuscript prepared for refereed journal publication.

Johnny Matta[a*], Benjamin Bronson[b], Peter E.G. Gogolek[b]
Jules Thibault[a], Poupak Mehrani[a**]

[a]Department of Chemical and Biological Engineering, University of Ottawa
161 Louis Pasteur Street, Ottawa, ON, K1N 6N5, Canada

[b]Natural Resources Canada, CanmetENERGY
1 Haanel Drive, Ottawa, Ontario, K1A 1M1, Canada

* T: 1-613-562-5800 Ext. 8852; E: jmatta@uottawa.ca
**T: 1-613-562-5800 Ext. 6098; F: 1-613-562-5172; E: poupak.mehrani@uottawa.ca

Abstract
Modelling of the thermochemical conversion process of biomass has been widely studied in the past. However, most of the work pertaining to fast pyrolysis is focused on modelling the devolatilization of a single biomass particle. Only a few works have been devoted to modelling pyrolysis at the bubbling fluidized-bed reactor level. Undeniably the most significant shortfalls of these models lie within the implemented devolatilization schemes. Modelling studies in general tend to establish complex hydrodynamic models. However, only simple single-component mechanisms without product specification are used. This work examines the application of devolatilization schemes not only for biomass fast pyrolysis product quantity but also liquid product composition (quality). In particular, the work explores the improvements in multi-step and multi-component fast pyrolysis kinetic mechanisms and compares their impacts on reactor measurable outputs such as product (bio-oil, gas and biochar) yields and distinctive compositional values. Three distinct biomass feedstocks were compared: hardwood sawdust, powdered cellulose and a bark-laden wood processing residue. The effect of biomass composition, feedstock ash content and operating temperatures on the modelled and experimental results are presented and discussed. A classification strategy of component yields is suggested for comparison with the experimental results collected from a 5 – 10 kg/h fluidized bed rapid pyrolysis unit at a fixed operating temperature and gas residence time. Additionally, mechanism modifications have been implemented to minimize the differences in component class outputs and increase the accuracy of model predictions. Results generated from this research will help in further understanding bio-oil yields and properties from pilot-scale fast pyrolysis processes in a cost and time-effective fashion.

Keywords: Biomass Fast Pyrolysis, Reactor Modelling, Multi-Component Devolatilization Kinetic Schemes

3.1. Introduction

Over the past century the majority of energy consumed has originated from fossil sources, primarily coal, oil, and natural gas. However, with the rise of global energy demands, the environmental impact of fossil fuels and concerns of their depletion, the importance of finding cleaner, renewable alternatives for energy production is significantly growing. Among current developments in the field of renewable energy, the exploitation of biomass for the production of bioenergy and biofuels is proving to be a promising alternative. Biomass is a renewable energy resource derived from the carbonaceous waste of various human and natural activities [4]. It could be of various types including: forestry crops and residues (wood, bark), agriculture crops and residues (straw, stover) and parts of municipal solid wastes, to name a few. Bioenergy generated from biomass offers several advantages over energy produced from fossil sources. For one thing, biomass is considered to be a carbon neutral energy source. Although there are many barriers to the increased use of biomass as an energy source in developed nations such as the low energy density of biomass, the large variability in resources and supply, the cost of transport, storage, and handling systems, and the lack of commercial demonstration of conversion technologies due to costly initial investments [10], there can be a long-term environmental advantage by replacing fossil fuels in energy production with biomass in order to reduce net greenhouse gas emissions.

Biomass can play a major role in reducing the reliance on fossil fuels by making use of thermochemical conversion technologies. Thermochemical conversion involves deconstructing biomass and upgrading the resulting intermediates into a range of fuels and other products. Research in fast thermochemical conversion processes commonly focuses on the production of either gaseous intermediates or liquid intermediates [55]. In fact, biomass can be promptly heated to 450 °C-600 °C in the absence of oxygen to ultimately produce a liquid intermediate termed bio-oil or pyrolysis oil [14]. This thermochemical conversion process is called fast pyrolysis. Under these conditions, organic vapours, also termed pyrolysis gases, are initially produced and are rapidly quenched to yield the pyrolysis oil. Non-condensable gases and biochar are also products of the thermal decomposition of biomass. These by-products can be used in combustion practices and improve the efficiency of the energy required to recover bio-oil. The

gas phase consists mainly of CO_2, CO, and CH_4, as well as traces of H_2 and C_2-C_3 compounds [11].

With further treatment, such as hydroprocessing, separation and fractionation, the bio-oil may be upgraded into a finished fuel suitable for a wide variety of applications including biofuels, biomaterials and chemicals. The bio-oil can also be used, directly or with minimal treatment, for heat and electricity generation just as solid biomass fuels. Typically, 60-75 wt% of the feedstock is converted into bio-oil [14] which can have a volumetric energetic density of up to 20 times higher than the original biomass [13]. Bio-oil produced from fast pyrolysis can be a uniform, single phase liquid or it can separate into multiple phases depending on various factors including feedstock moisture, feedstock extractives, production conditions and reactor design Often, when a non-uniform bio-oil is produced, it consists of a water-rich aqueous phase containing a variety of highly water soluble oxygenated organic compounds and an organic-rich phase which contains insoluble heavy organic species [15], each of which will be better suited to different applications. While the production of bio-oil may seem attractive, the liquid has some distinct characteristics that traditional fossil fuels do not share. Importantly, bio-oil exhibits a thermal instability whereby exposure to elevated temperatures may cause separation and solidification of the bio-oil or some fraction of it. The nature and reactivity of the polar oxygen-containing functional groups in the oxygenated components is reported to be the main cause for the unstable character of the bio-oil. Coking on burner nozzles for the combustion of the bio-oil or coking upon the injection into hot catalysts beds for the upgrading of bio-oil are frequently observed problems [56].In addition to the thermal instability exhibited at the temperatures of combustion equipment or catalyst beds, polymerization of certain components at room temperature causes an increase in fluid viscosity or cause phase separation over the course of months which is problematic for long-term bio-oil storage [57]. Finally, the reaction products from the thermal degradation of the original biomass constituents include organic acids, rendering the bio-oil acidic in nature.

Further development on the production of bio-oil with lower oxygenated organic compounds, lower average molecular weight, less acidic character, or the optimization for the production of chemical co-products could improve the economics of the fast pyrolysis process.

Yet, investigating the effect of prime operating parameters on fast pyrolysis yields at representative reactor configurations is very labour intensive. As such, numerical modelling has become an extremely important tool for reactor design and experimental data interpretation. By using accurate models, reactor performance can be predicted in a cost and time-effective fashion. Admittedly, due the quick nature of biomass fast pyrolysis, a model's predicted product yields are greatly affected by the formulations of the biomass devolatilization schemes. The goal of this work is to review and test the extensions of advanced multi-component and multi-step devolatilization schemes and compare their effects on reactor measurable outputs such as product (bio-oil, gas and biochar) yields and distinctive compositional values.

3.2. Biomass Fast Pyrolysis Devolatilization Schemes

3.2.1. Challenges of Biomass Fast Pyrolysis Kinetic Mechanism Formulation

The modelling of the thermochemical conversion of biomass in practical systems entails for a strong interaction between chemical and physical processes. Transport phenomena in various types of reactors are well documented but there is a need for an appropriate description of reaction kinetics in these systems. The variety and complexity of reaction schemes for biomass fast pyrolysis make the kinetic modelling an interesting and challenging study. In fact, there exist certain difficulties in reaching a clear consensus for defining intrinsic kinetic pathways and equation constants [58]. Since the mid-late 20^{th} century, several variations of the devolatilization mechanisms have been proposed [30,59–73]. Undoubtedly, one of the largest concerns in the analysis of kinetic data is the validity and reproducibility of the kinetic constants for general application. Modelling the kinetics of biomass fast pyrolysis is a challenge because of the variety in raw materials involved, the inconsistencies in experimental apparatuses and the wide range of experimental operating conditions used [74]. In fact, several literature sources have consecutively used different apparatuses with variable heating procedures to study biomass component decomposition over narrow temperature ranges; most of which have reported problems from systematic errors in comparing the applied methods [30]. However, recent advancements in thermogravimetric technology has allowed for the analysis of sample devolatilization over larger (and higher) temperature ranges, refining kinetic data comparisons. Another major difficulty encountered in carrying out measurements of sample weight loss for

kinetic equation fitting procedures is the exclusion of heat transfer limitations to obtain data under pure kinetic control. Particularly, experimental deviations in sample size and heating rates present non-negligible effects of particle internal and external heat-transfer resistances. Gronli et al. [72] attributed the discrepancies of different experimental results primarily to variations in the "thermal lag" of the instruments used; which is directly correlated to the different heating rates applied and sample sizes used. In addition, each type of biomass has a unique composition with specific physiochemical properties which will greatly alter kinetic behaviour [75] and present limitations in terms of formulating general pyrolysis mechanisms.

3.2.2. Single-Component Mechanisms

The simplest descriptions of the thermal decomposition of woody biomass are based on the single-component reaction mechanism such as the one presented in Figure 18 [62,64–69].

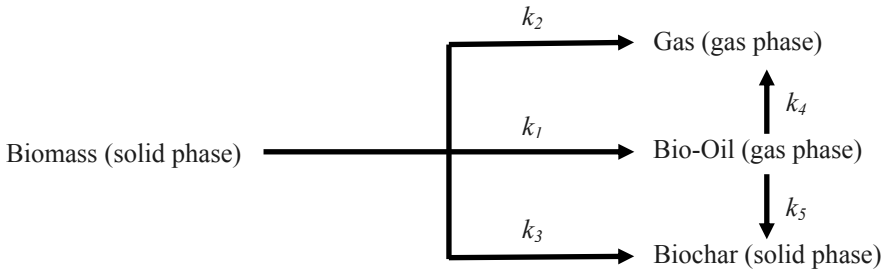

Figure 18: Single-Component and Single-Step Mechanism of Woody Biomass Pyrolysis [62]

Typically, mechanisms are associated with three lumped product classes namely: biochar, bio-oil (or organic liquid) and gas. This product classification has become a standard over the years and allows for a basic assessment of their related formation rates. The majority of kinetic data is expressed using an irreversible Arrhenius dependence on temperature. This includes the activation energy and pre-exponential factor parameters, and a linear or power-law dependence on the single-component mass concentration. Interestingly, this simple description of the devolatilization of wood is most appropriate for faster heating rates (as encountered in fast pyrolysis processes) since the individual peaks observed in the degradation rate analyses, representing the devolatilization of the different constituent major biomass polymers (hemicelluloses, cellulose, and lignin), tend to merge with the increase in heating rate [11].

However, they are largely limited in terms of flexibility since the kinetics constants have been derived for a specific type of biomass. As shown in [30], there is significant variance between the predictions of the different kinetic data sets likely due to the fact that different types of woods were used in each of the experiments for which the kinetic expressions were derived.

Some mechanisms have been extended to include additional steps accounting for secondary reactions. These are known as "multi-step" devolatilization mechanisms. For instance, at higher temperatures, secondary reactions of bio-oil vapours become more active which could, for example, result in the increase of light permanent gases produced. Generally, modelling secondary reactions would require a large number of chemical reactions to describe the chemical activity due to the complex chemical structure of bio-oil vapours. In fact, experimental difficulties have limited quantitative understanding of the products and therefore simple mechanisms have been developed. One such mechanism is that by Antal [59]. The reactions may be classified as homogeneous (in the gas phase) or heterogeneous (on the particle surface) and include processes such as cracking, partial oxidation, re-polymerization, and condensation [76]. Compared to primary reactions, secondary reactions are not as well studied and kinetic parameters have typically only been derived for the cracking process. This is due to the fact that differences in secondary reactivity are caused by differences in primary feedstock degradation. Recently, more in-depth analyses of the secondary reactions of pyrolysis products were performed. For instance, Shin et al. [77] presented secondary and tertiary reactions on a few of the main bio-oil products: 5-hydroxymethylfurfural, levoglucosan and hydroxyacetaldehyde.

3.2.3. Multi-Component Mechanisms

A different description of the thermal decomposition of woody biomass is based on a multi-component reaction mechanism. In this mechanism, each reaction takes into account the dynamics of several pseudo-components in the measured weight loss curves. In the majority of cases, such components correspond to cellulose, hemicellulose and lignin. Generally, the decomposition of the volatile fractions of pseudo-components is modelled as parallel reactions. Although, models with consecutive reactions, owing to significant overlap, have also been proposed [11]. Furthermore, it is most commonly assumed that there exists no interaction between each pseudo-component in the devolatilization scheme. In fact, process simulations

show that cellulose and hemicellulose decompose rapidly over a relatively narrow range of temperatures whereas lignin decomposes slowly over a broad range of temperatures [78]. However, there have been claims of cellulose-hemicellulose and cellulose-lignin interactions in wood pyrolysis at higher temperatures [79].

One of the more distinguishable mechanisms is the one proposed by Miller & Bellan (1996) [80] (see Figure 19) based on the superimposition of the different lignocellulosic component contributions. It has been pieced together from the previous works of [61,65,73] which studied individual biomass components, intermediate steps and possible interactions. As this mechanism is not based on experiments but yet based on a re-examination of literature data, it remains one of the few attempts to produce a general and flexible mechanism for woody biomass fast pyrolysis whilst being capable of making robust predictions for a variety of conditions and feedstocks [80]. The overall trend in the devolatilization of cellulose remains relatively unchanged whereas higher activation energies of hemicellulose degradation are reported. In this case, it is not unusual for multi-component mechanisms derived with higher heating rates to include additional steps, such as more parallel reactions, to improve the accuracy of predictions [11].

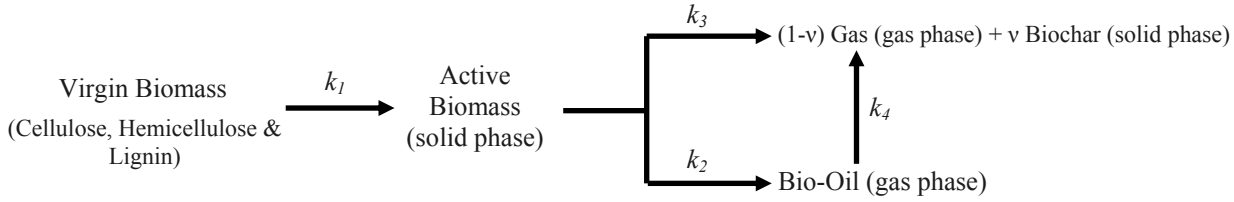

Figure 19: A Proposed Multi-Component Pyrolysis Mechanism by Miller & Bellan [80]

Table 7: Kinetic Constants for Miller & Bellan (1996) Mechanism

Component	Kinetic coefficients	ν	A (s^{-1})	E (kJ/mol)	ΔH^0_R [kJ/kg]
Primary Reactions (Devolatilization of Lignocellulosic Components)					
Cellulose	k_{1C}	0.35	$2.8x10^{19}$	242.4	0
	k_{2C}		$3.28x10^{14}$	196.5	418
	k_{3C}		$1.3x10^{10}$	150.5	418
Hemicellulose	k_{1H}	0.6	$2.1x10^{16}$	186.7	0
	k_{2H}		$8.75x10^{15}$	202.4	418
	k_{3H}		$2.6x10^{11}$	145.7	418
Lignin	k_{1L}	0.75	$9.6x10^{8}$	107.6	0
	k_{2L}		$1.5x10^{9}$	143.8	418
	k_{3L}		$7.7x10^{6}$	111.4	418
Secondary Reactions (Bio-Oil Cracking)					
Bio-Oil	k_4	-	$4.28x10^{6}$	108.0	-42
Additional Reaction (Evaporation of Biomass Moisture Content)					
Water	k_E	-	$5.13x10^{10}$	88	2244

- The evaporation of biomass moisture has been added according to the works of Sreekanth et al. [40]

The extension of the multi-component and multi-step kinetic mechanisms and the derivation of more comprehensive kinetic schemes including the specification of the products are desired and have been the focus of some researchers [11,58,61,63,65,73,74,77,80–82]. Among all of the lignocellulosic components of biomass, the thermal decomposition of cellulose is mostly investigated and best understood. Several mechanisms of cellulose pyrolysis are widely accepted to represent the reaction pathway, yielding specific products and defining the effect of temperature and heating rate [83]. These mechanisms include the works of [12,63], among many others. Similar mechanistic works in the devolatilization of hemicellulose and lignin also exist [58,81]. Indeed, reaction schemes predicting the sum of these lignocellulosic component contributions are available. The Ranzi mechanism, initially proposed by Ranzi et al. [74], is an extension of the multi-component kinetic mechanism from Miller & Bellan [80] and defines the rates and the stoichiometry of several lumped reactions, including primary devolatilization reactions and successive gas phase reactions, for each of the aforementioned reference components. Considering that typical pyrolysis oils consist of at least hundreds of chemical compounds and that this representation of the bio-oil may seem simplistic, the Ranzi mechanism (and its derivatives) remains one of the only kinetic schemes to attempt to represent the bio-oil to that extent. The kinetic constants have recently been modified in order to account for newly available experimental data [82] (see Table 8). The latest mechanism covers primary pyrolysis and secondary gas phase reactions, but does not include heterogeneous reactions between char

and gas. Catalytic effects of certain components, such as ash minerals and extractives, as well as the evaporation of moisture in biomass have been neglected. However, certain derivatives such as those presented by [84–86] have partially dealt with these limitations. For the Ranzi mechanism, the feedstock must be characterized in terms of 3 additional element-rich lignin components: carbon-rich (LIGC), hydrogen-rich (LIGH) and oxygen-rich (LIGO). The purpose is to account for the structure irregularities of lignin molecules. Though, characterizing the biomass in term of these reference components is challenging and may not always be possible without thorough biochemical analyses. A characterization method using the ultimate analysis of the feedstock has been proposed in [87].

Table 8: Kinetics Expressions for the 2014 Ranzi Reaction Scheme [82]

ID	Reaction	Kinetic Expressions [s^{-1}]	ΔH^0_R [kJ/kg]
1	CELL→CELLA	4 x 10^{13}exp (-188.36/RT)	0
2	CELLA→0.8HAA+0.2GLYOX+0.1C_2H_4O+0.25HMFU+0.3C_3H_6O+0.21CO_2 +0.1H_2+0.4CH_2O+0.16CO+0.83H_2O+0.02HCOOH+0.61Char	0.5×10^9 exp (-121.39/RT)	620
3	CELLA→LVG	1.8×T exp (-41.86/RT)	364
4	CELL→5H_2O+6Char	4×10^7 exp (-129.76RT)	-1913
5	HCE→0.4HCE1+0.6HCE2	0.33×10^{10}exp (-129.76/RT)	100
6	HCE1→0.025H_2O+0.5CO_2+0.025HCOOH+0.5CO+0.8CH_2O+0.125C_2H_5OH +0.1CH_3OH+0.25C_2H_4+0.125G{H_2}+0.275G{CO_2}+0.4G{COH_2} +0.45G{CH_3OH}+0.325G{CH_4}+0.875Char	1×10^9 exp (-133.95/RT)	-92
7	HCE1→0.25H_2O+0.5CO_2+0.05HCOOH+0.3CO+0.15G{CO}+0.25G{CO_2} +1.7G{COH_2}+0.625G{CH_4}+0.375G{C_2H_4}+0.675Char	0.05×T exp (-33.49/RT)	-1860
8	HCE1→XYLAN	0.9×T exp (-46.04/RT)	588
9	HCE2→0.2H_2O+0.175CO+0.275CO_2+0.5CH_2O+0.1C_2H_5OH+0.2HAA +0.025HCOOH+0.25G{CH_4}+0.3G{CH_3OH}+0.275G{C_2H_4}+0.4G{CO_2}+ 0.925G{COH_2}+Char	0.33×10^{10} exp (-138.13/RT)	212
10	LIGC→0.35LIGCC+0.1COUMARYL+0.08PHENOL+0.41C_2H_4+H_2O +0.3CH_2O+0.32CO +0.7G{COH_2}+0.495 G{CH_4}+5.735Char	1.33×10^{15} exp (-203.01/RT)	-490
11	LIGH→LIGOH+C_3H_6O	0.67×10^{13} exp (-156.97/RT)	100
12	LIGO→LIGOH+G{CO_2}	0.33×10^9 exp (-106.74/RT)	446
13	LIGCC→0.3COUMARYL+0.2PHENOL+0.35HAA+0.7H_2O+0.4CO +0.65G{CH_4}+0.6G{C_2H_4}+G{COH_2}+0.4G{CO}+6.75Char	1.6×10^6 exp (-131.85/RT)	-503
14	LIGOH→LIG+0.15G{H_2}+0.9H_2O+0.1CH_4+0.5CH_3OH+0.5G{CH_3OH} +0.05CO_2+0.3CO+G{CO}+0.05HCOOH+0.6G{COH_2}+0.35G{CH_4} +0.2G{C_2H_4}+4.15Char	0.5×10^8 exp (-125.58/RT)	-120
15	LIGOH→1.5H_2O+0.5CO+0.1CH_4+0.5G{H_2}+1.6G{CO}+3.9G{COH_2} +1.65G{CH_4}+0.3 G{C_2H_4}+0.5G{CH_3OH} +10.15Char	33 exp (-62.79/RT)	-1604

16	LIG→FE2MACR	2.4×T exp (-50.23/RT)	686
17	LIG→0.95H_2O+0.2CH_2O+0.4CH_3OH+CO+0.2CH_4+0.05HCOOH +0.45G{CO}+0.5G{COH_2}+0.4G{CH_4}+0.65G{C_2H_4}+0.2C_2H_4O +0.2C_3H_6O+5.5Char	0.4×10^{9} exp (-125.58/RT)	-470
18	LIG→0.6H_2O+0.4CO+0.2CH_4+0.4CH_2O+0.2G{CO}+0.4G{CH_4} +0.5G{C_2H_4}+0.4G{CH_3OH}+2G{COH_2}+6Char	0.083×T×exp (-33.49/RT)	-1663
19	G{CO_2}→CO_2	1×10^{6} exp (-100.46/RT)	-1814
20	G{CO}→CO	0.5×10^{13} exp (-209.29/RT)	-2000
21	G{COH_2}→CO+H_2	5×10^{11} exp (-297.20/RT)	6778
22	G{H_2}→H_2	5×10^{11} exp (-313.94/RT)	0
23,24	G{CH_4}→CH_4 G{C_2H_4}→C_2H_4	0.5×10^{13}exp (-300.13/RT)	0
25	G{CH_3OH }→CH_3OH	0.2×10^{13}exp (-209.29/RT)	0
26	H_2OB→H_2OG	5.13×10^{10}exp (-88/RT)	2244

- Activation energy units are kJ/mol
- The evaporation of water (ID 26) has been added according to the works of Sreekanth et al. [40]

3.3. Experimental Setup and Reactor Modelling

The ultimate goal of this work is to test the application and performance of these complex multi-component and multi-step devolatilization schemes. A one-dimensional Grey-Box Model (GBM) has been developed at the University of Ottawa and was applied to the Bell's Corners Complex (BCC) fluidized bed fast pyrolysis unit located at NRCan CanmetENERGY (Ottawa, ON) for testing and validation. The model was programmed using the Microsoft Visual Basic for Applications software. Details concerning reactor parameters and general operating conditions are presented in Figure 20. GBMs avoid the details and complexity of gas-solid dynamics of Computational Fluid-Dynamic Models (CFDMs) or white-box models (WBMs) but still manage to incorporate simplified multiphase flow patterns within the bed, as opposed to Black-Box Models (BBMs) (see Figure 21). They are essentially derivatives to Fluidization Models (FMs). The objective of the developed GBM is to provide individual component concentrations and overall yields of the pyrolysis products by solving a set of component mass and heat balances over a pre-defined grid. The advantages of GBMs are that they are very easy to use, there are few inputs required and model runtime is very fast. In fact, compared to Fluidization Models (FMs) and Computational Fluid-Dynamic Models (CFDMs), where multiple phases are treated and

constitutive relations describe gas and solid flow patterns and interactions, the GBM can surprisingly give good predictions.

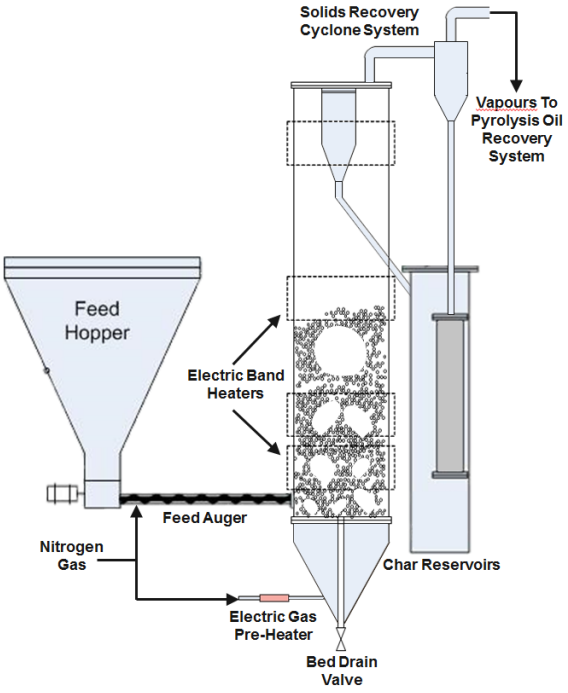

Operating Fluidization Regime	Bubbling
Reactor Internal Diameter	0.1 m
Reactor Height	1.0 m
Operating Pressure	Atmospheric
Operating Temperature	400-550 °C
Typical Fluidizing gas flow	~0.0025 SCMPS
Average Fuel Capacity	5.4-6.5 kg/h
Average Fuel Usage per Run	25 kg
Nominal Feed Particle Size	0 - 5 mm
Fluidizing Medium	Nitrogen
Bed Material Type	32-B4 Olivine Sand
Bed Material Size	~600 µm
Bed Material Mass	~3.75 kg
Bed Particle Density	2830 kg/m^3
Bed Bulk Density	1515 kg/m^3

Figure 20: Fast Pyrolysis Fluidized Bed Reactor Parameters and General Operating Conditions (reactor located at NRCan CanmetENERGY)

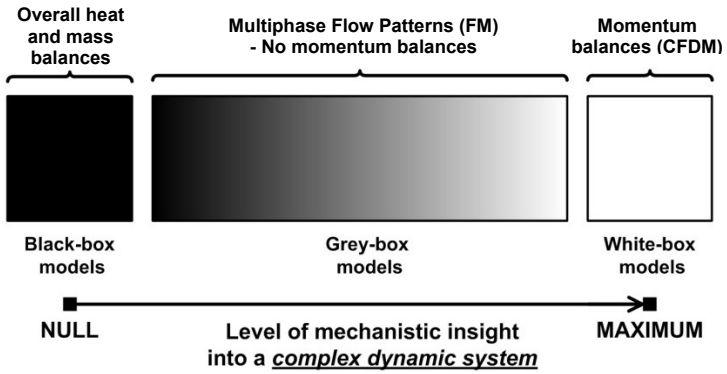

Figure 21: Approaches to Modelling Bubbling Fluidized Bed Reactors (adapted from [88])

Figure 22 presents the parameters used to solve the first control volume (cell) on the pre-defined grid as well as the sequential modular approach used to model the dense bed as a series of finite CSTRs. Successive cells use the inputs of the previous cells and follow the same procedure.

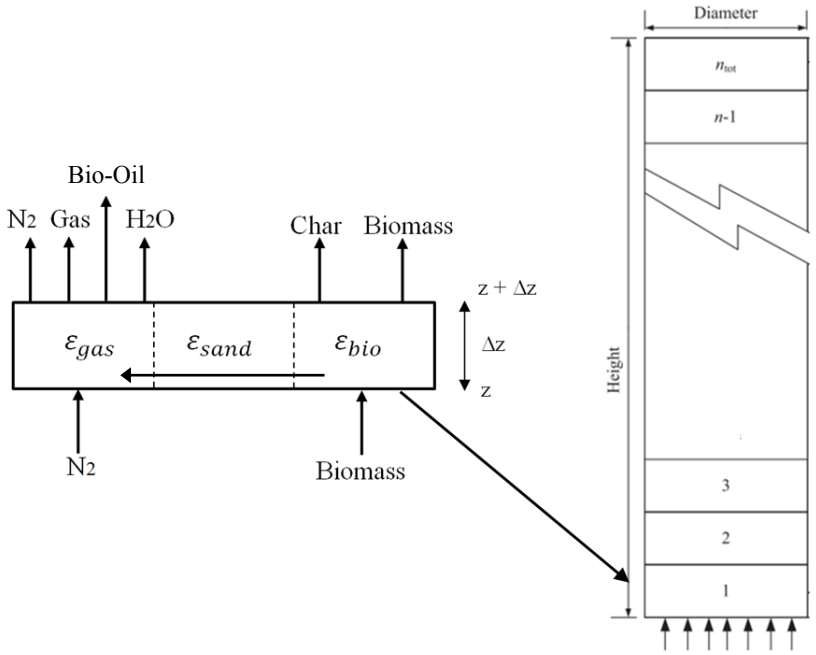

Figure 22: Inputs and Outputs of First Control Volume (Cell) in GBM Grid

A few of the underlying assumptions of the current model include:

- Wood particles are perfectly spherical and do not shrink
- Uniform distribution of porosity
- Isobaric operation and no significant effects of in-bed hydrodynamics or freeboard
- Negligible interaction of hydrodynamic and reaction kinetic sub-models
- Non-reactive effect of water and ash species
- Negligible mass and heat transfer resistances

According to Xiong et al. [43], multi-component reaction schemes which also considered secondary reactions are found to give better predictions compared to simple single-component schemes. For this reason, the following section will examine the Miller and Bellan [80] and Ranzi et al. [82] multi-component mechanism performance. A series of experiments were conducted at customary fast pyrolysis temperatures (400-500 °C) using three different woody biomass feedstocks. The temperature range has been selected to minimize the extent of secondary bio-oil cracking reactions at higher temperatures while still examining char forming potential at lower temperatures [25]. The first and second feedstocks were maple-derived hardwood sawdust (HWS) and Solka-Floc 200 MO Powdered Cellulose (SFPC). These

feedstocks have low ash content, and were initially tested to limit the extent of secondary inorganic catalytic reactions and their effect on yields. Accordingly, the third feedstock, a bark-rich wood processing residue called Interior Hog Fines (IHF), was selected for its similar physical properties yet noticeably larger ash content for the purpose of examining the extent of these secondary inorganic catalytic reactions. Some relevant properties are presented in Table 9.

Table 9: Biomass Feedstock Properties

Feedstock Properties	HWS Values	SFPC Values	IHF Values
Mean Particle Diameter	~1 mm	50 -150 µm	~1 mm
Particle Density	~500 kg/m³	~435 kg/m³	~500 kg/m³
Proximate Analysis			
Moisture Content	7.27 wt%	5.97 wt%	10.45 wt%
Ash Content	0.36 wt%	0.19 wt%	10.69 wt%
Volatiles Content	79.04 wt%	84.8 wt%	64.01 wt%
Fixed Carbon Content	13.33 wt%	9.04 wt%	14.85 wt%
Biochemical Analysis			
Cellulose Composition	40 wt%	100 wt%	27 wt%
Hemicellulose Composition	38 wt%	0 wt%	23 wt%
Lignin Composition	22 wt%	0 wt%	50 wt%

3.4. Results and Discussion

3.4.1. Examining the Performance of Original Multi-Component and Multi-Step Mechanisms

3.4.1.1. Mechanism Excluding Product Specification

3.4.1.1.1. Effect of Feedstock Composition

The biomass fast pyrolysis mechanism proposed by Miller & Bellan (1996) which excludes product specification was encoded within the GBM and its performance was compared to experimental yields. For the first experimental run, a HWS feedstock was fed at 6.5 kg/h ash-free into the BCC fast pyrolysis unit containing 3.8 kg of 32-B4 Olivine sand and operating at a temperature of 480 ºC and fluidization flow rate of 2.54×10^{-3} SCMPS. The summary of the experimental yields along with the GBM predictions is presented in Table 10. Experimental yields fall within typical ranges reported for woody feedstocks with low ash content. Impressively, the non-condensable gas and char yield differences were found to be below approximately 3 %. The experimental yield for bio-oil was taken as the summation of condensed organic vapours and the fraction of organic vapours suspended as liquid droplets in the gas phase termed “aerosols”. Aerosols are typically generated by the reactive boiling ejection of organic vapours from the molten intermediate lignocellulosic liquid compounds; molten cellulose being the prime contributor [84,86]. The rapid cooling rate of the quench system also favours the formation of small liquid droplets. Though it was found to be slightly higher than the difference for gas and char, the evaluated difference in bio-oil yield was small and its value is likely attributed to the incomplete experimental mass balance closure originating from imperfect bio-oil recovery procedures and accumulation in cleansing locations such as particulate filter housings. Finally, the yield of “unallocated” material obtained from the mass of solid deposits and residues recovered after the experiments, was said to be linked to the difference in char yields. However, due to the nature of experimental fast pyrolysis and the variability in commonly reported experimental yields, the claim was deemed statistically insignificant.

Table 10: Performance of the Miller & Bellan (1996) Mechanism at 480 ºC using HWS

Experimental Yield			Model Yield		Difference
Product	**Yield (wt%)**		**Product**	**Yield (wt%)**	**(Model – Experimental)**
Recovered Bio-Oil	50.7 %	72.1%	Bio-Oil	76.87 %	4.77 %
Bio-Oil as Aerosols	21.4 %				
Gas	12.5 %		Gas	10.5 %	-1.0 %
Char	9.1 %		Char	12.3 %	3.2 %
Unallocated	3.9 %		Ash by difference	0.33 %	- Not applicable -
Total	96.6 %		Total	100 %	3.4 %

- HWS ash content neglected in differences (< 0.36 %)

An attempt at studying the effect of biomass composition on product yields and testing the applicability of the multi-component nature of the mechanism was performed with pure SFPC. The feedstock was fed at 5.4 kg/h ash-free into the BCC fast pyrolysis unit containing 3.8 kg of 32-B4 Olivine sand and operating at a temperature of 480 ºC and fluidization flow rate of $2.54x10^{-3}$ SCMPS. The data is presented in Table 11. Similar gas and char differences to those reported for the HWS runs were observed. Though, considering the lower mass balance closure for the experimental SFPC run, a larger difference in bio-oil yields was obtained. In addition, both the GBM and experimental data presented lower char yields. Comparable yields were reported for powdered cellulose fast pyrolysis [89]. Albeit, the reported value for char is slightly larger than seen in [89]. Due to the fine nature of the cellulose powder, a fraction of what is recovered as "char" may in fact contain low quantities of volatile cellulosic matter that have been ejected from the bed during operation. In fact, a proximate analysis of the char provided slightly larger volatile matter yields. As was previously deliberated, these differences are relatively insignificant. Admittedly, it can be concluded that without the presence of considerable lignin content in the feed, lower char and higher bio-oil yields can be achieved.

Table 11: Performance of the Miller & Bellan (1996) Mechanism at 480 ºC using SFPC

Experimental Yield			Model Yield		Difference
Product	**Yield (wt%)**		**Product**	**Yield (wt%)**	**(Model – Experimental)**
Recovered Bio-Oil	64.5 %	75.8 %	Bio-Oil	87.17 %	11.37 %
Bio-Oil as Aerosols	11.3 %				
Gas	8.7 %		Gas	9 %	0.3 %
Char	5.6 %		Char	3.7 %	-1.9 %
Unallocated	1.7 %		Ash by difference	0.13 %	- Not applicable -
Total	91.8 %		Total	100 %	8.2 %

- SFPC ash content neglected in differences (< 0.36 %)

One of the shortcomings of the Miller & Bellan (1996) mechanism is that it does not account for the influence of salts and minerals in the feedstock. To examine the effect of inorganics, a IHF feedstock was fed at 6.5 kg/h ash-free into the BCC fast pyrolysis unit containing 3.8 kg of 32-B4 Olivine sand and operating at a temperature of 480 ºC and fluidization flow rate of 2.54×10^{-3} SCMPS. As seen in Table 12, there is a slight difference obtained in char yields. Although the char yields are larger than those observed with HWS and SFPC feedstocks, due to the higher lignin fraction in the feed, the mechanism only slightly underestimates the char yield when considering the ash fraction. The ash fraction in the IHF feedstock is not negligible and must be considered since the char fraction measured experimentally contains most of the ash from the feed material. The slight difference in char yields indicates there is catalytic activity of the inorganics promoting the rate of secondary charring reactions in the pyrolysis unit. The extent of the difference is subject to further studies. Concurrently, the bio-oil yield is also slightly overestimated as a result of the lack of charring reactions and incomplete experimental mass balance closure.

Table 12: Performance of the Miller & Bellan (1996) Mechanism at 480 ºC using IHF

Experimental Yield			Model Yield		Difference
Product	**Yield (wt%)**		**Product**	**Yield (wt%)**	**(Model – Experimental)**
Recovered Bio-Oil	45.1 %	49.2 %	Bio-Oil	62.76 %	13.56 %
Bio-Oil as Aerosols	4.1 %				
Gas	10.2 %		Gas	9.9 %	-0.3 %
Char	29.6 %		Char	16.7 %	-12.9 %
Unallocated	2.1 %		Ash by difference	10.64 %	- Not applicable -
Total	91.1 %		Total	100 %	8.9 %

3.4.1.1.2. Effect of Operating Temperature

Since the fast pyrolysis of biomass is principally an assemblage of heat-induced reactions, one of the most sensitive independent variables is the pyrolysis reactor temperature. GBM yields over a broad range of temperatures using the Miller & Bellan (1996) mechanism have been illustrated in Figure 23. As can be seen, there is a considerable variation in product yields as reactor temperature changes. Evidently, an operating temperature between 460-520 ºC is suitable for maximizing the production of bio-oil whereas higher temperatures are not favored. In fact, secondary bio-oil cracking is favored at higher temperatures, which is displayed by the increase in gas yield above 620 ºC. On the other hand, the increase in char-forming reactions is prominent at lower temperatures. As the decomposition of lignin is gradual over a wide and early temperature range as opposed to cellulose and hemicellulose [90], char yields of up to 21 wt% have been observed with HWS. Interestingly, the observed trends are in accordance with WBM predictions observed in literature [43,89,91].

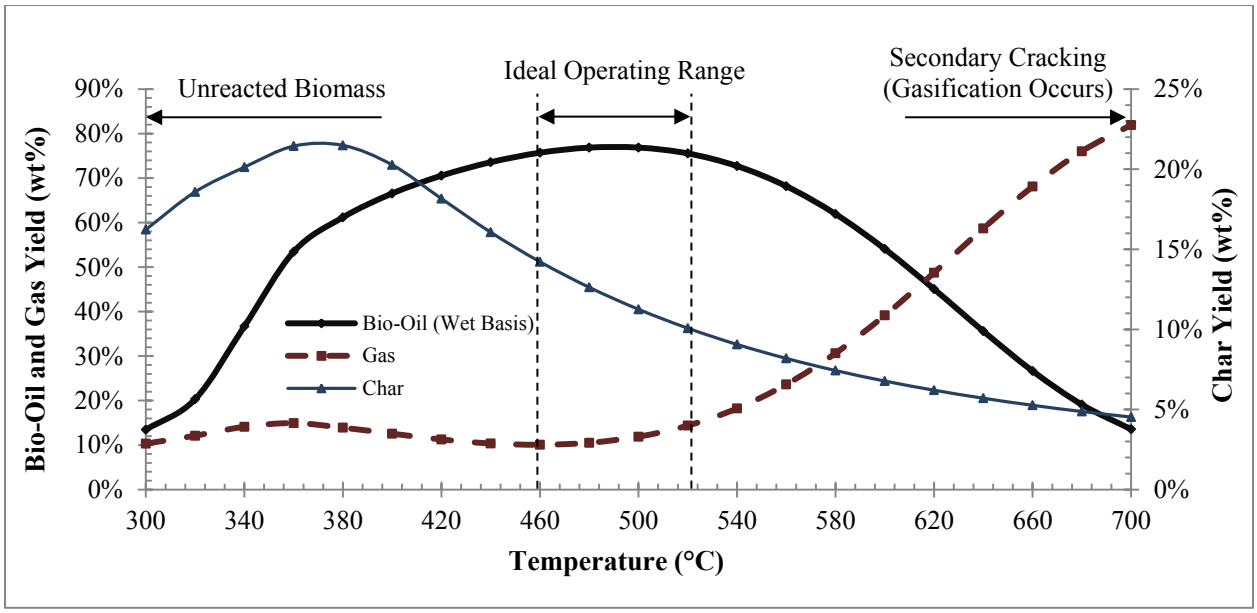

Figure 23: Effect of Temperature on Fast Pyrolysis Product Yields for HWS; Data Generated using the Miller & Bellan (1996) Mechanism

To examine the performance of the mechanism at lower temperatures, a HWS feedstock was fed at 6.5 kg/h ash-free into the BCC fast pyrolysis unit containing 3.8 kg of 32-B4 Olivine sand and operating at a temperature of 400 ºC and fluidization flow rate of 2.88×10^{-3} SCMPS. The data is presented in Table 13 with conforming results.

Table 13: Performance of the Miller & Bellan (1996) Mechanism at 400 ºC using HWS

Experimental Yield			**Model Yield**		**Difference**
Product	**Yield (wt%)**		**Product**	**Yield (wt%)**	**(Model – Experimental)**
Recovered Bio-Oil	52.6 %	64.0%	Bio-Oil	66.55 %	2.55 %
Bio-Oil as Aerosols	11.4 %				
Gas	8.4 %		Gas	12.6 %	4.2 %
Char	20.5 %		Char	19.9 %	-0.6 %
Unallocated	1.8 %		Solids by difference	0.95 %	- Not applicable -
Total	94.7 %		Total	100 %	5.3 %

- HWS ash content neglected in differences (< 0.36 %)
- Solids by difference account for ash and unreacted biomass

3.4.1.2. Mechanism Including Product Specification

3.4.1.2.1. Effect of Feedstock Composition

The biomass fast pyrolysis mechanism proposed by Ranzi et al. (2014), which includes product specification, was encoded within the GBM and its performance was evaluated against experimental yields. Comparing the bio-oil component yields of the mechanism to the experimental component yields is challenging for few reasons. The main reason is the dissimilarity in the description of bio-oil sample. In fact, only a dozen components have been used to represent the entirety of bio-oil predicted by the Ranzi mechanism. Considering that typical pyrolysis oils consists of several hundreds of chemical compounds and that this representation of the bio-oil may seem simplistic, the Ranzi mechanism and its derivatives remain to be some of the only kinetic schemes to attempt to represent the bio-oil to that extent. Experimentally, the complex nature of the bio-oil mixture renders essential the use of detailed characterization techniques. For the purpose of this work, GC-MS (DB5-MS) was used and the instrument was calibrated for the characterization of 27 compounds using the NIST Chemistry WebBook database [92]. One of the most common issues with the examination of pyrolysis oils is the method and standards used for component quantification. Therefore, two steps have been proposed for the comparison procedure.

The first step in the comparison procedure is data classification. In hopes of paralleling the bio-oil components for mechanism assessment, the components were partitioned within common pyrolysis oil organic classes according to their functional groups such as: Ketones/Aldehydes, Acids/Alcohols, Furans, Sugars, Phenolics and Guaiacols/Syringols. The classification is displayed in Table 14. It was found that this arrangement of components represents relatively analogous based on an examination of the C/H/O mass content (see Figure 24) with the slight exception of Furans which are solely characterized by 5-hydroxymethyl-furfural for the Ranzi mechanism.

Table 14: Moisture-Free Classification of Bio-Oil Components for Analysis

Mechanism Classification	Experimental Classification
Sugars	
• Levoglucosan (LVG) • Xylan (XYLAN)	• Levoglucosan
Acids/Alcohols	
• Methanol (CH_3OH) • Ethanol (C_2H_5OH) • Formic Acid (HCOOH) • Hydroxy-Acetaldehyde (HAA)	• Acetic Acid • Hydroxyacetone (Acetol) • Hydroxy-acetaldehyde (Glycolaldehyde) • Acetic acid, hydroxy-, methyl ester • EUC1 • Succinic acid • Vanillic acid
Ketones/Aldehydes	
• Glyoxal (GLYOX) • Acetone/Propanal (C_3H_6O) • Acetaldehyde (C_2H_4O) • Formaldehyde (CH_2O)	• EUC2 (possibly acetaldehyde) • Acetic acid, methyl ester* • Propanoic acid, 2-oxo-, methyl ester* • 2-Cyclopenten-1-one, 2-methyl- • 2-Cyclopenten-1-one, 2-hydroxy-3-methyl- or 1,2-Cyclopentanedione, 3-methyl-
Phenolics	
• Paracoumaryl Alcohol (COUMARYL) • Phenol (PHENOL)	• Phenol • EUC3 • 1,2-benzenediol • 1,2-Benzenediol, 3-methyl- • 1,2-Benzenediol, 4-methyl-
Furans	
• 5-hydroxymethyl-furfural (HMFU)	• Furfural • Furan, tetrahydro-2,5-dimethoxy- • EUC4
Guaiacols/Syringols	
• Sinapaldehyde (FE2MACR)	• 2-methoxyphenol • Phenol, 2-methoxy-4-methyl- • 2-Methoxy-4-vinylphenol • phenol, 2,6-dimethoxy- • Eugenol* • Vanillin • Isoeugenol • Phenol, 2,6-dimethoxy-4-(2-propenyl)- • 4-Hydroxy-2-methoxycinnamaldehyde

- Experimental components identified using NIST Standard Reference Database
- EUC: Experimentally Unidentifiable Component
- * represents predicted components

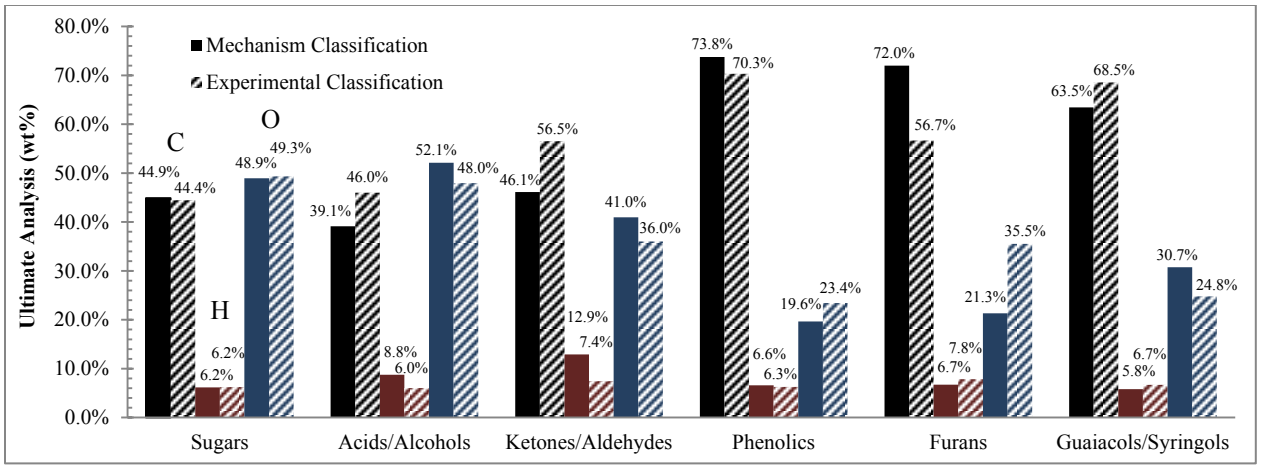

Figure 24: C/H/O Characterization of Classified Bio-Oil Components

The second step in the comparison procedure is data normalization. This step is crucial to achieve a similar basis for comparison of experimental and mechanism yields. In regards to the primary product, the bio-oil, there is a fraction of the components which is amenable to characterization and a fraction which is not. In fact, the GC-MS method only accounts for approximately 23-26 % of the bio-oil, leaving around 20-30 % of uncharacterized components. The normalization procedure allows for the consideration of this undetectable fraction in the comparison process. A fraction of the bio-oil has also been allocated to pyrolytic lignin (70 % of initial lignin content) according to suggestions from other authors [12,84,93–95]. These fractions are presented in Figure 25.

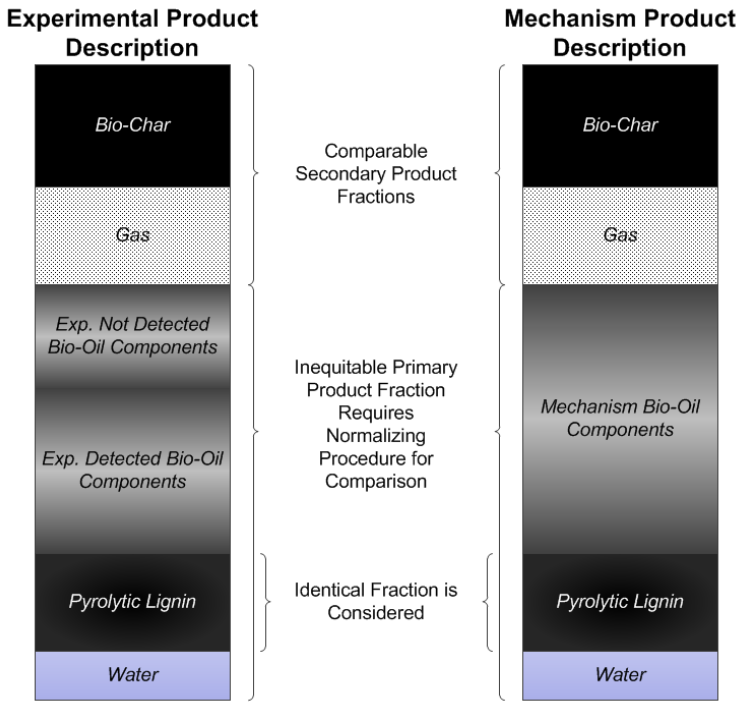

Figure 25: Primary and Secondary Fractions of Biomass Fast Pyrolysis Products

An initial attempt at evaluating the original mechanism performance was carried out using the HWS and SFPC experimental runs discussed in the previous section (see Table 15). Taking a closer look at the HWS yield summary it can be seen that the yield of char has varied at the expense of the bio-oil yield. A similar trend is observed for SFPC, though the extent is much less noticeable. In fact, for SFPC, the variation in the yield of non-condensable gases was more prominent. Comparable values have been reported in [96]. Incompletely pyrolysed biomass (IPB) is observed for HWS and has been linked to the slow devolatilization of the carbon-rich lignin derivative (LIGCC). The same phenomenon is observed for char and it has been linked to the slow evolution of trapped components making up roughly 40 % of the char and dominated by the yield of trapped formaldehyde (G{COH_2}). Interestingly, very similar total yields have been reported in the experimental work of Milhe et al. [97] for comparable temperatures. Granted, the experimental apparatus and feedstock that were used in their work limited heating rates and therefore favoured the formation of char. Considering the latter, the high yields of char has been attributed to apparent fitting of the mechanism's kinetic constants at lower heating rate experiments (unlike fast pyrolysis). This has been examined in Blondeau et al. [98] and validates the notion.

Table 15: Performance of the Ranzi et al. (2014) Mechanism at 480 ºC for Low-Ash Feedstocks

Yield Summary (wt%)		
	HWS	**SFPC**
IPB	1.85	0.00
Char	15.86	2.88
Gas	11.11	4.19
Bio-Oil	71.18	92.94

- IPB: Incompletely Pyrolysed Biomass

A look into the mechanism performance for the individual bio-oil classes is presented in Figure 26. Undoubtedly, some differences were observed in bio-oil class yields. The largest differences were found to be the overestimation of the sugar content and the underestimation of the acids/alcohols content. The yield of sugar is dominated by the production of levoglucosan, which generally tends to be larger in the devolatilization of highly cellulosic feeds. It is believed that the overestimation of the sugar content is linked to the activated cellulose transglycosylation reactions overwhelming the cellulose ring fragmentation reactions to form lower molecular weight hydroxycarbonyl components and even lower molecular weight non-condensable components. This phenomenon also explains the very high bio-oil yields and lower gas yields for the devolatilization of SFPC. In addition, a larger yield of Furans was also observed as they are mostly formed in the devolatilization of highly cellulosic material.

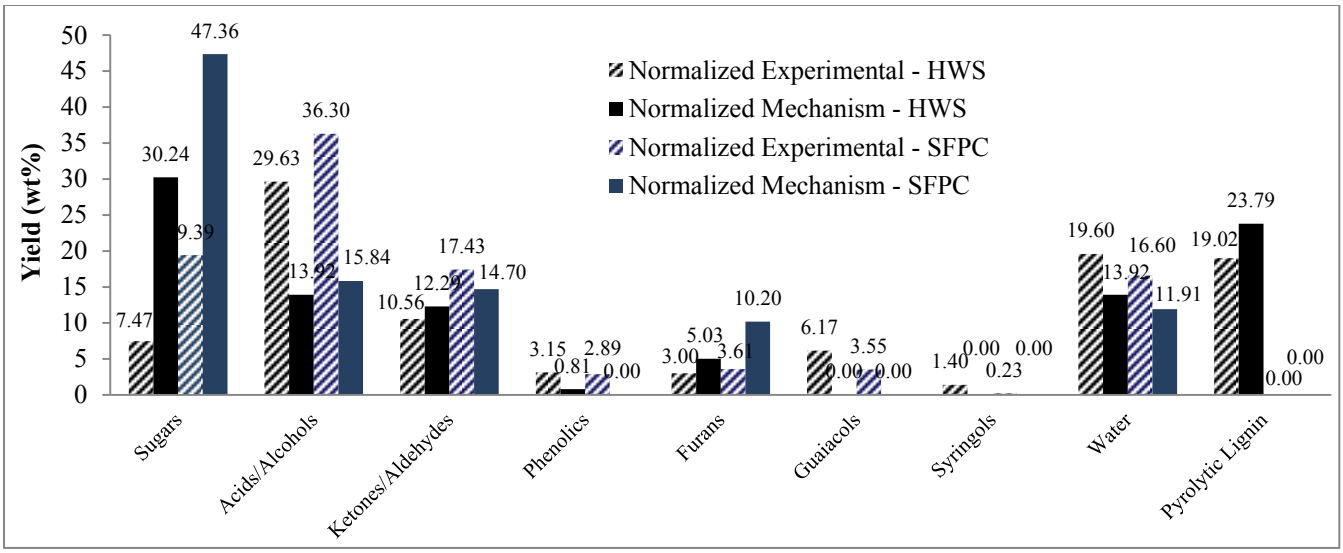

Figure 26: Comparison of Classified Specific Bio-Oil Yields

The majority of the gas fraction detected by GC-MS is allocated to carbon dioxide and carbon monoxide with the carbon dioxide yielding slightly larger amounts. Compared to output concentrations obtained with the Ranzi mechanism, there are slight differences, specifically with the CO_2 and CO yields. The extent of the difference is lower with the SFPC experiments, suggesting that the rate of CO_2 formation from the devolatilization of hemicellulose and lignin may be off. This reveals the second sign of the underperformance of the Ranzi mechanism at higher heating rates and pushes the need for fine-tuning of the stoichiometric coefficients and kinetic constants. Due to the high boiling point of acetaldehyde (relative to other gases and close to the quench temperature) and the polar nature of formaldehyde making it susceptible to solvent absorption in gas recovery process, it was presumed that their yields were incorporated within the liquid organic phase. This presumption was also reported in [84]. Therefore, the mechanism gas yields have been normalized to exclude Formaldehyde and Acetaldehyde. No CH_4 yield was reported. This is due to the uncertainty around the hydrogen and oxygen-rich lignin fractions in the feed. However, varying these fractions provided yields of CH_4 in the range of 1 – 3 wt%, conforming to experimental findings. The yields of the other gas components are irrelevant considering the extent of their yields.

Table 16: Comparison of Specific Gas Yields on Total Gas Basis

	HWS (wt% NF)		SFPC (wt% NF)	
Component	**Experimental Yield**	**Model Yield**	**Experimental Yield**	**Model Yield**
Carbon Dioxide	51.63	72.44	51.26	66.37
Hydrogen	0.16	0.22	0.35	1.45
Carbon Monoxide	42.40	21.85	44.71	32.18
Methane	3.35	0.00	1.21	0.00
Ethylene	1.19	5.50	0.93	0.00
Ethane	0.54	- NA -	0.30	- NA -
Propane	0.19	- NA -	- ND -	- NA -
Propylene	0.54	- NA -	- ND -	- NA -
Acetylene	0.00	- NA -	0.00	- NA -
Argon / Oxygen	0.00	- NA -	0.00	- NA -

- NF: Nitrogen-free, NA: Not applicable, ND: Not detected

The predicted yields of the liquid organic phase were also reviewed against the bio-oil analytical properties. Results are presented in Table 17. With regards to the moisture content, it is predicted very accurately with under a 1 wt% variation. The difference in water yields observed in Figure 26 is due to the fraction of pyrolytic lignin which was merged into the yield numbers. It is well known that a fraction of the bio-oil is composed of these large phenolic oligomers, and merging their respective yields into the results presented equivalent experimental and model C/H/O values. Slightly larger amounts of produced formic acid for the SFPC derived bio-oil also reflect the lower pH value. Though it is not presented in the mechanism, the conversion of hydroxy-acetaldehyde to lower pKa organic-derived acids commonly found in pyrolysis oils is also possible and therefore the larger amounts produced for the SFPC derived bio-oil could also reflect the lower pH value. Based on the specific yields, the C/H/O content on the bio-oils was compared in Figure 27. Overall, lower carbon content and higher oxygen content for both mechanism outputs were observed suggesting that the mechanism is dominated by smaller oxygenated compounds (acids/alcohols) and is lacking the inclusion of heavier organic molecules such as simple aromatics (BTX) and possibly slightly larger poly-aromatics (PAHs). Though, the formation of PAHs was thought to be unlikely at pyrolysis temperatures and residence times. Additionally, due to their higher the carbon to hydrogen ratio, benzene rings store more potential combustion energy per mole than other components. This is observed comparing the carbon content of both feedstock experimental bio-oil yields. As seen, the carbon content from the HWS mechanism yield is slightly higher than the SFPC yield, which is characteristic considering the larger measured higher heating value (HHV) of the HWS-derived

bio-oil. Finally, the lower viscosity of the HWS-derived oil is strongly linked to the higher water content.

Table 17: Bio-Oil Analytical Results

Properties	HWS derived Bio-Oil	SFPC derived Bio-Oil
Moisture Content	19.6 wt%	16.6 wt%
Viscosity (40°C)	21.22 cSt	44.39 cSt
pH	2.5	1.9
HHV	20.81 MJ/kg	17.26 MJ/kg

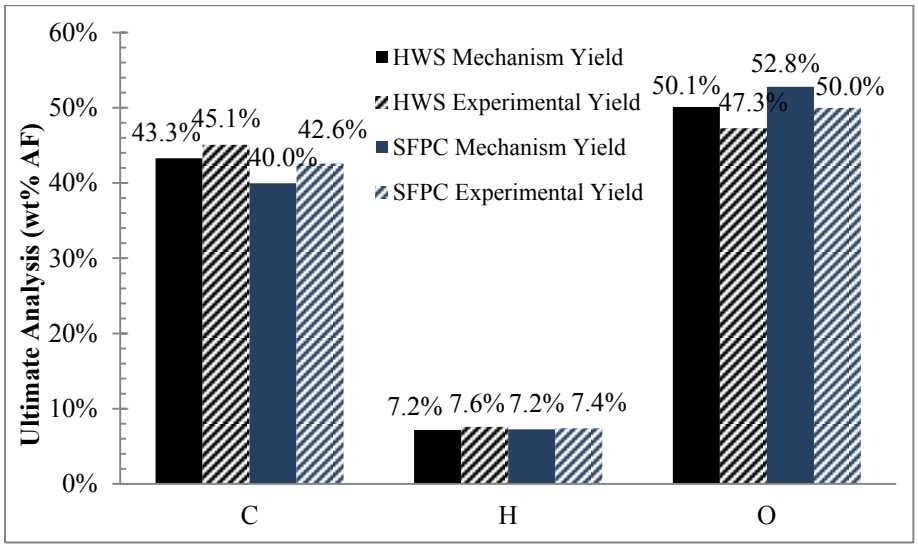

Figure 27: Comparison of C/H/O Elemental Yields

3.4.1.3. Effect of Operating Temperature

As the reactor temperature is increased, it is clear that the secondary tar cracking reactions are more prominent. Yet, as can be seen in Figure 28, they start to be even more noticeable at lower temperatures than was observed with the Miller and Bellan (1996) mechanism. The rates of gas production are larger for the ideal range of operational fast pyrolysis temperatures than those provided by the Miller and Bellan (1996) mechanism. However, at higher temperatures, the rate of gas production tends to plateau whereas it would be expected to increase dramatically and equivalently decrease the yield of bio-oil. Similar yield trends were reported by Blondeau et al. [98]. The yields of char have similarly been found to plateau as temperature increases, though at slightly higher yields than measured experimentally.

As previously discussed, this has been linked to the slow evolution of trapped components making up roughly 65 % of the char and dominated by the yield of trapped formaldehyde ($G\{COH_2\}$). The char yields for the HWS feed plateau at levels slightly higher than is observed experimentally whereas the yields for the SFPC plateau at similar levels suggesting that the hemicellulose and lignin char forming reactions need further calibration for higher heating rate pyrolysis.

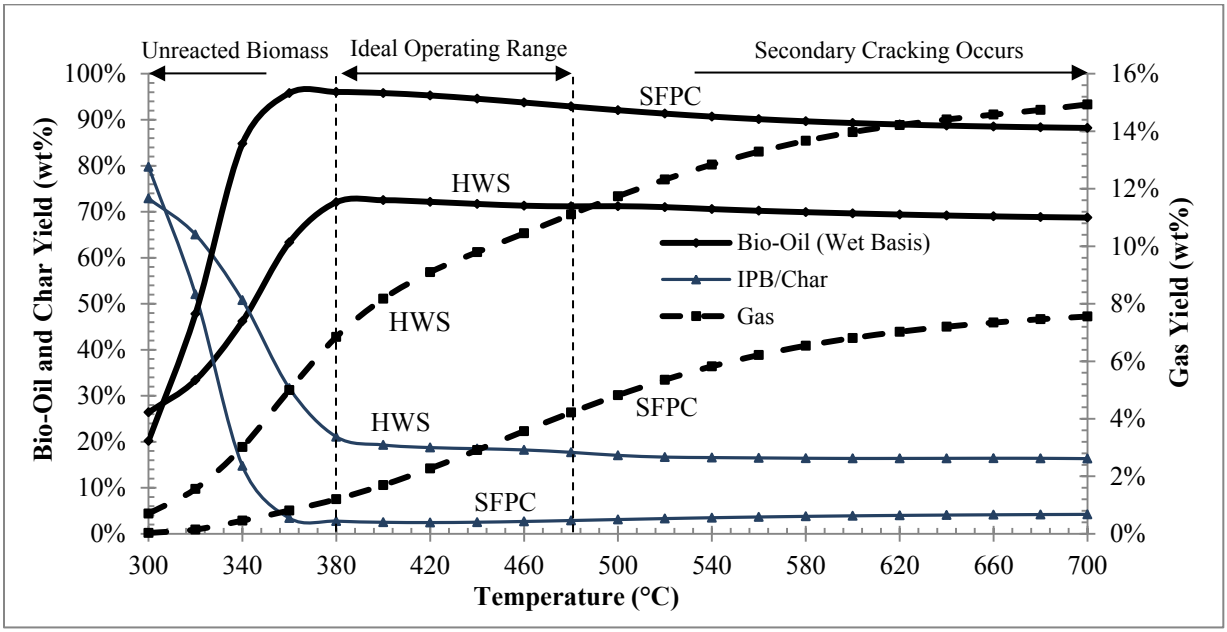

Figure 28: Effect of Temperature on Fast Pyrolysis Product Yields for HWS and SFPC; Data Generated using the Ranzi et al. (2014) Mechanism

3.4.2. Suggested Modifications of Multi-Component and Multi-Step Mechanisms

With the performance of the Miller and Bellan mechanism discussed in Section 3.4.1.1, no modifications were considered necessary. However, for the mechanism with product specification – the Ranzi mechanism, certain imperfections which led to its underperformance, such as the differences in bio-oil class yields and the plateau behaviour at higher temperatures, necessitated alterations. The work on Ranzi mechanism modifications in the literature is minimal. Only a few authors [84,98,99] have suggested modifications accounting for secondary reactions, alternate devolatilization pathways and the effect of inorganic mineral content. The following sections will assess the effect of secondary reactions on the yield plateau behaviour at

higher temperatures and suggest a simple kinetic parameter change to minimize differences in bio-oil class yields. Due to the low ash content of both the HWS and SFPC feedstocks, the mechanism modifications for the effect of inorganic mineral content were neglected.

3.4.2.1. Considering the Effect of Secondary Gas Cracking Reactions

To modify the behaviour of the Ranzi mechanism at temperatures beyond the optimal operating range, secondary gas-phase bio-oil cracking reactions were implemented based on the scheme presented in the work of Mellin et al. [85]. Results are presented in Figure 29.

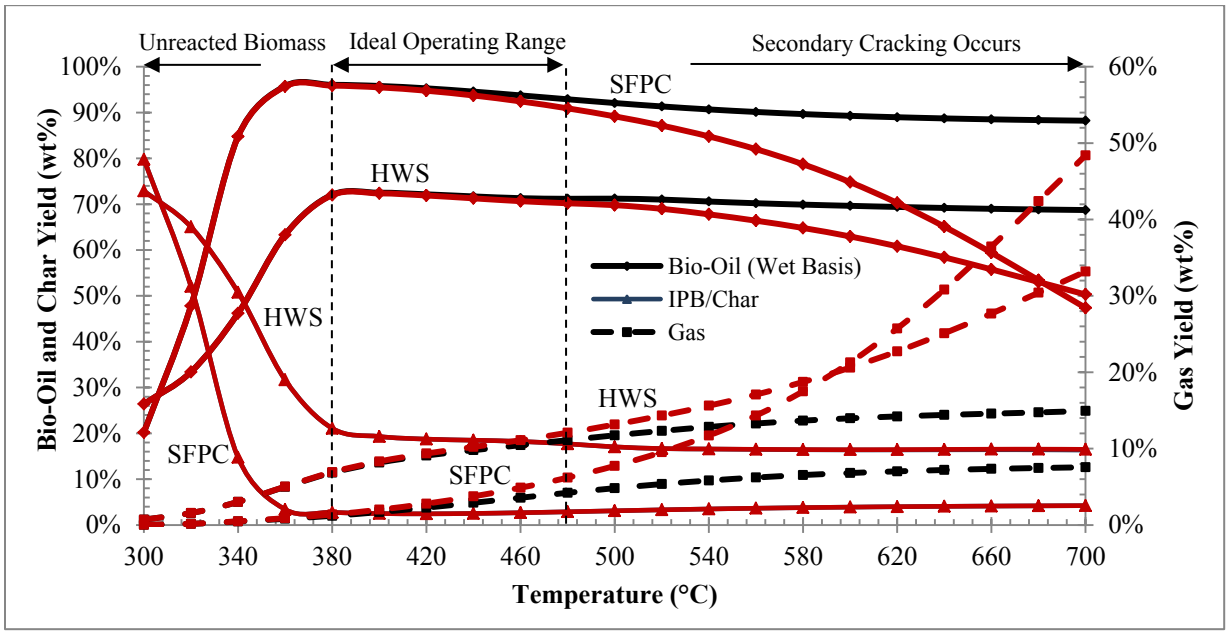

Figure 29: Effect of Temperature on Fast Pyrolysis Product Yields (Black: Original Mechanism, Red: Including Secondary Reactions)

Compared to what was observed in Figure 28, the yields in Figure 29 are unparalleled at temperatures beyond ideal operating range. The thermal cracking of pyrolysis vapours is far more prominent as the temperature is increased, mirroring the behavior observed with the Miller and Bellan mechanism; though not to the same extent. It should be noted that the rate of secondary cracking is larger for the SFPC-derived bio-oil suggesting that sugar fragmentation is a major contributor to increasing gas yields. As expected, there is no change on the yield of char.

3.4.2.2. Adjusting the Activation Energy for the Activated Cellulose Transglycosylation Reaction

As was displayed in Figure 26, the largest differences were found to be the overestimation of the sugar content and the underestimation of the acids/alcohols content. Levoglucosan is one of the major anhydro sugar products of fast pyrolysis and interestingly, the justification of its formation mechanisms from the devolatilization of cellulose has been subject to certain controversy. The analysis and formation of levoglucosan has been studied by several authors [100–105], among many, with the general consensus being that the theoretical activation energy for the formation of levoglucosan is approximately 200 kJ/mol. Though, the activation energy for the activated cellulose transglycosylation reaction presented in the Ranzi 2014 mechanism is much lower at 41.9 kJ/mol. Accordingly, the overestimation of the sugar content is believed to be linked to the transglycosylation reaction overwhelming the cellulose ring fragmentation reactions (much higher activation energy) and favoring the production of large quantities of levoglucosan. A study into the sensitivity of this activation energy was done and is presented in Figure 30.

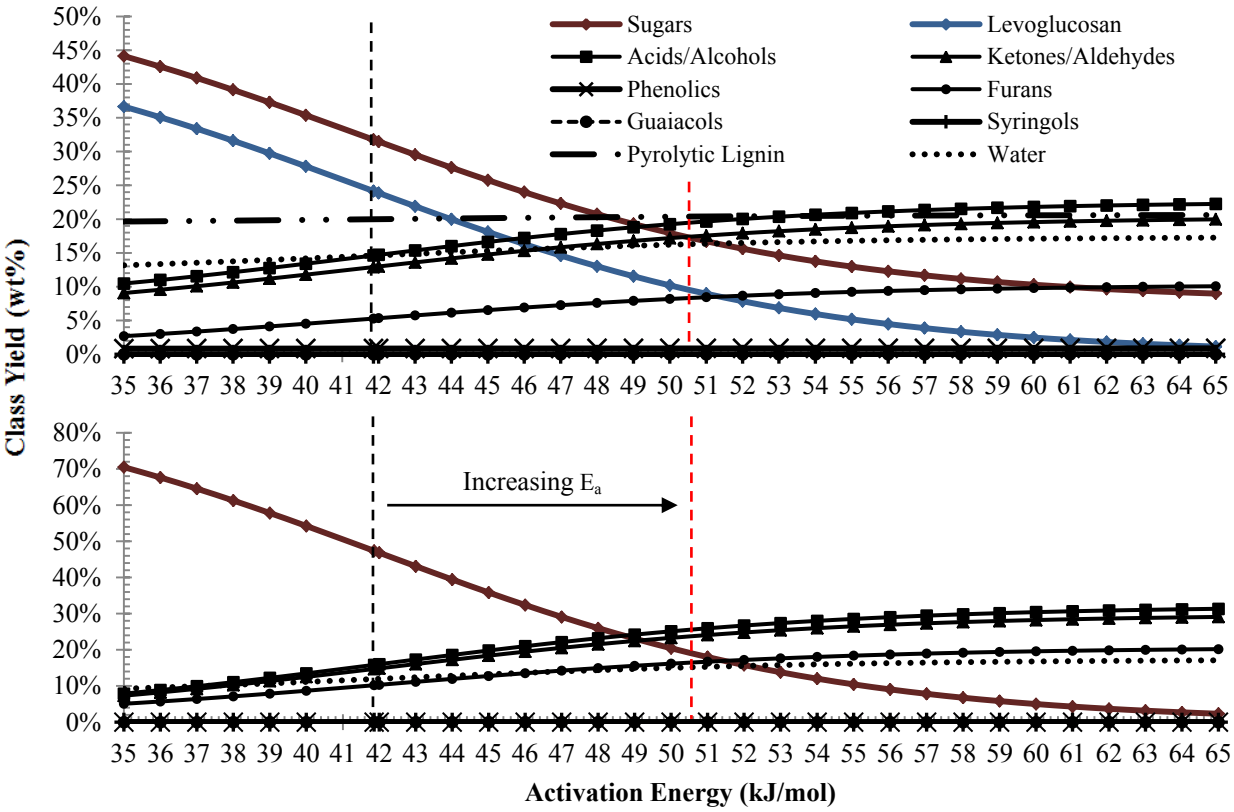

Figure 30: Sensitivity Analysis for Activated Cellulose Transglycosylation Reaction at 480 ºC (Top: HWS, Bottom: SFPC)

As the activation energy is increased, the rate of sugar formation decreases significantly. Specifically, the levoglucosan yield descends to minimal quantities at an activation energy of approximately 65 kJ/mol. Considering the sensitivity of the sugar product to change in activation energy, it was concluded that the suggested energy required for the production of levoglucosan was too low and a slight parameter change was recommended to minimize differences in bio-oil class yields. A value of $E_a \approx 50.5$ kJ/mol was used to mitigate the incongruities and new class yields are presented in Figure 31. As can be seen, the yield of total sugar is now relatively proportionate with what is detected experimentally. The difference observed with the HWS-derived bio-oil sugar content has been attributed to sugars resulting from the devolatilization of hemicellulose, such as xylose, which are not detected by the analysis method used. The yield of acids/alcohols, ketones/aldehydes and water were also balanced out, conforming slightly more to the proportions found in the experimental analysis. Granted, the predicted yield of furans, mostly formed in the devolatilization of highly cellulosic material, did fairly diverge from experimental

findings; suggesting that the loss of water-soluble phenols and furans is a possibility in the bio-oil analysis.

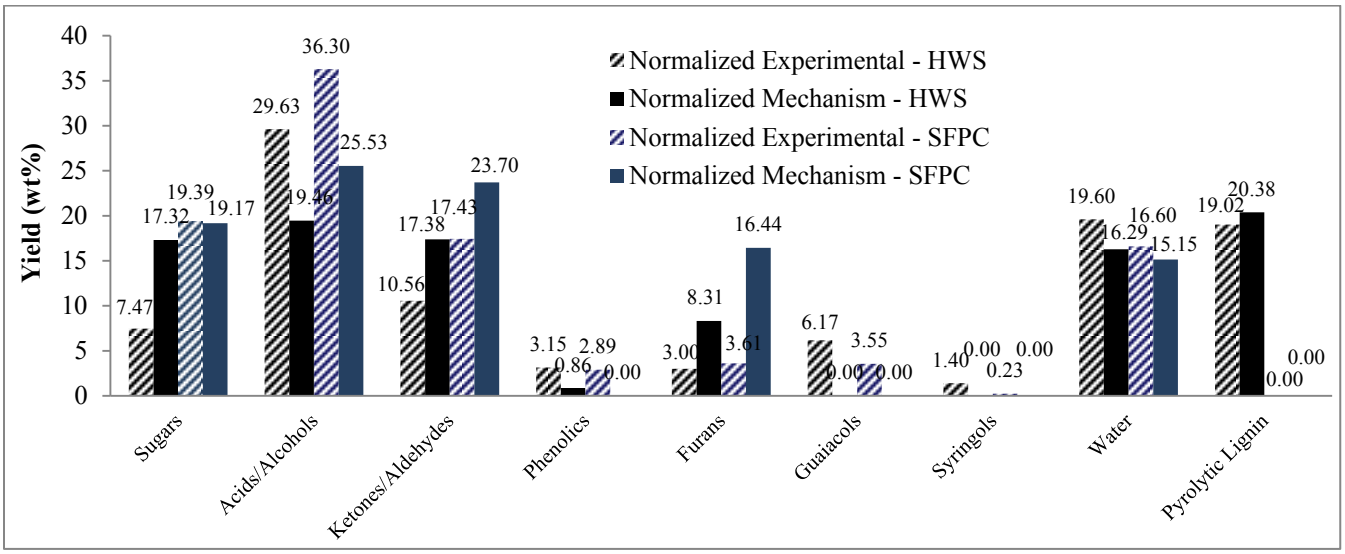

Figure 31: Comparison of Classified Specific Bio-Oil Yields after Modification

Considering the latter, it can be concluded that the activation energy for the transglycosylation reaction must be increased to allow for competing fragmentation reactions. The extent of the modification was small in this work; though, a fundamental and concrete understanding of the sugar formation mechanism is still required for further calibration. This could also include the hemicellulose-cellulose and lignin- cellulose interactions, which have been known to modify sugar behaviour and enhance the formation of lower molecular weight products [79].

3.5. Conclusions

Because of the quick nature of biomass fast pyrolysis, the performance of reactor models is greatly affected by the formulations of the devolatilization schemes. The current work has reviewed and tested the extensions of two existing multi-step and multi-component fast pyrolysis reaction mechanisms, with and without product specification, for different feedstocks and operating temperatures.

It was found that the Miller & Bellan (1996) mechanism tends to provide much closer results to those of experimental nature and that no major mechanism modification is required. Admittedly, the mechanism did not perform as well with the high ash containing feedstock nor

did it give any insight on product quality. Thus, integrating the effect of inorganic content as well as extending product specification to further characterize the bio-oil, such as including moisture content, is recommended.

While the Ranzi et al. (2014) mechanism provided similar yield trends, it tends to slightly underpredict the yield of bio-oil and overpredict the yield of char. In fact, for the SFPC-derived bio-oil, gas and biochar yields were slightly underpredicted suggesting that yield of gas and char resulting from the devolatilization of hemicellulose and lignin are too high.

Since the mechanism is formulated with respect to five lignocellulosic reference components instead of three, a comprehensive biochemical analysis of the feedstocks is required. While it may be difficult to get details on the specific the lignin based components, an approximation was obtained using the feedstock's preliminary biochemical analysis and the ultimate analysis.

Due to the complexity of accurately quantifying all the individual compounds in bio-oil, an experimental and mechanism component classification procedure was presented for mechanism assessment. The components were partitioned within common pyrolysis oil organic classes according to their functional groups. It was found that this arrangement of components represented relatively analogous based on an examination of the C/H/O mass content. Although GC-MS was used for characterization, there are certain downsides to using gas chromatography for bio-oil analysis, particularly concerning the thermal instability of compounds. Less thermally severe methods of characterization, such as HPLC, are recommended.

Adjustments to the Ranzi et al. (2014) mechanism were proposed which minimized the differences in component class outputs and increased the accuracy of model predictions. One of the main disadvantages of the reaction scheme was that it did not explicitly account for secondary tar cracking reactions. The scheme was extended to include additional steps accounting for secondary reactions which fixed the yield plateau behavior at higher operating temperatures. Due to relatively high predicted sugar yields, the cellulose devolatilization scheme was modified to limit the production of levoglucosan. A sensitivity analysis on the activation energy of the activated cellulose transglycosylation reaction revealed quite the large sensitivity of levoglucosan yield with change of the parameter. A value of 50.5 kJ/mol was suggested since it minimized component class yield differences.

The sensitivity of the model to kinetic parameters combined with the difficulties in bio-oil characterization makes fitting procedures even more challenging. In addition, the influence of the heating rate on the kinetic constants is only partially addressed and the need of compensation effects to account for different thermal conditions, such as those comparable with commercial scale systems, are required.

Considering, its simplicity over other multi-step and multi-component mechanisms and its ability to predict product composition, it is recommended that the Ranzi mechanism be considered in future fast pyrolysis modelling studies. As detailed, complete and reliable analytical evaluations of large-scale bio-oil samples become available, further modifications can be made with higher certainty.

Chapter 4: Effects of Fluidized Bed Hydrodynamic Formulations on the Performance of a Fast Pyrolysis Reactor Model

The current chapter is a manuscript prepared for refereed journal publication.

Johnny Matta[a], Benjamin Bronson[b], Peter E.G. Gogolek[b]
Jules Thibault[a], Poupak Mehrani[a]

[a]Department of Chemical and Biological Engineering, University of Ottawa
161 Louis Pasteur Street, Ottawa, ON, K1N 6N5, Canada

[b]Natural Resources Canada, CanmetENERGY
1 Haanel Drive, Ottawa, Ontario, K1A 1M1, Canada

Abstract

The effect of biomass fast pyrolysis devolatilization schemes on fluidized bed reactor model performance has been studied. It was concluded that the predicted reactor model yields are greatly affected by the reaction mechanism due to the quick nature of biomass fast pyrolysis. This work has for objective to determine if the performance of kinetic models is also dependent on the formulation of the hydrodynamic schemes in a fast pyrolysis fluidized bed reactor. In particular, the work explores the extent to which pyrolysis product yields vary with changes in multi-phase flow profiles in Grey-Box Models. The effects of fluidizing velocity and feedstock particle size on product yields are also investigated. Several works have been devoted to modelling fast pyrolysis at the bubbling fluidized-bed reactor level. These works utilize complex hydrodynamic models with simplified devolatilization mechanisms. Results generated from this research will help in determining whether or not complex hydrodynamic schemes are necessary for determining biomass fast pyrolysis product yields in a cost and time-effective fashion.

Keywords: Biomass Fast Pyrolysis, Reactor Modelling, Grey-Box Models, Fluidization, In-Bed Hydrodynamics

4.1. Introduction

Biomass fast pyrolysis is a promising technology for converting and upgrading carbonaceous feedstocks into a range of liquid fuels and other products. The process involves the thermal degradation of the biomass, in the absence of oxygen, at temperature ranging from 450 °C to 600 °C [42]. Rapid heating rates of the biomass and quenching rates of the organic vapours are necessary to ultimately produce a liquid product termed bio-oil or pyrolysis oil [14]. Bio-oil is a heterogeneous mixture, high in oxygen content, made up of different components such as sugars and anhydrosugars, carbonyls and hydroxycarbonyls, acids, phenols and pyrolytic lignins [12]. Non-condensable gases and biochar are also products of the thermal decomposition of biomass. The gas phase consists mainly of CO_2, CO, and CH_4, as well as traces of H_2 and C_2-C_3 compounds [11]. These by-products can be used in combustion practices to improve the efficiency of the energy required to recover bio-oil.

Fluidized beds are most commonly employed for thermochemical conversion processes to facilitate and meet the conditions required for good reactor performance. That is, allowing for higher heat and mass transfer rates as well as promoting solids mixing and increasing biomass particle residence times. Additionally, the flow of the fluidizing medium may be tuned to increase the gas carry-over velocity and reduce organic vapour residence time in the bed and diminish secondary bio-oil cracking reactions. The removal of lighter and porous char particles, which is required to minimize the available surface area for secondary cracking, is also facilitated by elutriation in fluidized beds. While fluidized beds are great units for conducting fast pyrolysis processes, the erratic nature of in-bed dynamics makes it difficult to establish a fundamental understanding of these mechanics. The current understanding and progress with fluidized bed hydrodynamic models have been classified into three types of models [25]. They are sorted into Black, Grey and White Box models according to the adopted fluid-dynamic simplifications. Transitioning from Black to Grey to White-box models increases the level of mechanistic insight into the behaviour of the fluidized bed. However, the required computational efforts and model input parameters also increase. A description of these types of models is presented in Chapter 1. A previous study developed a one-dimensional fluidized bed Grey-Box model and implemented different biomass devolatilization schemes, not only for biomass fast pyrolysis product quantity but also liquid product composition (quality), to examine the effect of

variable reaction kinetic sub-models on product yields. The model predictions validated well with results generated from the experimental work. The goal of this work is to review and test the performance of different hydrodynamic sub-models for fast pyrolysis fluidized bed reactors to establish if there exists a dependency of model predictions on the formulation of the hydrodynamic schemes. The objective is to investigate the effect of the dominant independent model variables such as the fluidizing velocity and the feedstock particle size on measurable outputs such as product (bio-oil, gas and biochar) yields and compare the outputs to experimental results generated from a pilot-scale fluidized bed fast pyrolysis unit.

4.2. Reactor Model Development

The reactor models used in this study were developed at the University of Ottawa using the Microsoft Visual Basic for Applications (VBA) software. The results are compared to the experimental data generated from the Bell's Corners Complex (BCC) pilot-scale fluidized bed fast pyrolysis unit located at NRCan CanmetENERGY (Ottawa, ON). Details concerning reactor parameters and general operating conditions are presented in Figure 32. The models have been classified as Grey-Box Model #1 (hereinafter referred to as GBM1) and Grey-Box Model #2 (hereinafter referred to as GBM2), the latter incorporating a modified hydrodynamic sub-model of the first one.

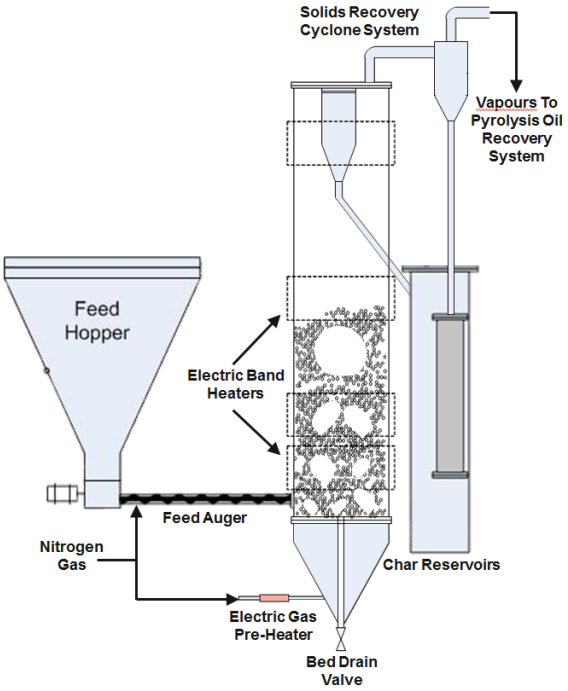

Operating Fluidization Regime	Bubbling
Reactor Internal Diameter	0.1 m
Reactor Height	1.0 m
Operating Pressure	Atmospheric
Operating Temperature	400-550 °C
Typical Fluidizing gas flow	~0.0025 SCMPS
Average Fuel Capacity	5.4-6.5 kg/h
Average Fuel Usage per Run	25 kg
Nominal Feed Particle Size	0 - 5 mm
Fluidizing Medium	Nitrogen
Bed Material Type	32-B4 Olivine Sand
Bed Material Size	~600 µm
Bed Material Mass	~3.75 kg
Bed Particle Density	2830 kg/m^3
Bed Bulk Density	1515 kg/m^3

Figure 32: Fast Pyrolysis Fluidized Bed Reactor Parameters and General Operating Conditions (reactor located at NRCan CanmetENERGY)

The objective of the GBMs is to provide individual component concentrations and overall yields of the pyrolysis products by solving a set of component mass and heat balances over a pre-defined grid. The advantages of GBMs are that they are easier to implement, there are few inputs required and model runtime is relatively fast. For both GBM1 and GBM2, the devolatilization of the biomass is based on the multi-component reaction mechanism of Miller & Bellan (1996) [80]. This mechanism takes into account the thermal dynamics of the components corresponding to woody biomass: cellulose, hemicellulose and lignin. The evaporation of biomass moisture has been added according to the works of Sreekanth et al. [40].

4.2.1. Grey-Box Model #1

GBM1 is a transient, non-isothermal, one-dimensional fluidized bed model with a simplified multiphase flow pattern for the dense bed. The modelling approach was to divide the bed height into discrete volumes, with different fractions representing three phases: biomass, sand, and gas. Each phase is perfectly mixed, has its own temperature, volume and velocity, and is affected by the other phases only through the devolatilization of biomass and the transfer of

energy. In the biomass phase, the particles are perfect spheres and follow a uniform conversion pathway (UCM). That is, conversion takes place equivalently throughout the non-shrinking particle and is linked to a change in particle density. In other words, the incoming biomass is converted into char, while maintaining the same volume. The ash content is considered to remain impregnated within the particle. The volatile fraction of the biomass reacts and is transferred into the gas phase. The velocity change is linked to the change biomass volume fraction with height, to maintain a constant volumetric flow of particles through the bed. In the gas phase, the fluidizing nitrogen gas enters at the bottom of the bed and leaves the top carrying volatile products such as organic vapours, non-condensable gases and evaporated water. The sand phase is stationary across each discrete volume of the bed and does not affect the interphase mass transfer. A visual representation of the phases is shown in Figure 33.

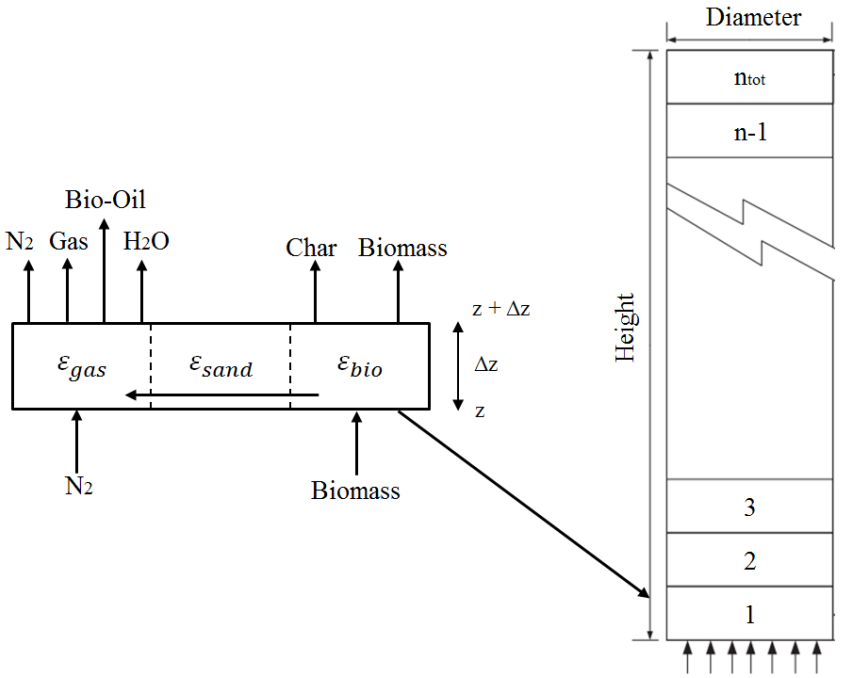

Figure 33: Inputs and Outputs of Discrete Volume (Cell) in GBM Grid

The set of hydrodynamic equations to calculate the volume fractions of the phases are determined with Equations (1) through (10) [18,43,45,106–108]. An estimate of the biomass fraction is based on the differential pressure change of the fluidized bed when biomass is introduced into the bed (Equation (9)).

$$Re_i = \frac{d_i U_g \rho_g}{\mu_g} \tag{1}$$

$$C_D = \frac{24}{Re}\left[1 + \left(8.1716e^{-4.0655\phi}\right)Re^{0.0964+0.5565\phi}\right] + \frac{73.69Re\left(e^{-5.0748\phi}\right)}{Re + 5.378e^{6.2122\phi}} \quad (2)$$

$$U_t = \sqrt{\frac{4d_s(\rho_s - \rho_g)g}{3\rho_g C_D}} \quad (3)$$

$$U_{tc} = 10^{\left(\frac{\log U_t}{\log 10} - \frac{d_s}{D_r}\right)} \quad (4)$$

$$n = 4.4 + 18\left(\frac{d_s}{D_r}\right)Re^{-0.1} \quad (5)$$

$$\varepsilon_{mf} = \left(\frac{U_g}{U_{tc}}\right)^{\frac{1}{n}} \quad (6)$$

$$H_{mf} = H\left(\frac{1-\varepsilon}{1-\varepsilon_{mf}}\right) \quad (7)$$

$$\varepsilon_s = 1 - \varepsilon_{mf} \quad (8)$$

$$\varepsilon_b = \frac{\Delta(\Delta P_{bed})}{gH_{mf}\rho_b} \quad (9)$$

$$\varepsilon_{gas} = 1 - \varepsilon_b - \varepsilon_s \quad (10)$$

The relationships used to determine the volume fraction of each phase in the bed have a direct impact on velocity of the phases. The interstitial velocities of the gas and biomass phases are calculated using Equations (11) and (12), respectively. The sand phase in the reactor is assumed to have a net velocity of zero. Allowing for simple hydrodynamic relationships in the model reduces the complexity and computation time for GBM1. However, as with most Grey-Box models, this comes at the expense of possible fluid dynamic imprecisions of what may be occurring in reality.

$$U_g = \frac{U}{\varepsilon_{gas}} \quad (11)$$

$$U_i = \frac{\dot{m}_{bio}}{\rho_b \varepsilon_b A_C} \tag{12}$$

Each phase of the reactor exchanges energy with one another through heat transfer mechanisms including conduction, convection and radiation. Since convection is the predominant heat transfer mechanism of heat transfer in gas-solid fluid beds [109], particle-particle conduction is assumed to be negligible compared to the radiative and convective heat transfer [18]. Moreover, with a particle Biot number that is much smaller than 1 (< 0.2), the intra-particle heat transfer resistance is very low and a "thermally thin" particle assumption is valid. This signifies that the particle behaves isothermally. The scheme for heat exchange between the phases is shown in Figure 34. The biomass phase gains energy from the sand and gas phases through radiation and convection, respectively. The gas phase gains energy from the sand only by convective flow since the radiative heat transfer to and from the gas phase is small; resulting from the low thermal emissivity of gases. To maintain a constant bed temperature, heat transfer from the band heaters to the sand phase were modelled as a direct energy source (represented by Q), neglecting the conductivity through the reactor walls and the radiation from the walls to the sand particles.

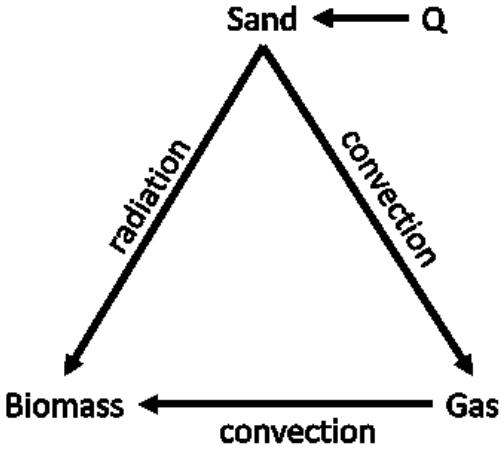

Figure 34: Prominent Heat transfer Scheme Between Phases

To determine the convective heat transfer coefficient (h_p) between the phases, the heat transfer correlation of Ranz-Marshall for heat transfer around spherical particles is used. The heat transfer coefficient, embedded in the Nusselt number, is a function of the particle Reynolds and gas Prandtl numbers. The correlation is shown in Equations (14). The first term of the

correlation represents the contribution of particle-fluid natural convection while the second term is related to the forced convection due to gas flow. The parameter *b* is taken to be 0.5 and the parameter *a* can range from 0.6 to 1.8, following the suggestions of Kunii and Levenspiel [106]. The upper bound of 1.8 was used for this work.

$$Nu_p = \frac{h_p d_p}{k_g} \tag{13}$$

$$Nu_p = 2.0 + aRe_i^b Pr^{1/3} \ (a = 0.5, 0.6 \leq b \leq 1.8) \tag{14}$$

$$Pr_g = \frac{Cp_g \mu_g}{k_g} \tag{15}$$

Heat transfer by radiation is given by the Stefan-Boltzman equation for radiant exchange between the sand and the biomass (Equation (16)). The effective emissivity between the two phases is determined by treating each phase as two opposing parallel surfaces with their own respective emissivity. This overall emissivity is shown in Equation (17).

$$h_r = e_{sb}\sigma(T_{sand}^4 - T_{bio}^4) \tag{16}$$

$$e_{sb} = \frac{1}{\frac{1}{e_s} + \frac{1}{e_b} - 1} \tag{17}$$

A few of the underlying assumptions of GBM1 include:

- Wood particles are perfectly spherical and are not susceptible to attrition
- Uniform distribution of volume fractions
- Isobaric operation and no significant effects of in-bed hydrodynamics or freeboard
- Non-reactive effect of water and ash species
- Negligible internal mass and heat transfer resistances

4.2.2. Grey-Box Model #2

The objective of GBM2 was to modify the previously developed GBM1 to better describe the fluidized bed hydrodynamic behavior. The previous model structure, which used a sequential modular approach to calculate component concentrations, was used but different hydrodynamic correlations linked to experimental observations were used to estimate the local volume fractions. For the most part, the balance equations remained unchanged. They were slightly modified to account for the interphase mass transfer and the variation in phase velocity across the cells. While it is desired to solve steady-state equations to avoid the time-consuming process of the transient concentrations reaching steady-state, it was essential to simulate the hydrodynamics with time to obtain a space-time average of the volume fractions. The goal is to minimize model runtime by estimating the required parameters based on few seconds of transient operation. The pre-determined grid used for solving the set of component mass balances is used for the transient-mode estimations.

Many efforts have been made to modelling the multi-phase flow and estimating fluidization parameters in different fluidization regimes. Generally, the gas is dispersed between two phases, the bubble and emulsion [45], though some works have also incorporated a third phase (cloud-wake). There is no major fundamental difference between models but simply different correlations for phase properties such as bubble size, velocity and volumetric fractions. There exist many variations of GBMs, and some of the more popular ones include: the Kunii and Levenspiel Model [46], the Davidson-Harrison Model [47] and the Kato and Wen Model [48]. The most common assumptions are that solids are considered perfectly mixed in the bed and that the gas, in the bubbles and emulsion, follows plug flow behavior. Although sometimes the latter is taken as perfectly mixed, especially at high fluidization velocity [25]. Bubbles are also commonly stated to be solids-free. In addition, there exist some assumptions and simplifications, particularly related to the coalescence of bubbles within the bed. For instance, it is generally assumed that gas beyond the minimum fluidizing velocity forms a single train of bubbles rising along the center line of the bed [45]. At larger fluidizing velocities and higher bed heights, complete jet interaction at the distributor plate is generally observed and bubbles coalesce violently, almost instantaneously, to form practically cloudless bubbles [46].

The largest difficulty in modelling in-bed hydrodynamics arises when the operating fluidizing velocity changes significantly, causing the fluidization regime to transition from one to another. For Geldart group B particles, this increase in fluidizing gas volumetric flow rate along with the large aspect ratio of pilot scale reactors is regularly met by the transition from bubbling to slugging phase. In the slugging flow regime, bubbles reach large diameters (larger than 2/3 of the bed diameter) and the bed surface rises and falls with regular frequency and corresponding pressure fluctuations [45]. This was observed experimentally with a cold set-up at the University of Ottawa using a Plexiglas column with the same dimensions and operating with the same bed material and fluidization velocity as used in the fast pyrolysis reactor at NRCan CanmetENERGY (Figure 35). While it cannot be explicitly seen in the figure, the slugs were found to be round-nose slugs, occasionally moving along the wall and forming flat-nose slugs.

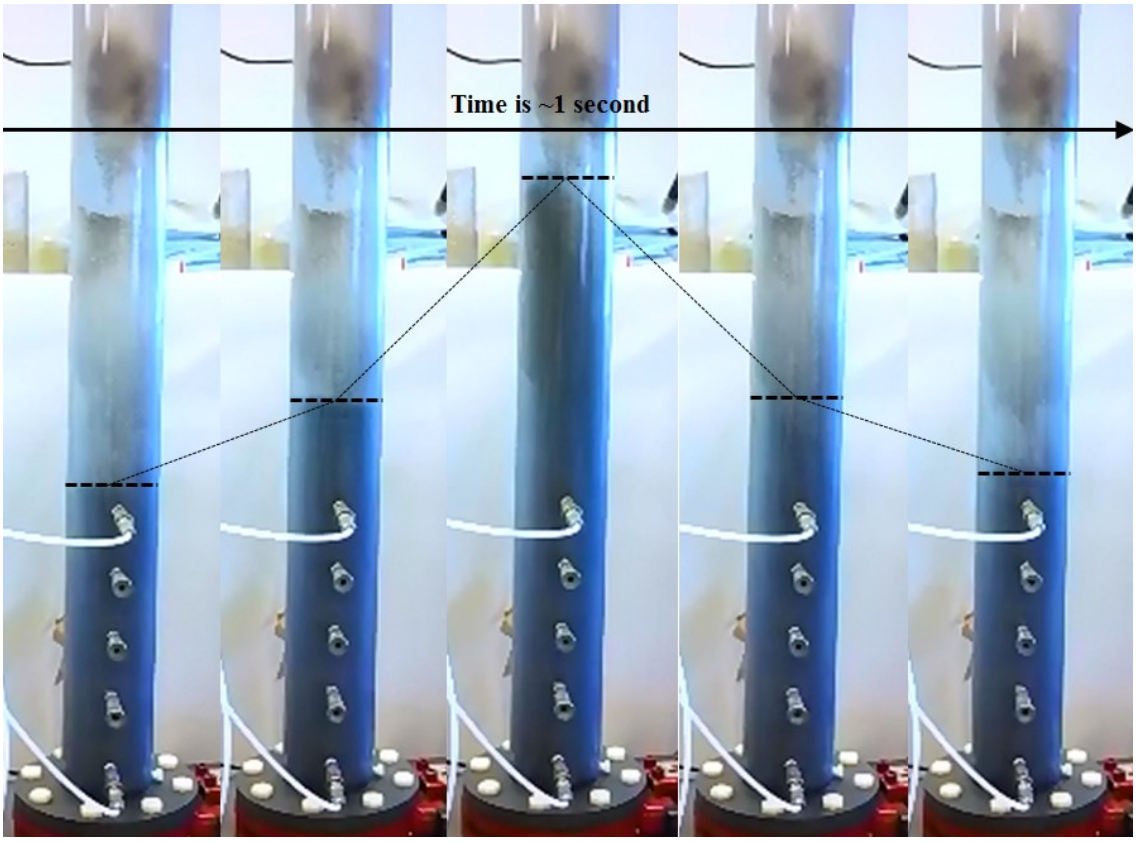

Figure 35: Slugging Behavior of Fluidized Bed at Fast Pyrolysis Fluidizing Velocity

One important aspect of bubbling fluidized beds is that most of the gas in excess of that required for minimum fluidization will form bubbles which propagate through the bed with a

characteristic size and velocity - respective of the gas flow. Prediction of the bubble size, rise velocity and coalescence pattern are often difficult to estimate due their irregular geometry. A significant amount of work has been published investigating the behavior of rising bubbles and many empirical equations are available (Figure 36). However, it can be seen that there are limitations to the use of these correlations, especially at higher fluidization velocities. In the case of bubbling fluidized beds for fast pyrolysis, the gas residence time is required to be low ($\leq$ 1 s) to avoid undesired bio-oil compounds secondary reactions. This is problematic since the velocities are beyond the appropriate range suggested for the correlations. Many of the correlations also restrict the range of particle size, particle density, and column diameter, which complicate the selection of a suitable set of hydrodynamic equations. Additionally, equations for bubble volume fraction throughout the dense bed [46] were found to be unsuitable as they highly overestimate the fractions at these high fluidization velocities.

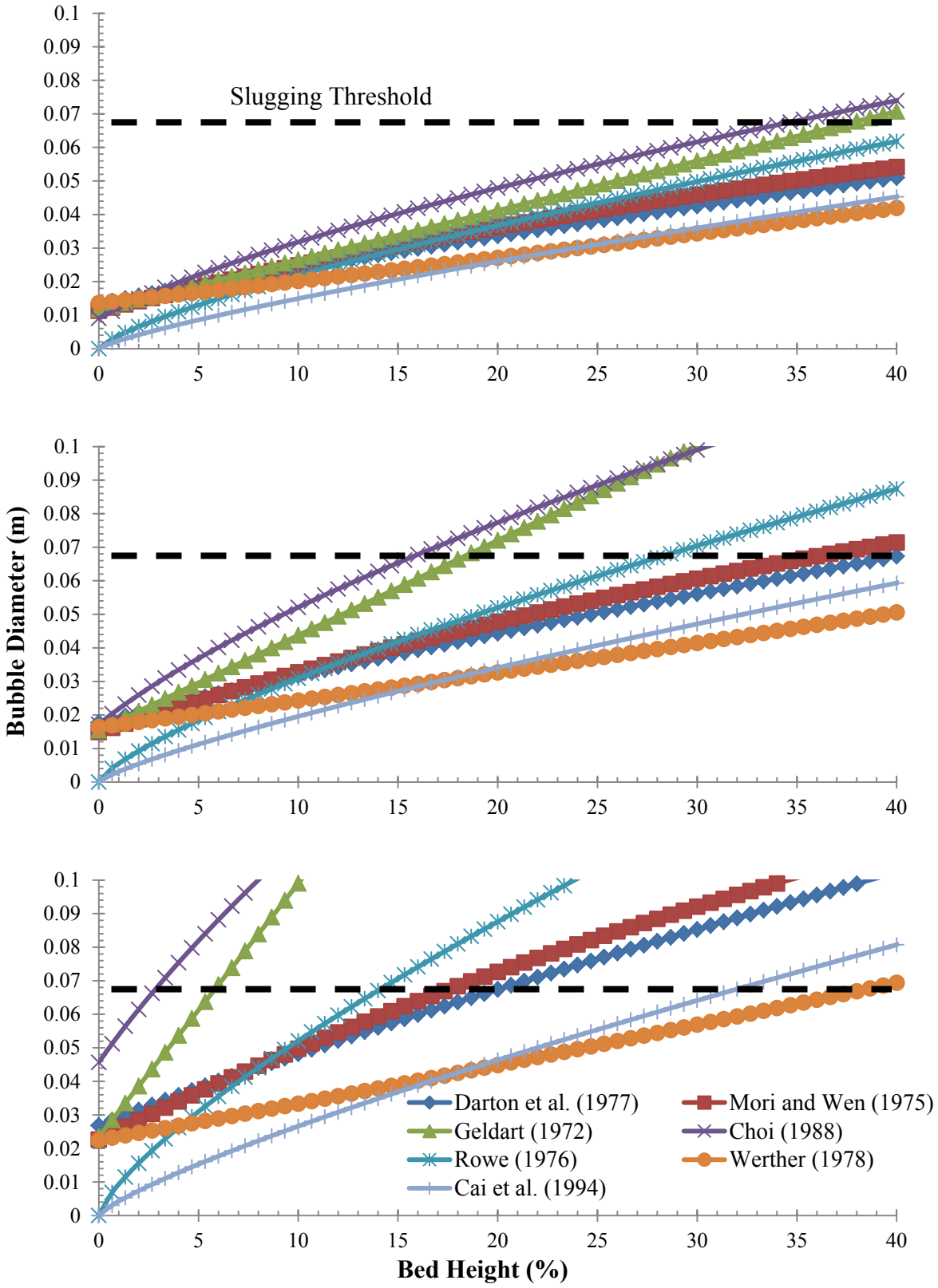

Figure 36: Behavior of Several Bubble Diameter Correlations when Increasing Fluidization Velocity (Top: $1.5U_{mf}$, Middle: $2U_{mf}$, Bottom: $3.8U_{mf}$) [110–115]

A different approach was taken in this work to calculate the volume fractions within the bed. This involves mechanistically taking the volume fraction of rising bubbles and time-averaging the fractions over a span of time which is deemed for steady state to have been reached. Figure 37 illustrates the mechanistic approach using sectional fractions of the bubbles and column to calculate the local volume fractions. Once the bed height is estimated, the cell volume (S_2) is determined according to the number of control volumes desired. As bubbles are formed and rise through the bed, the occupied bubble volume (S_1) within that cell is calculated and the bubble volume fraction (ε_b) for that cell is determined. The equations for the emulsion and solids volume fractions can be derived from the volume fraction of the bubble. Bubble fractions rise as the bubble diameter increases and plateaus when the maximum bubble size is attained. Since the volume fractions are time-averaged values, they are dependent on bubble forming frequency. While formation frequency is a parameter which has yet to be accurately quantified, it was assumed to have a value of 10 s^{-1}, following experimental observations in literature [114]. When the slug reached the top of the bed, it pops, which leads to a sharp decline in bubble fraction at the top of the bed. Further considerations are required on bubble behavior in the splash zone as particle velocities flow patterns are expected to be quite spontaneous in this section of the bed. Though, this was not examined. One advantage of operating at high velocities is that gas convection is magnitudes faster than diffusion, which yields a Peclet number much larger than 1. The axial diffusion of gas is therefore not worth considering, with respect to the undesired increase in numerical complexity.

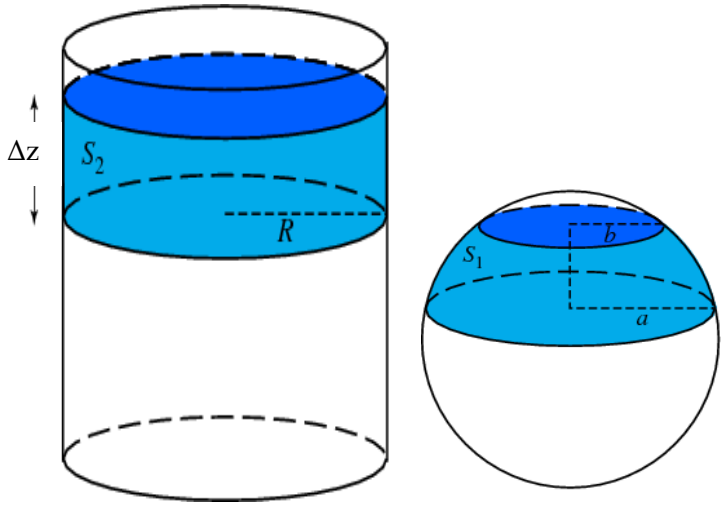

Figure 37: Schematic of local volume fraction calculations (adapted from [116])

The fraction of biomass particles within the bulk solids flow, be it virgin biomass, partially reacted biomass or char, is assumed to be well-mixed. Under the well-mixed assumption, it is important to study the axial movement of sand particles when looking to model the dynamics of biomass particles. The rise of bubbles through the dense bed induces the upflow of particles along the core of the bed, whereas the downflow is naturally found along the walls. The upwards movement of solids in fluidized beds is primarily due to two cavities created by the passage of bubbles: bubble wake and bubble drift. Equations for the transport of solids according to the bubble properties have been suggested. A particle rise velocity of 0.05 m/s was chosen following approximations from literature for flotsam particles [85,117,118]. An issue in deciding on the modelling approach for flotsam particles in fluidized bed is whether or not the particles keep floating once they have reached the bed's surface or if they are forced to descend or back mix with the bulk particles [25]. However, the latter was found not to be relevant in fast pyrolysis due to the very large reaction rates resulting in Damköhler numbers larger than unity. This signifies that the biomass particles tend to be fully (or nearly fully) devolatilized when they reach the top of the bed. Whether or not the particles descend, float or elutriate does not play an important role [25], unless char-catalyzed secondary cracking reactions are modelled. Additionally, it has been observed experimentally that the jet force from escaping volatile matter tends to keep the biomass particles floating at the top of the bed [119,120]. Since the particle density decreases significantly during devolatilization, complete elutriation was assumed following conversion. Figure 38 presents a schematic of the modelling approach taken for the multi-phase flows within the fluidized bed and the hydrodynamic parameters were calculated using equations (18) through (31) [121,122,110,123].

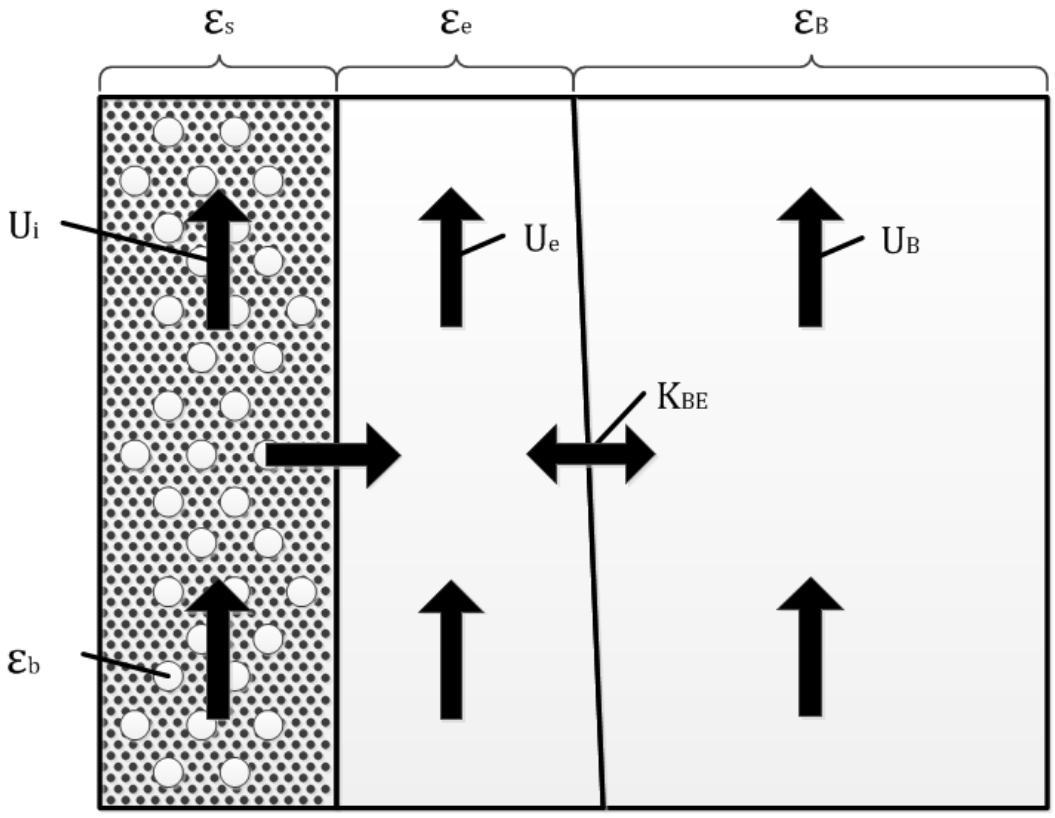

Figure 38: Schematic of Volume Fractions for GBM2 Phases

$$\varepsilon_B = \frac{\widehat{S_1}}{S_2} \tag{18}$$

$$\varepsilon_e = (1 - \varepsilon_B - \varepsilon_b)\varepsilon_{mf} \tag{19}$$

$$\varepsilon_s = (1 - \varepsilon_B - \varepsilon_b)(1 - \varepsilon_{mf}) \tag{20}$$

$$\varepsilon_b = \frac{\dot{m}_{bio}}{\rho_b U_i A_c} \tag{21}$$

$$K_{BE} = \frac{U_{mf}}{4} + \sqrt{\frac{4\varepsilon_{mf} D U_B}{\pi d_B}} \tag{22}$$

$$Ar = \frac{\rho_g(\rho_p - \rho_g)d_s^3 g}{\mu_g^2} \tag{23}$$

$$U_{mf} = \frac{\mu_g(\sqrt{27.2^2 + 0.0408Ar} - 27.2)}{d_s \rho_g} \tag{24}$$

$$\varepsilon_{mf} = \frac{0.496}{Ar^{0.029}\varphi^{0.72}} \tag{25}$$

$$U_i = \gamma U_B \tag{26}$$

$$U_e = \frac{U_g - \varepsilon_B(U_g - U_{mf})}{\varepsilon_e} \tag{27}$$

$$V_b = \frac{\rho_b}{\rho_b^i} V_b^i \tag{28}$$

$$d_B = 0.54(U - U_{mf})^{0.4}(h + 4\sqrt{A_0})^{0.8} g^{-0.2} \tag{29}$$

$$U_B = U_g - U_{mf} + U_{br} \tag{30}$$

$$U_{br} = \left(0.711\sqrt{g d_B}\right) 1.2 e^{\frac{-1.49 d_B}{D_r}} \tag{31}$$

Additional underlying assumptions of GBM2 include:

- Wood particles are perfectly spherical and are not susceptible to attrition
- Shrinking Unreacted Core Model (SUCM)
- Isobaric operation and no significant effects of in-bed hydrodynamics or freeboard
- Non-reactive effect of water and ash species
- Negligible internal mass and heat transfer resistances
- Bubbles are perfectly spherical and solids-free
- Ideal gas law for gas flow

4.3. Results and Discussion

To compare the effect of the different hydrodynamic profiles between GBM1 and GBM2, the simulations were conducted at a temperature of 480 °C, atmospheric pressure and a biomass feed rate of 6.5 kg/h. The feedstock used was maple-derived hardwood sawdust with a relatively low ash and moisture content. The biomass properties are presented in Table 18.

Table 18: Hardwood Sawdust Feedstock Properties

Feedstock Properties	
Mean Particle Diameter	~1 mm
Particle Density	~500 kg/m³
Proximate Analysis	
Moisture Content	7.27 wt%
Ash Content	0.36 wt%
Volatiles Content	79.04 wt%
Fixed Carbon Content	13.33 wt%
Biochemical Analysis	
Cellulose Composition	40 wt%
Hemicellulose Composition	38 wt%
Lignin Composition	22 wt%

4.3.1. Comparing the Effect of Biomass Particle Size on Product Yields

The effect of biomass particle diameter on the yield of bio-oil, gas and char is shown in Figure 39 for both GBM1 and GBM2. A range of sizes were examined from sawdust-like (<2000 μm) particles to pellet-like (~5000 μm) particles. The yields are taken at the top of the dense bed when the particles have undergone a single pass. As the particle size is increased, less energy can be transferred to particles for a given residence time. The slower rate of particle heating leads to a decrease in bio-oil yield and an increase in char and incompletely pyrolyzed biomass yields. This is evident with GBM2. In fact, the yields from GBM1 and GBM2 are in relatively good agreement until around 2500 μm where the yield of incompletely pyrolyzed biomass increases (yield of incompletely pyrolyzed biomass for GBM1 remains ~0 %). As a result, a difference in bio-oil yield is also observed beyond this point. Once the incompletely pyrolyzed particles reach the surface of the bed, the lack of good heat transfer on the top of the bed would induce a larger char-forming potential. Additionally, almost the entire fraction of incompletely pyrolyzed biomass is lignin-based polymers which, when slowly devolatilized, will predominantly yield char. The yield of gas remains unchanged as biomass size varies since the size does not significantly affect its temperature and velocity. While an extrapolation of the data at lower particle sizes would suggest an increase in bio-oil yields, reducing the particle size far beyond 600 μm could facilitate the blow-out of particles from the bed before being completely converted, as suggested by Xiong et al. [43]. This would result in a decrease of bio-oil yields.

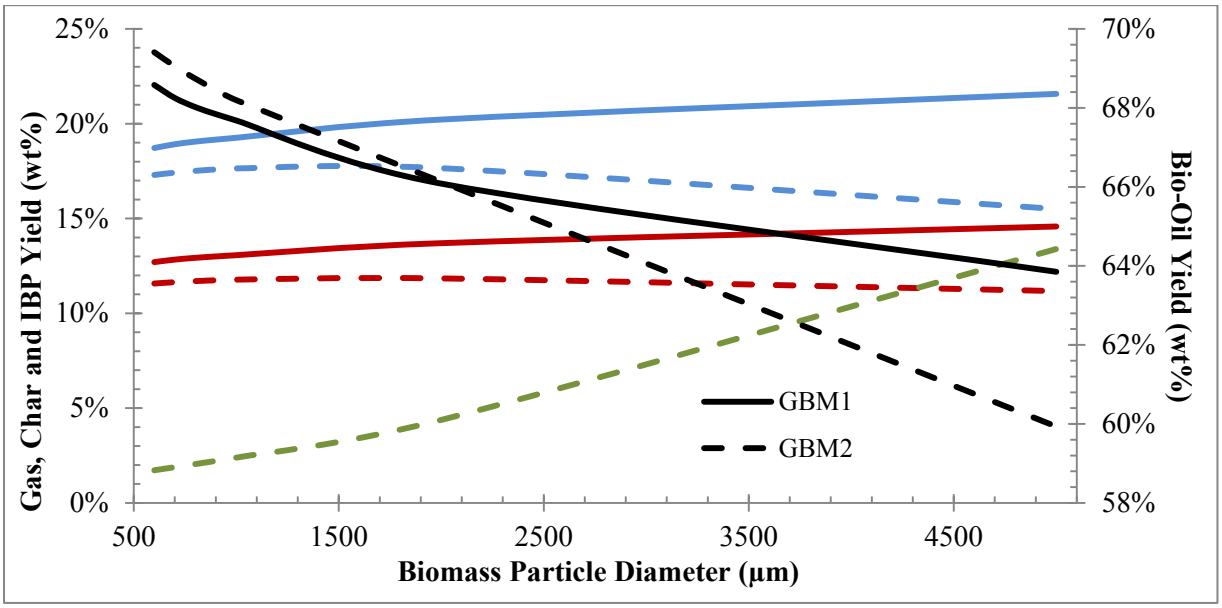

Figure 39: Effect of Biomass Particle Size on Product Yields (Black: Bio-Oil, Red: Gas, Blue: Char, Green: Incompletely Pyrolyzed Biomass (IPB))

The temperature profiles of the biomass and gas phase along the bed height is presented in Figure 40, Figure 41, Figure 42 and Figure 43. For both GBM1 and GBM2, the increase in biomass particle size necessitates a prolonged residence time to reach temperatures ideal for complete devolatilization. For GBM1, the slower velocity of biomass through the bed allows for rapid heating within minimal distance from the feed port. For GBM2, the higher modelled particle velocity leads to slower particle heating and the biomass reaches the ideal temperature further along the bed height. When decreasing the diameter of the biomass particle, the Nusselt number decreases which congruently decreases the convective heat transfer coefficient. However, the decrease in particle size also leads to an increase in the surface area to volume ratio. The net heat flux is found to be larger which leads to a faster decrease in gas temperature at lower biomass particle size. The phenomena discussed above for the biomass and gas temperature profiles are observed within both GBM1 and GBM2. Overall, the heating rate observed in GBM2 is lower than the one observed with GBM1, due to the faster moving particles. This is particularly evident for larger particles. The temperature rate of change for biomass and gas varies much more in GBM2. This is due to the change in particle diameter, the change in multi-phase volume fractions and the occurrence of exothermic gas-phase reactions within the phases. For example, with the rapid change in diameter of the SUCM, the heating

rates increase at approximately 8 % for particle below 1000 μm and approximately 12 % and 22 % for 2000 μm and 5000 μm, respectively. The heating rates slow down thereafter when the core has stopped shrinking. Although a decrease in bio-oil yields was observed with an increase in biomass particle size, the extent of the decrease is expected to be larger considering the increase of intra-particle heat transfer resistances for larger biomass particles.

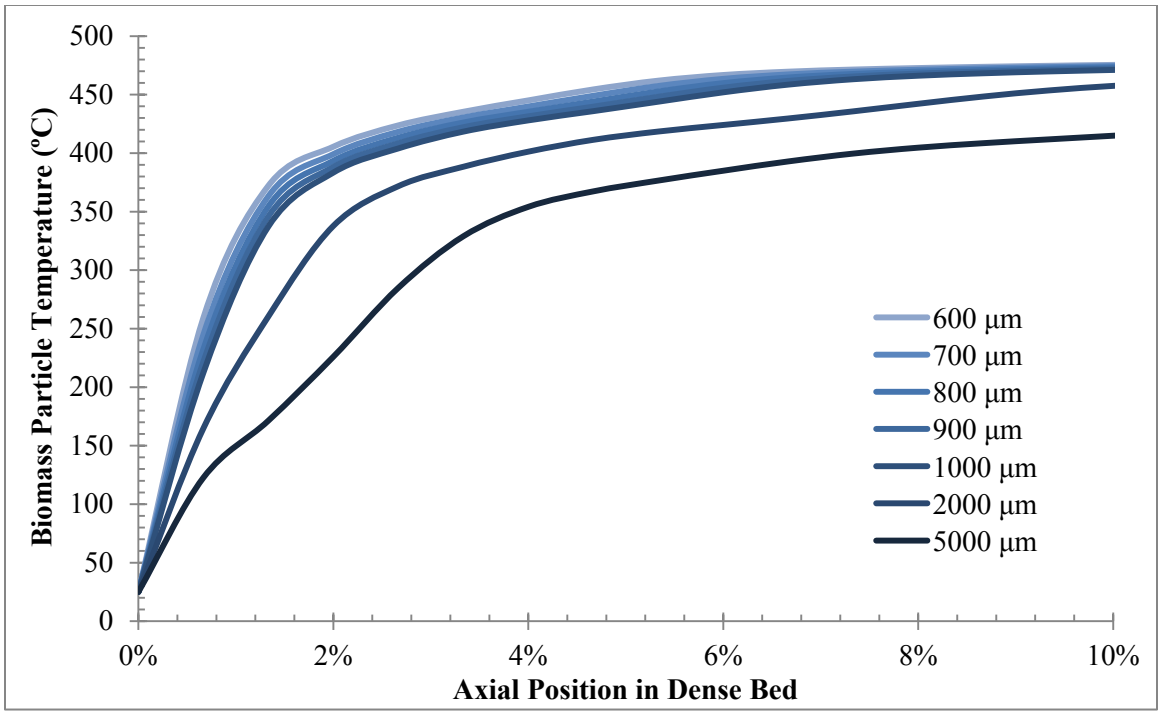

Figure 40: Biomass Temperature Profile with GBM1

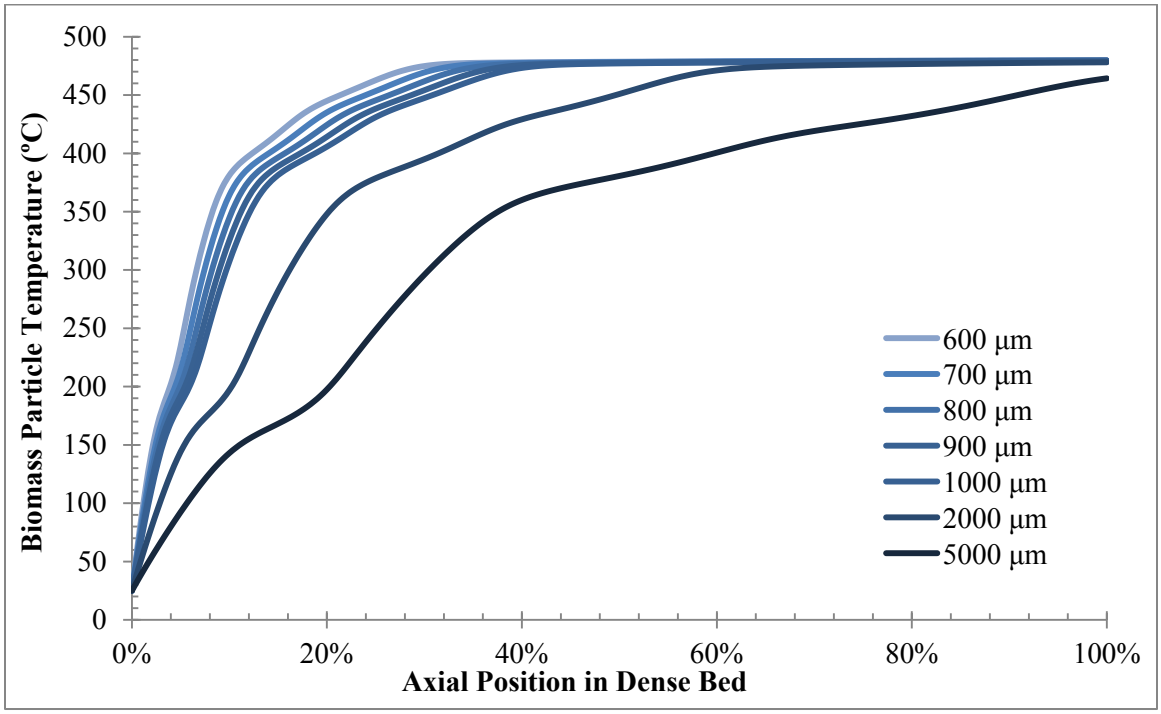

Figure 41: Biomass Temperature Profile with GBM2

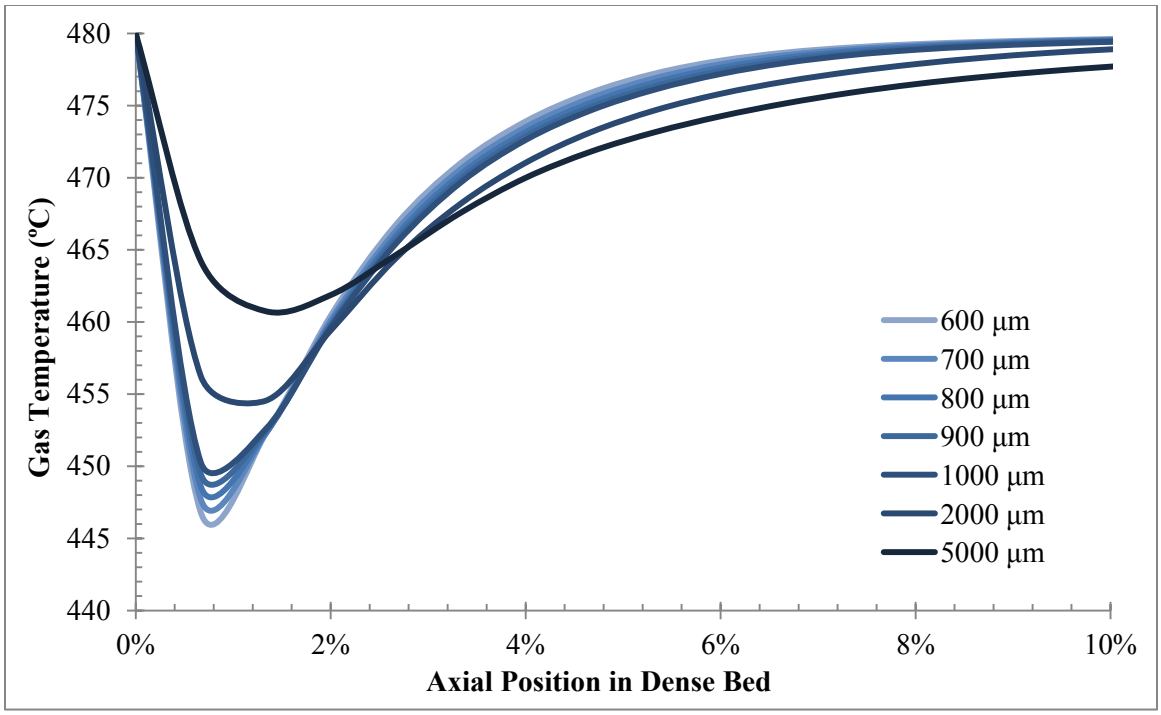

Figure 42: Gas Temperature Profile with GBM1

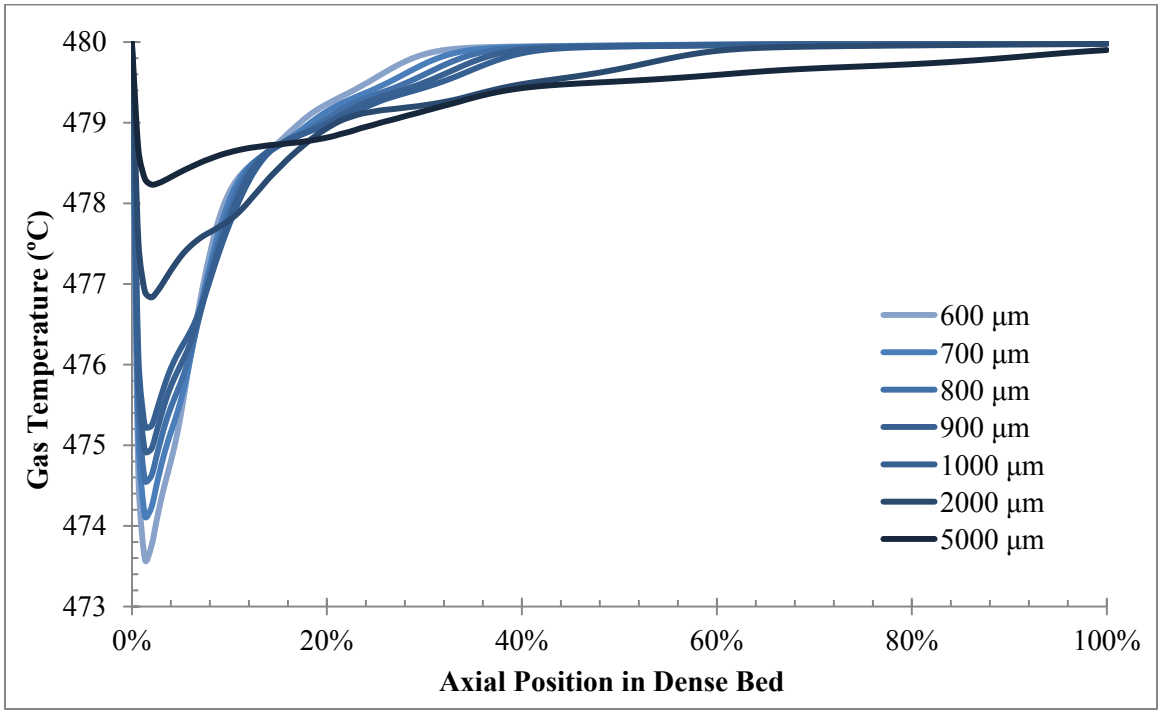

Figure 43: Gas Temperature Profile with GBM2

4.3.2. Comparing the Effect of Fluidization Velocity on Product Yields

The effect of the operating superficial gas velocity on product yields was also examined. Typically, the reactor fluidization gas velocity is one of the most easily manipulated variables in the system. A range of gas velocities was examined from minimum fluidization velocity (U_{mf}) to roughly 4 times U_{mf}. The GBM output product yields can be found in Figure 44. With the increase in superficial gas velocity, the tar yield increases while the gas yield decreases due to the decrease in the residence time of the gas. When the gas residence time is shorter, there is less time for the tarry vapors to undergo secondary reactions. The yield of char is also found to decrease, though the extent is not as prominent. This is due to the increase in the rate of heat transfer to the particles at higher gas velocities. Although, it should be noted that at higher superficial gas velocities, there is a greater risk of blowing particles out of the reactor due to fluidization regime change, especially with smaller diameter columns (such as those found in pilot-scale systems). Bubble burst and elutriation dynamics are not modelled but GBM2 shows that biomass has not completely reacted once it has reached the top of the bed which means there is a possibility of lower yields at higher velocities. A similar trend was observed between the yields of GBM1 and GBM2. The values are nearly identical, suggesting there is no real effect of in-bed hydrodynamics on product yields. At higher velocities, both GBM1 and GBM2 underestimate the yield of bio-oil which illustrates the underperformance of bubbling dynamics correlations in the slugging regime. However, the bio-oil yields observed with GBM1ISO (GBM1 under isothermal conditions) are larger by approximately 10 wt%, and closer to values observed experimentally at higher gas velocities. Additionally, while it may seem that the experimental yields seem to better match the predictions from GBM1 and GBM2 at lower gas velocities, it is believed that the experimental char yield is overvalued and that bio-oil yields should be slightly higher than observed and closer to the yields predicted by GBM1ISO. Therefore, one can conclude that the major resistance to the performance of these models lies within the implemented heat transfer mechanisms and the rate of particle heating, which seems to be underestimated by GBM1 and GBM2.

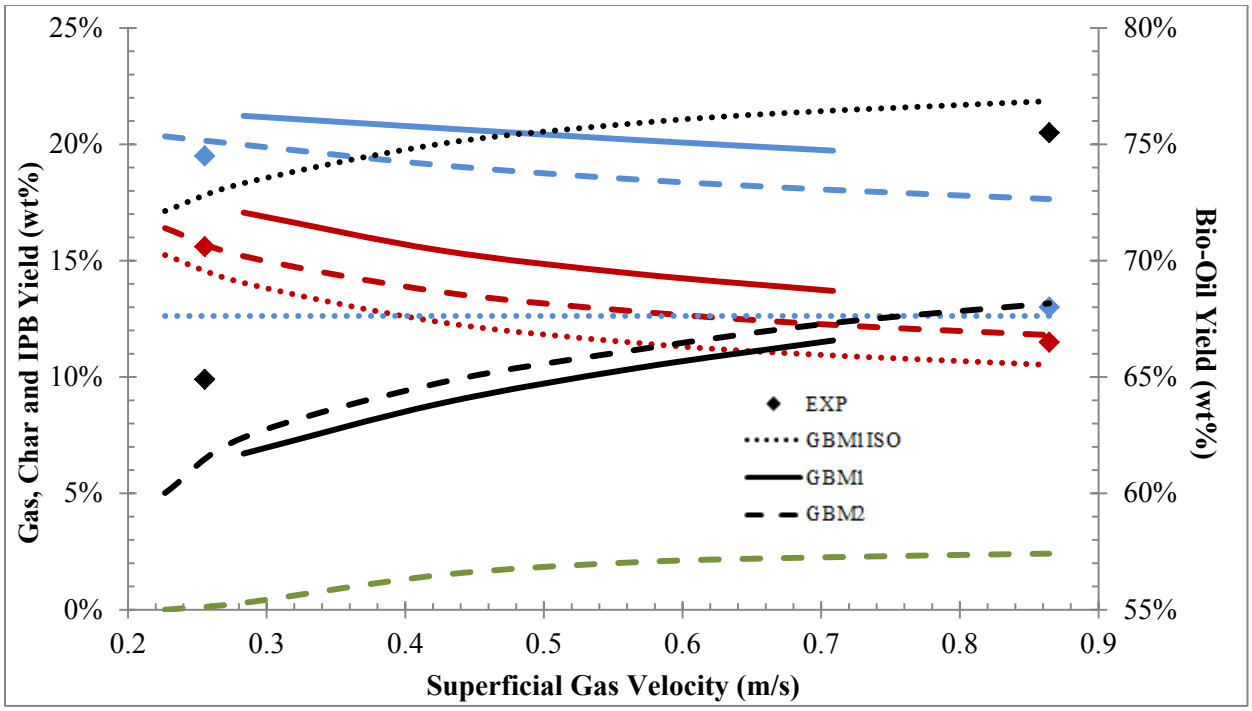

Figure 44: Effect of Superficial Gas Velocity on Product Yields (Black: Bio-Oil, Red: Gas, Blue: Char, Green: Incompletely Pyrolyzed Biomass (IPB))

4.4. Conclusions

In this investigation, the formulation of the fluidized bed hydrodynamic schemes is examined to determine if it impacts the performance of biomass fast pyrolysis. The effect of the biomass particle size and the superficial gas velocity on pyrolysis product yields was studied with two Grey-Box Models – each using distinct profiles for multi-phase flow.

It was found that the yield of bio-oil decreased with an increase in particle size and increased with an increase of the superficial gas velocity. For small particle sizes, the bio-oil yield was assumed to decrease due to particles being ejected from the bed surface following the burst of slugs. All in all, it was concluded that there is no significant effect of in-bed hydrodynamics on product yields since the yield trend of GBM1 and GBM2 were very similar. Not to mention that there are no gas-particle reactions in biomass fast pyrolysis that could be affected by local gas concentrations which are dependent of hydrodynamic formulations.

However, the biggest issue with modelling pilot or smaller scale fast pyrolysis was determined to be the change in fluidization regime from bubbling to slugging at higher fluidization velocities. This work examined whether or not bubbling dynamics correlations may be extended to also model slugging dynamics. While there seemed to be no major change in yield trends at higher fluidization velocities, the char yield was overestimated for all tested parameters. This suggests that, while a change in hydrodynamics may be insignificant, a change in the implemented the heat transfer mechanisms could greatly affect yield trends.

It is suggested that the behavior of fluid dynamics on heat transfer towards biomass particles be further examined; especially at locations less understood such as near the feed port and near the splashing zone at the top of the bed.

4.5. Appendix: Transport Equations

Equations (32) through (37) are the mass and heat balances used within the GBMs:

Mass balance for gas-phase components within bubble phase:

$$V\frac{\partial(\varepsilon_B C_{iB})}{\partial t} = -A_C\frac{\partial(\varepsilon_B C_{iB} U_B)}{\partial z} - V\varepsilon_B K_{BE}(C_{iB} - C_{ie}) + V\varepsilon_B\sum_{i=1}^{k} R_{iB} \tag{32}$$

Mass balance for gas-phase components within emulsion phase:

$$V\frac{\partial(\varepsilon_e C_{ie})}{\partial t} = -A_C\frac{\partial(\varepsilon_e C_{ie} U_e)}{\partial z} + V\varepsilon_e K_{BE}(C_{ib} - C_{ie}) + V\varepsilon_e\sum_{i=1}^{k} R_{ie} \tag{33}$$

Mass balance for solid-phase components within biomass phase:

$$V\frac{\partial(\varepsilon_b C_{ib})}{\partial t} = -A_C\frac{\partial(\varepsilon_b C_{ib} U_i)}{\partial z} + V\varepsilon_b\sum_{i=1}^{k} R_{ib} \tag{34}$$

Heat balance for biomass phase: (35)

$$\left(\varepsilon_b V\left(C_{p\,Char}C_{Char} + C_{p\,Bio}C_{Bio} + C_{P\,m}C_m\right)\right)\frac{\partial(T_{Bio})}{\partial t}$$
$$= U_i\varepsilon_b A_c\left(C_{p\,Char}C_{Char} + C_{p\,Bio}C_{Bio} + C_{P\,m}C_m\right)(T_{Bio\,in} - T_{Bio})$$
$$+ a_b h_b\left(T_{gas} - T_{Bio}\right) + a_b e_{bs}\sigma\left({T_{sand}}^4 - {T_{bio}}^4\right)$$
$$+ \begin{bmatrix}(R_{2b})\Delta H_{rxn2} + (R_{3b})\Delta H_{rxn3}\\ +\left(R_{evapb}\right)\Delta H_{evap}\end{bmatrix}(\varepsilon_b V)$$

Heat balance for gas phase:

$$(\varepsilon_e V(Cp_N C_N + Cp_G C_G + Cp_T C_T + Cp_w C_w))\frac{\partial(T_{gas})}{\partial t} \tag{36}$$
$$= U_g\varepsilon_e A_c(Cp_N C_N + Cp_G C_G + Cp_T C_T + Cp_w C_w)\left(T_{gas\,in} - T_{gas}\right)$$
$$- a_b h_b\left(T_{gas} - T_{Bio}\right) + a_s h_s\left(T_{sand} - T_{gas}\right) + (R_{4e})\Delta H_{rxn4}(\varepsilon_e V)$$

Heat balance for sand phase:

$$M_s Cp_{sand}\frac{\partial(T_{sand})}{\partial t} = -a_s h_s\left(T_{sand} - T_{gas}\right) - a_b e_{sb}\sigma\left({T_{sand}}^4 - {T_{bio}}^4\right) + \dot{Q} \tag{37}$$

Chapter 5: Conclusions and Recommendations

The ultimate goal of this work was to develop a one-dimensional Grey-Box Model (GBM) for the fluidized bed biomass fast pyrolysis unit located at NRCan CanmetENERGY's Bell's Corners Complex (BCC) and test its extensions with respect to the reaction kinetic sub-model and hydrodynamic sub-model.

The first part of the work examined the performance of the reaction kinetic sub-model by testing two multi-component and multi-step devolatilization schemes, with and without product specification, for different feedstocks and operating temperatures.

The first mechanism which was studied was the multi-component and multi-step devolatilization schemes without product specification by Miller & Bellan (1996). For low ash containing feedstocks, the mechanism output was in good agreement with experimental results and no mechanism modifications were necessary. The difference in product yields with the high ash containing feedstock, IHF, were found to be slightly higher than those with low ash suggesting that the effect of inorganic minerals may not be neglected. While the effect was not found to be significant, it is recommended that a detailed study be conducted on the magnitude of the catalytic effect for specific mineral ions embedded within the ash. The magnitude should also be numerically fitted so that it may be incorporated within future models. Unfortunately, the mechanism did not include product specification to characterize the bio-oil and was therefore found to be subpar to the second mechanism which was tested.

The second mechanism which was studied was the multi-component and multi-step devolatilization schemes with product specification by Ranzi et al. (2014). The mechanism was found to provide similar yield trends to the Miller and Bellan (1996) mechanism. Though, it underpredicted the yield of bio-oil and overpredicted the yield of char. However, examining the yield of gas and biochar for the SFPC-derived bio-oil showed a slight underprediction suggesting that yield of gas and char resulting from the devolatilization of hemicellulose and lignin components are too high. A look into the performance of the mechanism for high lignin containing feedstocks is recommended. Two major adjustments were proposed to increase the accuracy of the model. First, the scheme was extended to include additional steps accounting for

secondary reactions which fixed the yield plateau behavior at higher operating temperatures. Second, the cellulose devolatilization scheme was modified to limit the production of levoglucosan after a sensitivity analysis on the activation energy of the activated cellulose transglycosylation reaction revealed an overestimation of predicted sugar yields. A value of 50.5 kJ/mol was suggested since it minimized component class yield differences.

The Ranzi et al. (2014) mechanism did provide an insight into the quality of the bio-oil produced by specifying the bio-oil composition. While it did require additional inputs in terms of a comprehensive feedstock biochemical analysis, the level of insight gained from the quality of the bio-oil was deemed necessary for future biomass fast pyrolysis model work. The largest difficulty encountered in validating the mechanism yields was to accurately experimentally quantify the compounds in bio-oil samples. The characterization, which was done using GC-MS, was found to be sufficient when a proper classification procedure was used. Yet, the issue regarding the thermal instability of compounds under GC-MS analysis conditions, which has led to a large fraction of undetectable components, still exists and requires further studies with less thermally invasive characterization techniques. One of the main suggested techniques is HPLC and procedures are currently being investigated at CanmetENERGY. Though, using two-dimensional chromatography or using a suite of techniques such as NMR for hydroxyl groups, titration for acid content and simulated distillation by TGA to obtain a boiling point range is also suggested as future work to compare and support current methods.

The second part of the work examined the performance of the hydrodynamic sub-model by testing two GBMs, each with different in-bed profiles for multiphase flow. No significant effect of in-bed hydrodynamics on product yields was observed. It was concluded that this was largely because biomass fast pyrolysis contains no gas-particle reactions that could be affected by local gas concentrations which are dependant of hydrodynamic formulations.

The effect of biomass particle size and superficial gas velocity on pyrolysis product yields was also studied. The yield of bio-oil was found to decrease with the increase in particle size and increase with the increase of superficial gas velocity. This was analogous to trends found in literature. The model did not incorporate intra-particle resistances nor did it account for

premature elutriation before complete conversion at high velocities. Therefore, it is recommended that dynamics be reviewed to account for scenarios using large biomass particles or high fluidization velocities with fine particles.

It was observed that, while a change in hydrodynamics would be insignificant, a change in the implemented the heat transfer mechanisms could greatly affect yield trends. This was evident since the char yield was overestimated for the analysis of fluidization velocity and particle size. The influence of the heating rate on both the reaction kinetic sub-model and the hydrodynamic sub-model was only partially addressed in this work. A review on the influence of heating rate on the kinetic constants as well as a review on the dynamics of in-bed heating rates near the feed port and near the splashing zone is suggested with the use of more insightful WBMs.

References

[1] U.S Energy Information Administration, International Energy Outlook 2016, DOE/EIA-04 (2016).

[2] BP Statistical Review of World Energy, (2016) 1–48.

[3] O. Edenhofer, R. Pichs-Madruga, Y. Sokona, J.C. Minx, E. Farahani, K. Susanne, et al., Working Group III Contribution to the Fifth Assessment Report of the Intergovernmental Panel on Climate Change, Climate Change 2014: Mitigation of Climate Change. (2014) 1454. doi:10.1017/CBO9781107415416.

[4] Edugreen, Biomass, National Renewable Energy Laboratory. (2014). http://edugreen.teri.res.in/explore/renew/biomass.htm.

[5] Natural Resources Canada - About Renewable Energy, (2016). http://www.nrcan.gc.ca/energy/renewable-electricity/7295#bio.

[6] P. Tanger, J.L. Field, C.E. Jahn, M.W. Defoort, J.E. Leach, Biomass for thermochemical conversion: targets and challenges, Frontiers in Plant Science. 4 (2013) 218. doi:10.3389/fpls.2013.00218.

[7] A. V. Bridgwater, G.V.C. Peacocke, Fast Pyrolysis Processes for Biomass, Renewable & Sustainable Energy Reviews. 4 (2000) 1–73. doi:10.1016/S1364-0321(99)00007-6.

[8] D.J. Stevens, Hot Gas Conditioning: Recent Progress with Larger-Scale Biomass Gasification Systems, National Renewable Energy Laboratory. (2001) 103. doi:10.2172/786288.

[9] A.K. Rajvanshi, Biomass gasification, Alternative Energy in Agriculture. II (2014) 1–21.

[10] B. Bronson, The Effect of Pre-treating Forestry Residues on the Performance of Fluidized Bed Gasification, University of Ottawa, 2014.

[11] C. Di Blasi, Modeling chemical and physical processes of wood and biomass pyrolysis, Progress in Energy and Combustion Science. 34 (2008) 47–90. doi:10.1016/j.pecs.2006.12.001.

[12] J. Piskorz, D.S. Scott, D. Radlein, Composition of Oils Obtained by Fast Pyrolysis of Different Woods, ACS Symposium on Production, Analysis and Upgrading of Pyrolysis Oils from Biomass. (1988).

[13] R. Venderbosch, H. Heeres, Pyrolysis Oil Stabilisation by Catalytic Hydrotreatment, Biofuel's Engineering Process Technology. (2011) 385–410. doi:10.5772/18446.

[14] A. Bridgewater, Biomass fast pyrolysis, Thermal Science. 8 (2004) 21–50. doi:10.2298/TSCI0402021B.

[15] M. Calonaci, R. Grana, E. Barker Hemings, G. Bozzano, M. Dente, E. Ranzi, Comprehensive kinetic modeling study of bio-oil formation from fast pyrolysis of biomass, Energy and Fuels. 24 (2010) 5727–5734. doi:10.1021/ef1008902.

[16] P. Kaushal, T. Pröll, H. Hofbauer, Model development and validation: Co-combustion of residual char, gases and volatile fuels in the fast fluidized combustion chamber of a dual fluidized bed biomass gasifier, Fuel. 86 (2007) 2687–2695. doi:10.1016/j.fuel.2007.03.032.

[17] A. Milioni, Gasification Process, Oil & Gas Portal. (2015). http://www.oil-gasportal.com/gasification-process/#_ftnref14.

[18] J. Bruchmüller, B.G.M. van Wachem, S. Gu, K.H. Luo, R.C. Brown, Modeling the Thermochemical Degradation of Biomass Inside a Fast Pyrolysis Fluidized Bed Reactor, AIChE Journal. 58 (2012) 3030–3042. doi:10.1002/aic.13705.

[19] B. V. Babu, A.S. Chaurasia, Pyrolysis of biomass: Improved models for simultaneous kinetics and transport of heat, mass and momentum, Energy Conversion and Management. 45 (2004) 1297–1327. doi:10.1016/j.enconman.2003.09.013.

[20] P. Basu, P. Kaushal, Modeling of Pyrolysis and Gasification of Biomass in Fluidized Beds: A Review, Chemical Product and Process Modeling. 4 (2009). doi:10.2202/1934-2659.1338.

[21] R.W. Chan, M. Kelbon, B. Krieger-Brockett, Single-Particle Biomass Pyrolysis: Correlations of Reaction Products with Process Conditions, Industrial & Engineering Chemistry Research. 27 (1988) 2261–2275. doi:10.1021/ie00084a012.

[22] W.-C.R. Chan, M. Kelbon, B.B. Krieger, Modelling and experimental verification of physical and chemical processes during pyrolysis of a large biomass particle, Fuel. 64 (1985) 1505–1513. doi:10.1016/0016-2361(85)90364-3.

[23] Q. Xiong, F. Xu, E. Ramirez, S. Pannala, S. Daw, Modeling the impact of bubbling bed hydrodynamics on tar yield and its fluctuations during biomass fast pyrolysis, Fuel. 164 (2016) 11–17. doi:10.1016/j.fuel.2015.09.074.

[24] R. Difelice, G. Coppola, S. Rapagna, N. Jand, Modeling of Biomass Devolatilization in a Fluidized Bed Reactor, The Canadian Journal of Chemical Engineering. 77 (1999) 325–

332. doi:10.1002/cjce.5450770219.

[25] A. Gómez-Barea, B. Leckner, Modeling of biomass gasification in fluidized bed, Progress in Energy and Combustion Science. 36 (2010) 444–509. doi:10.1016/j.pecs.2009.12.002.

[26] Y. Haseli, J. Van Oijen, L. De Goey, A Simplified Pyrolysis Model of a Biomass Particle Based on Infinitesimally Thin Reaction Front Approximation, Energy & Fuels. 26 (2012) 3230–3243. doi:10.1021/ef3002235.

[27] M.A. Hastaoglu, M.S. Hassam, Application of a general gas-solid reaction model to flash pyrolysis of wood in a circulating fluidized bed, Fuel. 74 (1995) 697–703. doi:10.1016/0016-2361(94)00010-O.

[28] P. Kaushal, S.A. Mirhidi, J. Abedi, Fast Pyrolysis of Biomass in Bubbling Fluidized Bed: A Model Study, Chemical Product and Process Modeling. 6 (2011) 22. doi:10.2202/1934-2659.1545.

[29] S.D. Kenarsari, Y. Zheng, A Numerical Modeling of Fast Pyrolysis of Spherical Biomass Particles, in: ASME 2012 International Mechanical Engineering Congress & Exposition, 2012: pp. 1119–1126. doi:10.1115/IMECE2012-87768.

[30] S.R.A. Kersten, X. Wang, W. Prins, W.P.M. van Swaaij, Biomass Pyrolysis in a Fluidized Bed Reactor. Part 1: Literature Review and Model Simulations, Industrial & Engineering Chemistry Research. 44 (2005) 8773–8785. doi:10.1021/ie0504856.

[31] D. Lathouwers, J. Bellan, Modeling of dense gas-solid reactive mixtures applied to biomass pyrolysis in a fluidized bed, International Journal of Multiphase Flow. 27 (2001) 2155–2187. doi:10.1016/S0301-9322(01)00059-3.

[32] D. Lathouwers, J. Bellan, Modeling of Biomass Pyrolysis for Hydrogen Production: The Fluidized Bed Reactor, in: Proceedings of the 2001 DOE Hydrogen Program Review, 2001: pp. 1–35.

[33] Z. Luo, S. Wang, K. Cen, A model of wood flash pyrolysis in fluidized bed reactor, Renewable Energy. 30 (2005) 377–392. doi:10.1016/j.renene.2004.03.019.

[34] K. Papadikis, S. Gu, A. V. Bridgwater, CFD modelling of the fast pyrolysis of biomass in fluidised bed reactors: Modelling the impact of biomass shrinkage, Chemical Engineering Journal. 149 (2009) 417–427. doi:10.1016/j.cej.2009.01.036.

[35] K. Papadikis, S. Gu, A. Fivga, A. V. Bridgwater, Numerical Comparison of the Drag Models of Granular Flows Applied to the Fast Pyrolysis of Biomass, Energy and Fuels. 24

(2010) 2133–2145. doi:10.1021/ef901497b.

[36] R. Radmanesh, Y. Courbariaux, J. Chaouki, C. Guy, A unified lumped approach in kinetic modeling of biomass pyrolysis, Fuel. 85 (2006) 1211–1220. doi:10.1016/j.fuel.2005.11.021.

[37] P. Ranganathan, S. Gu, Computational fluid dynamics modelling of biomass fast pyrolysis in fluidised bed reactors, focusing different kinetic schemes, Elsevier Ltd, 2015. doi:10.1016/j.biortech.2016.02.042.

[38] A.K. Sadhukhan, P. Gupta, R.K. Saha, Modelling and experimental studies on pyrolysis of biomass particles, Journal of Analytical and Applied Pyrolysis. 81 (2008) 183–192. doi:10.1016/j.jaap.2007.11.007.

[39] A. Sharma, S. Wang, V. Pareek, H. Yang, D. Zhang, Multi-fluid reactive modeling of fluidized bed pyrolysis process, Chemical Engineering Science. 123 (2015) 311–321. doi:10.1016/j.ces.2014.11.019.

[40] M. Sreekanth, Ajit Kumar Kolar, B. Leckner, Transient thermal behaviour of a cylindrical wood particle during devolatilization in a bubbling fluidized bed, Fuel Processing Technology. 89 (2008) 838–850. doi:10.1016/j.fuproc.2008.02.003.

[41] A. Trendewicz, R. Braun, A. Dutta, J. Ziegler, One dimensional steady-state circulating fluidized-bed reactor model for biomass fast pyrolysis, Fuel. 133 (2014) 253–262. doi:10.1016/j.fuel.2014.05.009.

[42] X. Wang, S.R.A. Kersten, W. Prins, W.P.M. van Swaaij, Biomass Pyrolysis in a Fluidized Bed Reactor. Part 2: Experimental Validation of Model Results, Industrial & Engineering Chemistry Research. 44 (2005) 8786–8795. doi:10.1021/ie050486y.

[43] Q. Xiong, S. Aramideh, S.-C. Kong, Modeling Effects of Operating Conditions on Biomass Fast Pyrolysis in Bubbling Fluidized Bed Reactors, Energy & Fuels. 27 (2013) 5948–5956. doi:10.1021/ef4012966.

[44] Q. Xiong, S. Aramideh, A. Passalacqua, S.C. Kong, BIOTC: An open-source CFD code for simulating biomass fast pyrolysis, 2014. doi:10.1016/j.cpc.2014.02.012.

[45] W.-C. Yang, Handbook of Fluidization and Fluid-Particle Systems, CRC Press. (2003) 851.

[46] D. Kunii, O. Levenspiel, Bubbling Bed Model, I&EC Fundamentals. 7 (1968) 446–452. doi:10.1021/i160027a016.

[47] Davidson, Harrison, G. de Carvalho, On the Liquidlike Behavior of Fluidized Beds, Annual Review of Fluid Mechanics. 9 (1977) 55–86.

[48] K. Kato, C.Y. Wen, Bubble assemblage model for fluidized bed catalytic reactors, Chemical Engineering Science. 24 (1969) 1351–1369. doi:10.1016/0009-2509(69)85055-4.

[49] C. Fryer, O.E. Potter, Countercurrent Backmixing Model for Fluidized Bed Catalytic Reactors. Applicability of Simplified Solutions, Industrial & Engineering Chemistry Fundamentals. 11 (1972) 338–344. doi:10.1021/i160043a009.

[50] M. Bidabadi, M.R. Moghaddam, S.A. Mostafavi, F.F. Dizaji, H.B. Dizaji, An analytical model for pyrolysis of a single biomass particle, Journal of Central South University. 22 (2015) 350–359. doi:10.1007/s11771-015-2529-3.

[51] M.W. van de Weerdhof, Modeling the pyrolysis process of biomass particles, Eindhoven University of Technology, 2010.

[52] G. Mazziotti di Celso, S. Rapagnà, M. Prisciandaro, E.F. Zanoelo, Kinetics of pyrolysis and combustion of spherical wood particles in a fluidized bed, Energy Conversion and Management. 82 (2014) 27–36. doi:10.1016/j.enconman.2014.03.005.

[53] S. Koppatz, C. Pfeifer, H. Hofbauer, Comparison of the performance behaviour of silica sand and olivine in a dual fluidised bed reactor system for steam gasification of biomass at pilot plant scale, Chemical Engineering Journal. 175 (2011) 468–483. doi:10.1016/j.cej.2011.09.071.

[54] T. Sfetsas, C. Michailof, A. Lappas, Q. Li, B. Kneale, Qualitative and quantitative analysis of pyrolysis oil by gas chromatography with flame ionization detection and comprehensive two-dimensional gas chromatography with time-of-flight mass spectrometry, Journal of Chromatography A. 1218 (2011) 3317–3325. doi:10.1016/j.chroma.2010.10.034.

[55] U.S. Deparment of Energy, Energy Efficiency & Renewable Energy : Bioenergy Technologies Office, 2014.

[56] S. Czernik, A. Bridgwater, Overview of Applications of Biomass Fast Pyrolysis Oil, Energy & Fuels. 18 (2004) 590–598. doi:Doi 10.1021/Ef034067u.

[57] A. Oasmaa, S. Czernik, Fuel Oil Quality of Biomass Pyrolysis Oils-State of the Art for the End Users, Energy & Fuels. 13 (1999) 914–921. doi:10.1016/S0140-6701(00)96592-5.

[58] C. Di Blasi, M. Lanzetta, Intrinsic kinetics of isothermal xylan degradation in inert atmosphere, Journal of Analytical and Applied Pyrolysis. 40-41 (1997) 287–303. doi:10.1016/S0165-2370(97)00028-4.

[59] M.J. Antal, A Review of the Vapor Phase Pyrolysis of Biomass Derived Volatile Matter, Fundamentals of Thermochemical Biomass Conversion. (1985) 511–537.

[60] C.A. Koufopanos, N. Papayannakos, G. Maschio, A. Luccesi, Modelling of the Pyrolysis of Biomass Particles, Studies on Kinetics, Thermal and Heat Transfer Effects, Canadian Journal of Chemical Engineeringneering. 69 (1991) 907–915. doi:10.1002/cjce.5450690413.

[61] C.A. Koufopanos, A. Lucchesi, G. Maschio, Kinetic Modelling of the Pyrolysis of Biomass and Biomass Components, The Canadian Journal of Chemical Engineering. 67 (1989) 75–84. doi:10.1002/cjce.5450670111.

[62] F. Shafizadeh, P.P.S. Chin, Thermal Deterioration of Wood, ACS Symposium Series American Chemical Society. (1977).

[63] J.L. Banyasz, S. Li, J. Lyons-Hart, K.H. Shafer, Gas evolution and the mechanism of cellulose pyrolysis, Fuel. 80 (2001) 1757–1763. doi:10.1016/S0016-2361(01)00060-6.

[64] J.A. Knight, C.W. Gorton, R.J. Kovac, Oil Production by Entrained Flow Pyrolysis of Biomass, Biomass. 6 (1984) 69–76. doi:10.1016/0144-4565(84)90009-X.

[65] S.M. Ward, J. Braslaw, Experimental Weight Loss Kinetics of Wood Pyrolysis under Vacuum, Combustion and Flame. 61 (1985) 261–269. doi:10.1016/0010-2180(85)90107-5.

[66] T.R. Nunn, J.B. Howard, J.P. Longwell, W.A. Peters, Product Compositions and Kinetics in the Rapid Pyrolysis of Sweet Gum Hardwood, Industrial & Engineering Chemistry Process Design and Development. 24 (1985) 836–844.

[67] R. Font, A. Marcilla, E. Verdii, J. Devesa, Kinetics of the Pyrolysis of Almond Shells and Almond Shells Impregnated with CoCl2 in a Fluidized Bed Reactor and in a Pyroprobe 100, Industrial & Engineering Chemistry Research. (1990) 1846–1855. doi:10.1021/ie00105a016.

[68] M.C. Samolada, I.A. Vasalos, A kinetic approach to the flash pyrolysis of biomass in a fluidized bed reactor, Fuel. 70 (1991) 883–889. doi:10.1016/0016-2361(91)90200-T.

[69] J. Reina, E. Velo, L. Puigjaner, Thermogravimetric Study of the Pyrolysis of Waste

Wood, Thermochimica Acta. 320 (1998) 161–167. doi:10.1016/S0040-6031(98)00427-4.

[70] F. Thurner, U. Mann, Kinetic Investigation of Wood Pyrolysis, Industrial & Engineering Chemistry Process Design and Development. 20 (1981) 482–488. doi:10.1021/i200014a015.

[71] C. Branca, C. Di Blasi, R. Elefante, F. Ii, P. V Tecchio, Devolatilization and Heterogeneous Combustion of Wood Fast Pyrolysis Oils, (2005) 799–810.

[72] M. Grønli, M. Melaaen, Mathematical Model for Wood Pyrolysis - Comparison of Experimental Measurements with Model Predictions, Energy & Fuels. 14 (2000) 791–800. doi:10.1021/ef990176q.

[73] A.G.W. Bradbury, Y. Sakai, F. Shafizadeh, Kinetic Model for Pyrolysis of Cellulose., Journal of Applied Polymer Science. 23 (1979) 3271–3280. doi:10.1002/app.1979.070231112.

[74] E. Ranzi, A. Cuoci, T. Faravelli, A. Frassoldati, G. Migliavacca, S. Pierucci, et al., Chemical Kinetics of Biomass Pyrolysis, Energy and Fuels. 22 (2008) 4292–4300.

[75] J. Lédé, Biomass Fast Pyrolysis Reactors: A Review of a Few Scientific Challenges and of Related Recommended Research Topics, Oil & Gas Science and Technology – Revue d'IFP Energies Nouvelles. 68 (2013) 801–814. doi:10.2516/ogst/2013108.

[76] P. Morf, P. Hasler, T. Nussbaumer, Mechanisms and kinetics of homogeneous secondary reactions of tar from continuous pyrolysis of wood chips, Fuel. 81 (2002) 843–853. doi:10.1016/S0016-2361(01)00216-2.

[77] E.J. Shin, M.R. Nimlos, R.J. Evans, Kinetic analysis of the gas-phase pyrolysis of carbohydrates, Fuel. 80 (2001) 1697–1709. doi:10.1016/S0016-2361(01)00056-4.

[78] M.G. Grønli, G. Várhegyi, C. Di Blasi, Thermogravimetric Analysis and Devolatilization Kinetics of Wood, Industrial & Engineering Chemistry Research. 41 (2002) 4201–4208. doi:10.1021/ie0201157.

[79] T. Hosoya, H. Kawamoto, S. Saka, Cellulose-hemicellulose and cellulose-lignin interactions in wood pyrolysis at gasification temperature, Journal of Analytical and Applied Pyrolysis. 80 (2007) 118–125. doi:10.1016/j.jaap.2007.01.006.

[80] R.S. Miller, J. Bellan, A Generalized Biomass Pyrolysis Model Based on Superimposed Cellulose, Hemicelluloseand Liqnin Kinetics, Combustion Science and Technology. 126 (1997) 97–137. doi:10.1080/00102209708935670.

[81] D. Ferdous, A.K. Dalai, S.K. Bej, R.W. Thring, Pyrolysis of Lignins: Experimental and Kinetics Studies, Energy and Fuels. 16 (2002) 1405–1412. doi:10.1021/ef0200323.

[82] E. Ranzi, M. Corbetta, F. Manenti, S. Pierucci, Kinetic modeling of the thermal degradation and combustion of biomass, Chemical Engineering Science. 110 (2014) 2–12. doi:10.1016/j.ces.2013.08.014.

[83] M. Van de Velden, J. Baeyens, A. Brems, B. Janssens, R. Dewil, Fundamentals, kinetics and endothermicity of the biomass pyrolysis reaction, Renewable Energy. 35 (2010) 232–242. doi:10.1016/j.renene.2009.04.019.

[84] A. Anca-Couce, R. Mehrabian, R. Scharler, I. Obernberger, Kinetic scheme of biomass pyrolysis considering secondary charring reactions, Energy Conversion and Management. 87 (2014) 687–696. doi:10.1016/j.enconman.2014.07.061.

[85] P. Mellin, E. Kantarelis, W. Yang, Computational fluid dynamics modeling of biomass fast pyrolysis in a fluidized bed reactor, using a comprehensive chemistry scheme, Fuel. 117 (2014) 704–715. doi:10.1016/j.fuel.2013.09.009.

[86] A. Anca-Couce, Reaction mechanisms and multi-scale modelling of lignocellulosic biomass pyrolysis, Progress in Energy and Combustion Science. 53 (2016) 41–79. doi:10.1016/j.pecs.2015.10.002.

[87] A. Cuoci, T. Faravelli, A. Frassoldati, S. Granata, G. Migliavacca, S. Pierucci, et al., A General Mathematical Model of Biomass Devolatilization Note 2. Detailed kinetics of volatile species, in: 30th Meeting of the Italian Section of the Combustion Institute, 2007: pp. 1–6.

[88] Three types of mathematical models of complex dynamic systems, BioDiverse Perspectives. (2014). http://www.biodiverseperspectives.com/2014/10/07/the-dark-side-of-theoretical-ecology/.

[89] D.S. Scott, J. Piskorz, M.A. Bergougnou, R.P. Overend, R. Graham, The Role of Temperature in the Fast Pyrolysis of Cellulose and Wood, Industrial & Engineering Chemistry Research. 27 (1988) 8–15. doi:10.1021/ie00073a003.

[90] F. Shafizadeh, Pyrolytic reactions and products of biomass, Fundamentals of Thermochemical Biomass Conversion. (1985) 183–217.

[91] P. Kaushal, J. Abedi, A simplified model for biomass pyrolysis in a fluidized bed reactor, Journal of Industrial and Engineering Chemistry. 16 (2010) 748–755.

doi:10.1016/j.jiec.2010.07.008.

[92] NIST Chemistry WebBook, NIST Standard Reference Database Number 69. (2011) http://webbook.nist.gov/chemistry/. doi:10.5860/CHOICE.35-2709.

[93] D. Mohan, C.U. Pittman, P.H. Steele, Pyrolysis of Wood/Biomass for Bio-oil: A Critical Review, Energy & Fuels. 20 (2006) 848–889.

[94] C. Branca, P. Giudicianni, C. Di Blasi, GC / MS Characterization of Liquids Generated from Low-Temperature Pyrolysis of Wood, Industrial & Engineering Chemistry Research. (2003) 3190–3202.

[95] C.A. Mullen, A.A. Boateng, Chemical Composition of Bio-oils Produced by Fast Pyrolysis of Two Energy Crops, Energy & Fuels. (2008) 2104–2109.

[96] R.J.M. Westerhof, D.W.F. (Wim) Brilman, W.P.M. van Swaaij, S.R.A. Kersten, Effect of Temperature in Fluidized Bed Fast Pyrolysis of Biomass: Oil Quality Assessment in Test Units, Industrial & Engineering Chemistry Research. 49 (2010) 1160–1168. doi:10.1021/ie900885c.

[97] M. Milhé, L. van de Steene, M. Haube, J.M. Commandré, W.F. Fassinou, G. Flamant, Autothermal and allothermal pyrolysis in a continuous fixed bed reactor, Journal of Analytical and Applied Pyrolysis. 103 (2013) 102–111. doi:10.1016/j.jaap.2013.03.011.

[98] J. Blondeau, H. Jeanmart, Biomass pyrolysis at high temperatures: Prediction of gaseous species yields from an anisotropic particle, Biomass and Bioenergy. 41 (2012) 107–121. doi:10.1016/j.biombioe.2012.02.016.

[99] A. Trendewicz, R. Evans, A. Dutta, R. Sykes, D. Carpenter, R. Braun, Evaluating the effect of potassium on cellulose pyrolysis reaction kinetics, Biomass and Bioenergy. 74 (2015) 15–25. doi:10.1016/j.biombioe.2015.01.001.

[100] X. Zhang, W. Yang, C. Dong, Levoglucosan formation mechanisms during cellulose pyrolysis, Journal of Analytical and Applied Pyrolysis. 104 (2013) 19–27. doi:10.1016/j.jaap.2013.09.015.

[101] M.R. Rover, R.C. Brown, Analysis of sugars and phenolic compounds in bio- oil by, Iowa State University, 2013.

[102] P.R. Patwardhan, J.A. Satrio, R.C. Brown, B.H. Shanks, Influence of inorganic salts on the primary pyrolysis products of cellulose, Bioresource Technology. 101 (2010) 4646–4655. doi:10.1016/j.biortech.2010.01.112.

[103] P.R. Patwardhan, Understanding the product distribution from biomass fast pyrolysis, Iowa State University, 2010.

[104] V. Seshadri, P.R. Westmoreland, Concerted Reactions and Mechanism of Glucose Pyrolysis and Implications for Cellulose Kinetics, Journal of Physical Chemistry A. 116 (2012) 11997–12013. doi:10.1021/jp3085099.

[105] H.B. Mayes, L.J. Broadbelt, Unraveling the Reactions that Unravel Cellulose, Journal of Physical Chemistry A. 116 (2012) 7098–7106. doi:10.1021/jp300405x.

[106] D. Kunii, O. Levenspiel, Fluidization Engineering, 2nd Ed., 1990.

[107] E.D. Gordillo, A. Belghit, A two phase model of high temperature steam-only gasification of biomass char in bubbling fluidized bed reactors using nuclear heat, International Journal of Hydrogen Energy. 36 (2011) 374–381. doi:10.1016/j.ijhydene.2010.09.088.

[108] Z.Y. Zhou, A.B. Yu, P. Zulli, Particle Scale Study of Heat Transfer in Packed and Bubbling Fluidized Beds, AIChE Journal. 55 (2009) 17. doi:10.1002/aic.11823.

[109] G.K. Roy, J.R. Sarma, Fluidized bed heat transfer, Chemical Processing & Engineering. (1970) 8.

[110] R.C. Darton, R.D. LaNauze, J.F. Davidson, D. Harrison, Bubble Growth Due to Coalesence in Fluidised Beds, Transactions of The Institution of Chemical Engineers. 55 (1977) 274–280.

[111] D. Geldart, The Effect of Particle Size and Size Distribution on the Behaviour of Gas-Fluidised Beds, Powder Technology. 6 (1972) 201–215.

[112] S. Mori, C.Y. Wen, Estimation of Bubble Diameter in Gaseous Fluidized Beds, AIChE Journal. 21 (1975) 109–115. doi:10.1002/aic.690210114.

[113] P.N. Rowe, Prediction of Bubble Size in a Gas Fluidised Bed, Chemical Engineering Science. 31 (1976) 285–288.

[114] J.-H. Choi, J.E. Son, S.D. Kim, Bubble Size and Frequency in Gas Fluidized Beds, Journal of Chemical Engineering of Japan. 21 (1988) 171–178.

[115] M. Rüdisüli, Characterization of rising gas bubbles in fluidized beds by means of statistical tools, Paul Scherrer Institut, 2012.

[116] Archimedes' Hat-Box Theorem, Wolfram MathWorld. (2016). http://mathworld.wolfram.com/ArchimedesHat-BoxTheorem.html.

[117] H.P. Meissner, C.L. Kusik, Particle Velocities in a Gas Fluidized Bed, The Canadian

Journal of Chemical Engineering. 48 (1970) 349–355.

[118] R. Radmanesh, R. Mabrouk, J. Chaouki, C. Guy, Effect of Temperature on Solids Mixing in a Bubbling Fluidized Bed Reactor, International Journal of Chemical Reactor Engineering. 3 (2005) 16. doi:10.2202/1542-6580.1262.

[119] H. Thunman, Principles and Models of Solid Fuel Combustion, Chalmers University of Technology, 2001.

[120] Q. Xiong, S. Aramideh, S.-C. Kong, Assessment of Devolatilization Schemes in Predicting Product Yields of Biomass Fast Pyrolysis, Environmental Progress & Sustainable Energy. 33 (2014) 756–761. doi:10.1002/ep.11922.

[121] P. Kaushal, J. Abedi, N. Mahinpey, A comprehensive mathematical model for biomass gasification in a bubbling fluidized bed reactor, Fuel. 89 (2010) 3650–3661. doi:10.1016/j.fuel.2010.07.036.

[122] H. Bashiri, R. Sotudeh-Gharebagh, A. Sarvar-Amini, A. Haghtalab, N. Mostoufi, Comparative simulation of a fluidised bed reformer using industrial process simulators, International Journal of Sustainable Energy. 35 (2016) 664–674. doi:10.1080/14786451.2014.932280.

[123] D. Andersson, M. Karlsson, Investigation of the Effects of Introducing Hydrodynamic Parameters into a Kinetic Biomass Gasification Model for a Bubbling Fluidized Bed, Mälardalen University, 2014.

Appendices

Appendix A: Model Graphical User Interface, Input Screens and Output Screens

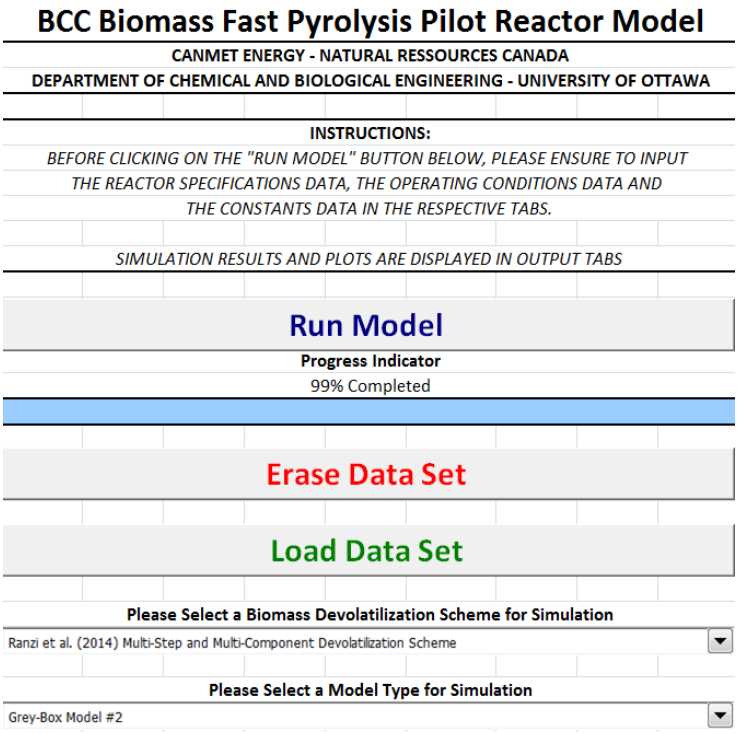

Figure 45: Model Run Screen

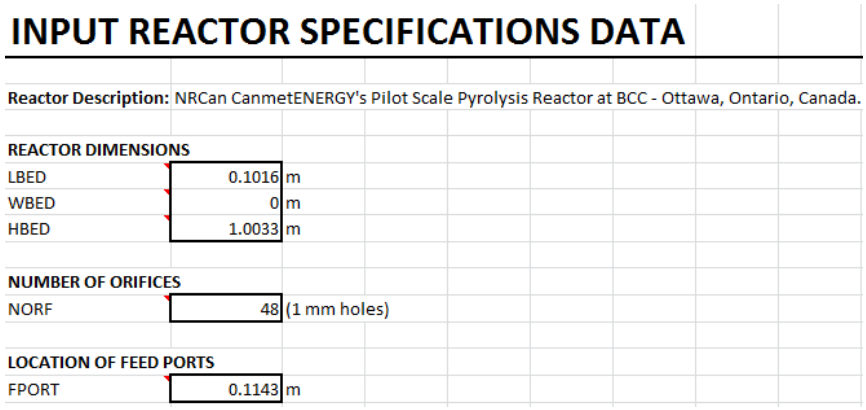

Figure 46: Input Reactor Specifications Screen

INPUT OPERATING CONDITIONS DATA

Run Description: 14640_01
Biomass Description: Hardwood Sawdust (HWS)
Sand Description: 32-B4 Olivine Sand

Bed Temperature			Sand Properties			Biomass Ultimate Analysis			Heat Transfer Constants		
TEMP	480	°C	SMASS	3.756	kg	C	45.6	%wt	Cp Char	1100	J/Kg K
Setpoint Temp	480	°C	SDIA	613.264	um	H	5.54	%wt	Cp Biomass	2300	J/Kg K
Static Pressre			SSPH	1		O	41.1	%wt	Cp Water (l)	4200	J/Kg K
PRESS	101.325	kPa	SPDEN	2830	kg/m3	N	0.11	%wt	Cp Water (g)	2147	J/Kg K
			SBDEN	1515	kg/m3	S	0.05	%wt	Cp N2	1121	J/Kg K
Pressure Drop			EMSAND	0.76					Cp Bio-Oil	2500	J/Kg K
PDROP	-	kPa				**Fluidizing Gas Properties**			Cp Gas	1100	J/Kg K
			Biomass Properties			GFLOW	152.5	slpm			
Fluidizing Gas Composition			BMOIS	7.27	%wt	GDEN	0.453	kg/m3	TCOND N2	0.0563	W/M K
H2O	0	%wt	BASH	0.36	%wt	GVIS	3.3652E-05	Pa s	TCOND Gas	0.02577	W/M K
N2	100	%wt	BVOLS	79.04	%wt						
O2	0	%wt	BFC	13.33	%wt	**Differential Pressure at Feed**			**Model Parameters**		
CO2	0	%wt	BDIA	5000	um	DPF	1.1	"WC	dt	0.00031	s
CO	0	%wt	BSPH	1					End Time	60	s
H2	0	%wt	BPDEN	500	kg/m3	**Biomass Composition**			bubFreq	0.1	/s
CH4	0	%wt	BBDEN	800	kg/m3	Cellulose (CELL)	40	%wt	Slug Fraction Criteria	0.8	
			BCALVAL	18.16	MJ/Kg	Hemicellulose (HCE)	38	%wt	BIOVEL	0.05	m/s
			BFRATE	6.5	kg/h ash-free	Carbon-rich Lignin (LIGC)	22	%wt	NCELL	150	Cells
			BMASS	25.1	kg	Hydrogen-rich Lignin (LIGH)	0		TOL	0.0001	
			EMBIO	0.9		Oxygen-rich Lignin (LIGO)	0				
			BTEMP	25.0	°C						

Figure 47: Input Operating Conditions, Material Specifications and Model Parameters Screen

INPUT CONSTANTS DATA

Kinetic Parameters for Miller & Bellan (1996) Mechanism

Component	Cellulose		Hemicellulose		Lignin		Reaction Heat
	A (1/s)	E (kJ/mol)	A (1/s)	E (kJ/mol)	A (1/s)	E (kJ/mol)	kJ/kg
k1	2.8E+19	242.4	2.1E+16	186.7	9.60E+08	107.6	0
k2	3.28E+14	196.5	8.75E+15	202.4	1.50E+09	143.8	418
k3	1.30E+10	150.5	2.6E+11	145.7	7.70E+06	111.4	418
v	0.35		0.6		0.75		
	A (1/s)	E (kJ/mol)					
k4	4280000	108					-42

	Water		Reaction Heat
	A (1/s)	E (kJ/mol)	kJ/kg
kw	5.13E+10	88	2244

Kinetic Parameters for the Modified Ranzi et al. (2014) Mechanism

Reaction #	A (1/s)	E (kJ/mol)	T exponent	ΔH^0_R (kJ/kg)	Notes	Reaction #	Reactions
1	4E+13	188.3633	0	0	Unchanged	1	CELL→CELLA
2	5.00E+08	150.5	0	620	Unchanged	2	CELLA→.8HAA+.2GLYOX+.1C2H4O+.25HMFU+.3C3H
3	1.8	50.5	1	364	Modified	3	CELLA→LVG
4	4.00E+07	129.7614	0	-1913	Unchanged	4	CELL→5H2O+6Char
5	3.30E+09	129.7614	0	100	Unchanged	5	HCE→.4HCE1+.6HCE2
6	1.00E+09	133.9473	0	-92	Unchanged	6	HCE1→.025H2O+.5CO2+.025HCOOH+.5CO+.8CH2O
7	0.05	33.48681	1	-1860	Unchanged	7	HCE1→.25H2O+.5CO2+.05HCOOH+.3CO+.15G{CO}+
8	0.9	46.04437	1	588	Unchanged	8	HCE1→XYLAN
9	3.30E+09	138.1331	0	212	Unchanged	9	HCE2→.2H2O+.175CO+.275CO2+.5CH2O+.1C2H5OH
10	1.33E+15	203.0138	0	-490	Unchanged	10	LIGC→.35LIGCC+.1COUMARYL+.08PHENOL+.41C2H
11	6.70E+12	156.9694	0	100	Unchanged	11	LIGH→LIGOH+C3H6O
12	3.30E+08	106.7392	0	446	Unchanged	12	LIGO→LIGOH+G{CO2}
13	1.60E+06	131.8543	0	-503	Unchanged	13	LIGCC→.3COUMARYL+.2PHENOL+.35HAA+.7H2O+
14	5.00E+07	125.5756	0	-120	Unchanged	14	LIGOH→LIG+.15G{H2}+.9H2O+.1CH4+.5CH3OH+.5
15	33	62.78778	0	-1604	Unchanged	15	LIGOH+1.5H2O+.5CO+.1CH4+.5G{H2}+1.6G{CO}+3
16	2.4	50.23022	1	686	Unchanged	16	LIG→FE2MACR
17	4.00E+08	125.5756	0	-470	Unchanged	17	LIG→.95H2O+.2CH2O+.4CH3OH+CO+.2CH4+.05HCO
18	0.083	33.48681	1	-1663	Unchanged	18	LIG→.6H2O+.4CO+.2CH4+.4CH2O+.2G{CO}+.4G{CH
19	1.00E+06	100.4604	0	-1814	Unchanged	19	G{CO2}→CO2
20	5.00E+12	209.2926	0	-2000	Unchanged	20	G{CO}→CO
21	5.00E+11	297.1955	0	6778	Unchanged	21	G{COH2}→CO+H2
22	5.00E+11	313.9389	0	0	Unchanged	22	G{H2}→H2
23	5.00E+12	300.1256	0	0	Unchanged	23	G{CH4}→CH4
24	5.00E+12	300.1256	0	0	Unchanged	24	G{C2H4}→C2H4
25	2.00E+12	209.2926	0	0	Unchanged	25	G{CH3OH }→CH3OH
26	5.13E+10	88	0	2244	Sreekanth et al	26	H2OB→H2OG
27	4280000	108	0	642.7	Blondeau et al.		
28	4280000	108	0	1878.2	Blondeau et al.		

Component #	Component ID	Component Name	C	H	O	Molar Mass
1	CELL	Cellulose	6	10	5	162.142
2	CELLA	Activated Cellulo	6	10	5	162.142
3	HCE	Hemicellulose	5	8	4	132.1158
4	HCE1	Activated Hemice	5	8	4	132.1158
5	HCE2	Activated Hemice	5	8	4	132.1158
6	LIGC	Carbon-rich Ligni	15	14	4	258.2732
7	LIGH	Hydrogen-rich Lig	22	28	9	436.4578
8	LIGO	Oxygen-rich Ligni	20	22	10	422.3878
9	LIGCC	Carbon-rich Ligni	15	14	4	258.2732
10	LIGOH	OH-rich Lignin	19	22	8	378.378
11	LIG	Lignin	11	12	4	208.2134
12	Char	Char	1	0	0	12.011
13	H2OB	Moisture	0	2	1	18.0152
14	G{CO2}	Trapped Carbon I	1	0	2	44.0098
15	G{CO}	Trapped Carbon I	1	0	1	28.0104
16	G{COH2}	Trapped Formalc	1	2	1	30.0262
17	G{H2}	Trapped Hydroge	0	2	0	2.0158
18	G{CH4}	Trapped Methan	1	4	0	16.0426
19	G{C2H4}	Trapped Ethylene	2	4	0	28.0536
20	G{CH3OH}	Trapped Methan	1	4	1	32.042
21	Ash	Ash				
22	CO2	Carbon Dioxide	1	0	2	44.0098
23	H2	Hydrogen	0	2	0	2.0158
24	CO	Carbon Monoxide	1	0	1	28.0104
25	CH4	Methane	1	4	0	16.0426
26	CH2O	Formaldehyde	1	2	1	30.0262
27	C2H4	Ethylene	2	4	0	28.0536
28	C2H4O	Acetaldehyde	2	4	1	44.053
29	N2	Nitrogen				28.0134
30	CH3OH	Methanol	1	4	1	32.042
31	C2H5OH	Ethanol	2	6	1	46.0688
32	HCOOH	Formic Acid	1	2	2	46.0256
33	H2OG	Generated Wate	0	2	1	18.0152
34	HAA	Hydroxy-Acetalde	2	4	2	60.0524
35	GLYOX	Glyoxal	2	2	2	58.0366
36	C3H6O	Acetone/Propana	3	6	1	58.0798
37	HMFU	5-hydroxymethyl-	6	6	3	126.1116
38	LVG	Levoglucosan	6	10	5	162.142
39	XYLAN	Xylose Monomer	5	8	4	132.1158
40	COUMARYL	Paracoumaryl Alc	9	10	2	150.1768
41	PHENOL	Phenol	6	6	1	94.1128
42	FE2MACR	Sinapaldehyde	11	12	4	208.2134

Figure 48: Input Kinetic Constants Data Screen

Reaction #	1	A (1/s)	4E+13	E (kJ/mol)	188.3633	ΔH°_{R} (kJ/k	0	T exponen	0						
	Reactants					Products									
Componen	Stoich #	C	H	O	MM	Componen	Stoich #	C	H	O	MM	Fraction C	Fraction H	Fraction O	Elemental Balance Closure (%)
CELL	1	6	10	5	162.142	CELLA	1	6	10	5	162.142	6	10	5	C H O
	SUM	6	10	5								SUM 6	10	5	100 100 100

Reaction #	2	A (1/s)	5.00E+08	E (kJ/mol)	121.3897	ΔH°_{R} (kJ/k	620	T exponen	0						
	Reactants					Products									
Componen	Stoich #	C	H	O	MM	Componen	Stoich #	C	H	O	MM	Fraction C	Fraction H	Fraction O	
CELLA	1	6	10	5	162.142	HAA	0.8	2	4	2	60.0524	1.6	3.2	1.6	
						GLYOX	0.2	2	2	2	58.0366	0.4	0.4	0.4	
						C2H4O	0.1	2	4	1	44.053	0.2	0.4	0.1	
						HMFU	0.25	6	6	3	126.1116	1.5	1.5	0.75	
						C3H6O	0.3	3	6	1	58.0798	0.9	1.8	0.3	
						CO2	0.21	1	0	2	44.0098	0.21	0	0.42	
						H2	0.1	0	2	0	2.0158	0	0.2	0	
						CH2O	0.4	1	2	1	30.0262	0.4	0.8	0.4	
						CO	0.16	1	0	1	28.0104	0.16	0	0.16	
						CH4	0	1	4	0	16.0426	0	0	0	
						H2O	0.83	0	2	1	18.0152	0	1.66	0.83	
						HCOOH	0.02	1	2	2	46.0256	0.02	0.04	0.04	Elemental Balance Closure (%)
						Char	0.61	1	0	0	12.011	0.61	0	0	C H O
	SUM	6	10	5								SUM 6	10	5	100 100 100

Reaction #	3	A (1/s)	1.8	E (kJ/mol)	41.85852	ΔH°_{R} (kJ/k	364	T exponen	1						
	Reactants					Products									
Componen	Stoich #	C	H	O	MM	Componen	Stoich #	C	H	O	MM	Fraction C	Fraction H	Fraction O	Elemental Balance Closure (%)
CELLA	1	6	10	5	162.142	LVG	1	6	10	5	162.142	6	10	5	C H O
	SUM	6	10	5								SUM 6	10	5	100 100 100

Reaction #	4	A (1/s)	4.00E+07	E (kJ/mol)	129.7614	ΔH°_{R} (kJ/k	-1913	T exponen	0						
	Reactants					Products									
Componen	Stoich #	C	H	O	MM	Componen	Stoich #	C	H	O	MM	Fraction C	Fraction H	Fraction O	Elemental Balance Closure (%)
CELL	1	6	10	5	162.142	H2O	5	0	2	1	18.0152	0	10	5	C H O
						Char	6	1	0	0	12.011	6	0	0	100 100 100
	SUM	6	10	5								SUM 6	10	5	

Reaction #	5	A (1/s)	3.30E+09	E (kJ/mol)	129.7614	ΔH°_{R} (kJ/k	100	T exponen	0						
	Reactants					Products									
Componen	Stoich #	C	H	O	MM	Componen	Stoich #	C	H	O	MM	Fraction C	Fraction H	Fraction O	
HCE	1	5	8	4	132.1158	HCE1	0.4	5	8	4	132.1158	2	3.2	1.6	Elemental Balance Closure (%)
						HCE2	0.6	5	8	4	132.1158	3	4.8	2.4	C H O
	SUM	5	8	4								SUM 5	8	4	100 100 100

Figure 49: Stoichiometric Balance Check Screen

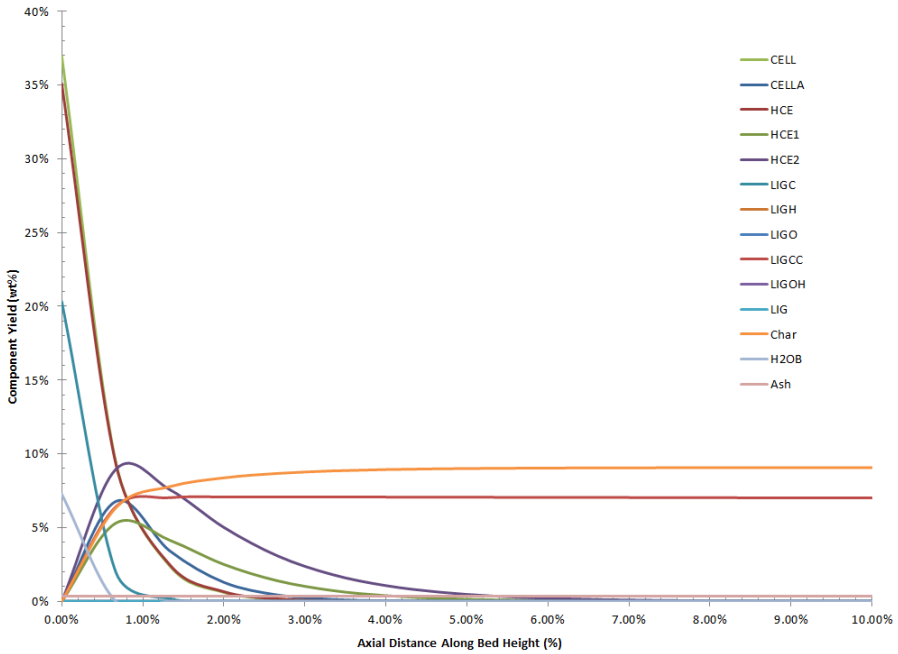

Figure 50: Yield Output Screen Example 1

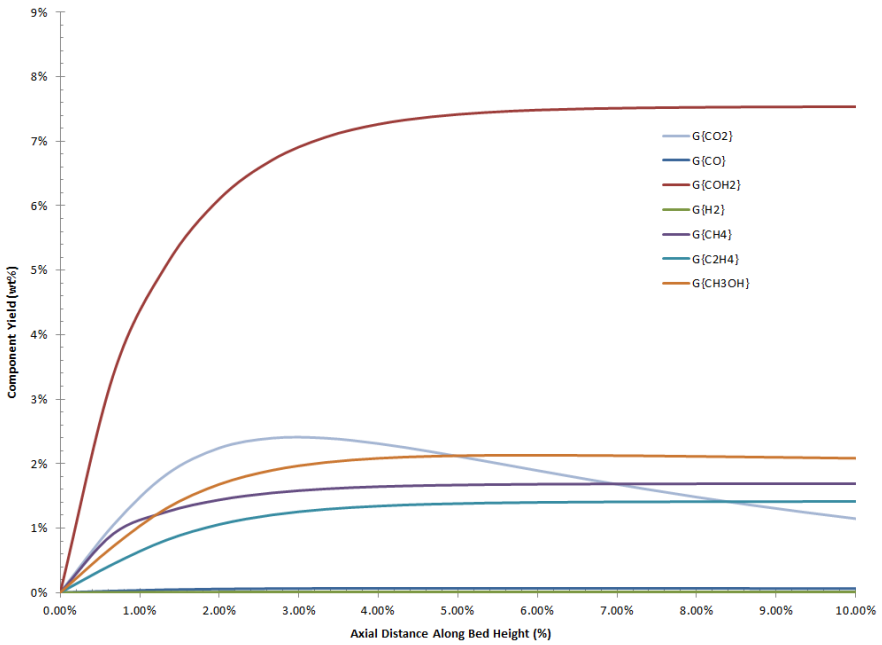

Figure 51: Yield Output Screen Example 2

Appendix B: Supplementary Material for Chapter 3

Table 19: Classification of Ranzi Mechanism Solid and Gas Components

Components of Biomass			
CELL	Cellulose ($C_6H_{10}O_5$)	**LIG**	Lignin ($C_{11}H_{12}O_4$)
CELLA	Activated Cellulose ($C_6H_{10}O_5$)	**Char**	Char (C)
HCE	Hemicellulose ($C_5H_8O_4$)	**H2OB**	Moisture in feed
HCE1	Activated Hemicellulose 1 ($C_5H_8O_4$)	**G{CO_2}**	Trapped Carbon Dioxide
HCE2	Activated Hemicellulose 2 ($C_5H_8O_4$)	**G{CO}**	Trapped Carbon Monoxide
LIGC	Lignin-C ($C_{15}H_{14}O_4$)	**G{CH_2O}**	Trapped Formaldehyde
LIGH	Lignin-H ($C_{22}H_{28}O_9$)	**G{H_2}**	Trapped Hydrogen
LIGO	Lignin-O ($C_{20}H_{22}O_{10}$)	**G{CH_4}**	Trapped Methane
LIGCC	Lignin-CC ($C_{15}H_{14}O_4$)	**G{C_2H_4}**	Trapped Ethylene
LIGOH	Lignin-OH ($C_{19}H_{22}O_8$)	**G{CH_3OH}**	Trapped Methanol
Components of Gas			
CO_2	Carbon Dioxide		
H_2	Hydrogen		
CO	Carbon Monoxide		
CH_4	Methane		
CH_2O	Formaldehyde		

C_2H_4	Ethylene
C_2H_4O	Acetaldehyde

Table 20: Moisture-Free Characterization and Classification of Modelled Bio-Oil Compounds

Compound ID	Compound Name	Structure	Chemical Formula	Classification
CH3OH	Methanol	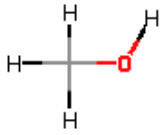	CH_3OH	Acids/Alcohols
C2H5OH	Ethanol	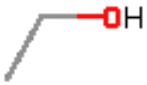	C_2H_6O	Acids/Alcohols
HCOOH	Formic Acid		CH_2O_2	Acids/Alcohols
C2H4O2	Hydroxy-acetaldehyde (Glycolaldehyde)		$C_2H_4O_2$	Acids/Alcohols
C2H2O2	Glyoxal		$C_2H_2O_2$	Ketones/Aldehydes
C3H6O	Acetone/Propanal		C_3H_6O	Ketones/Aldehydes
HMFU	5-hydroxymethyl-furfural	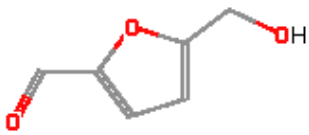	$C_6H_6O_3$	Furans
C6H10O5	Levoglucosan	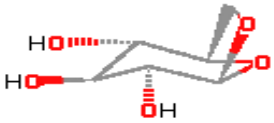	$C_6H_{10}O_5$	Sugars

XYLAN	Xylosan (1,4-anhydro-α-D-xylopyranose)	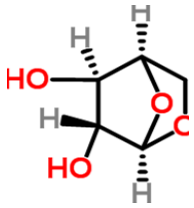	$C_5H_8O_4$	Sugars
COUMARYL	Paracoumaryl Alcohol	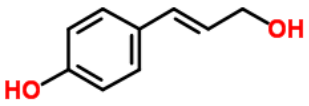	$C_9H_{10}O_2$	Phenolics
C6H6O	Phenol	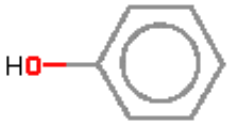	C_6H_6O	Phenolics
FE2MACR	Sinapaldehyde	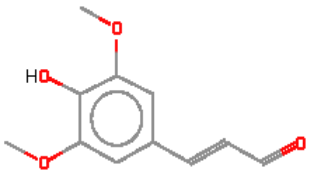	$C_{11}H_{12}O_4$	Syringols

The following equations are the species mass balances for the Ranzi mechanism:

CELL (Biomass Component) – Cellulose (C6H10O5)

$$In - Out + Generation - Consumption = Accumulation$$

$$F_{i0} - F_i \pm G_i = \frac{dm_i}{dt}$$

$$u_i \varepsilon_{bio} A_C C_{CELL}^z - u_i \varepsilon_{bio} A_C C_{CELL}^{z+\Delta z} - r_1 A_C \Delta z \varepsilon_{bio} - r_4 A_C \Delta z \varepsilon_{bio} = 0$$

$$C_{CELL}^{z+\Delta z} = C_{CELL}^z - \frac{(r_1 + r_4)\Delta z}{u_i} \quad \left[\frac{kg\ CELL}{m^3 biomass}\right]$$

$$C_{CELL}^{z+\Delta z} = C_{CELL}^z - \frac{(k_1 C_{CELL}^{z+\Delta z} + k_4 C_{CELL}^{z+\Delta z})\Delta z}{u_i} \quad \left[\frac{kg\ CELL}{m^3 biomass}\right]$$

$$C_{CELL}^{z+\Delta z} = \frac{C_{CELL}^z}{\left(1 + \frac{(k_1 + k_4)\Delta z}{u_i}\right)} \quad \left[\frac{kg\ CELL}{m^3 biomass}\right]$$

CELLA (Biomass Component) - Activated Cellulose (C6H10O5)

$$C_{CELLA}^{z+\Delta z} = \frac{C_{CELLA}^z + \frac{\left(\frac{sn_{CELLA}}{sn_{CELL}}\right)\left(\frac{MM_{CELLA}}{MM_{CELL}}\right) k_1 C_{CELL}^{z+\Delta z} \Delta z}{u_i}}{\left(1 + \frac{(k_2 + k_3)\Delta z}{u_i}\right)} \quad \left[\frac{kg\ CELLA}{m^3 biomass}\right]$$

HCE (Biomass Component) - Hemicellulose (C5H8O4)

$$C_{HCE}^{z+\Delta z} = \frac{C_{HCE}^z}{\left(1 + \frac{k_5 \Delta z}{u_i}\right)} \left[\frac{kg\ HCE}{m^3 biomass}\right]$$

HCE1 (Biomass Component) - Activated Hemicellulose 1 (C5H8O4)

$$C_{HCE1}^{z+\Delta z} = \frac{C_{HCE1}^z + \frac{(\frac{sn_{HCE1}}{sn_{HCE}})(\frac{MM_{HCE1}}{MM_{HCE}}) k_5 C_{HCE}^{z+\Delta z} \Delta z}{u_i}}{\left(1 + \frac{(k_6 + k_7 + k_8)\Delta z}{u_i}\right)} \quad \left[\frac{kg\ HCE1}{m^3 biomass}\right]$$

HCE2 (Biomass Component) - Activated Hemicellulose 2 (C5H8O4)

$$C_{HCE2}^{z+\Delta z} = \frac{C_{HCE2}^z + \frac{(\frac{sn_{HCE2}}{sn_{HCE}})(\frac{MM_{HCE2}}{MM_{HCE}}) k_5 C_{HCE}^{z+\Delta z} \Delta z}{u_i}}{\left(1 + \frac{k_9 \Delta z}{u_i}\right)} \quad \left[\frac{kg\ HCE2}{m^3 biomass}\right]$$

LIGC (Biomass Component) – Carbon-rich Lignin (C15H14O4)

$$C_{LIGC}^{z+\Delta z} = \frac{C_{LIGC}^{z}}{\left(1+\frac{k_{10}\Delta z}{u_i}\right)} \qquad \left[\frac{kg\ LIGC}{m^3 biomass}\right]$$

LIGH (Biomass Component) – Hydrogen-rich Lignin (C22H28O9)

$$C_{LIGH}^{z+\Delta z} = \frac{C_{LIGH}^{z}}{\left(1+\frac{k_{11}\Delta z}{u_i}\right)} \qquad \left[\frac{kg\ LIGH}{m^3 biomass}\right]$$

LIGO (Biomass Component) – Oxygen-rich Lignin (C20H22O10)

$$C_{LIGO}^{z+\Delta z} = \frac{C_{LIGO}^{z}}{\left(1+\frac{k_{12}\Delta z}{u_i}\right)} \qquad \left[\frac{kg\ LIGO}{m^3 biomass}\right]$$

LIGCC (Biomass Component) – Carbon-rich Lignin 2 (C15H14O4)

$$C_{LIGCC}^{z+\Delta z} = \frac{C_{LIGCC}^{z} + \frac{(\frac{sn_{LIGCC}}{sn_{LIGC}})(\frac{MM_{LIGCC}}{MM_{LIGC}})k_{10}C_{LIGC}^{z+\Delta z}\Delta z}{u_i}}{\left(1+\frac{k_{13}\Delta z}{u_i}\right)} \qquad \left[\frac{kg\ LIGCC}{m^3 biomass}\right]$$

LIGOH (Biomass Component) – OH-rich Lignin (C19H22O8)

$$C_{LIGOH}^{z+\Delta z} = \frac{C_{LIGOH}^{z} + \left(\left(\frac{sn_{LIGOH}}{sn_{LIGH}}\right)\left(\frac{MM_{LIGOH}}{MM_{LIGH}}\right)k_{11}C_{LIGH}^{z+\Delta z} + (\frac{sn_{LIGOH}}{sn_{LIGO}})\ (\frac{MM_{LIGOH}}{MM_{LIGO}})k_{12}C_{LIGO}^{z+\Delta z}\right)\left(\frac{\Delta z}{u_i}\right)}{\left(1+\frac{(k_{14}+k_{15})\Delta z}{u_i}\right)} \qquad \left[\frac{kg\ LIGOH}{m^3 biomass}\right]$$

LIG (Biomass Component) - Lignin (C11H12O4)

$$C_{LIG}^{z+\Delta z} = \frac{C_{LIG}^{z} + \frac{(\frac{sn_{LIG}}{sn_{LIGOH}})\ (\frac{MM_{LIG}}{MM_{LIGOH}})k_{14}C_{LIGOH}^{z+\Delta z}\Delta z}{u_i}}{\left(1+\frac{(k_{16}+k_{17}+k_{18})\Delta z}{u_i}\right)} \qquad \left[\frac{kg\ LIG}{m^3 biomass}\right]$$

Char (Biomass Component) – Char (C)

$$C_{Char}^{z+\Delta z} = C_{Char}^{z} + \left(\left(\frac{sn_{Char}}{sn_{CELLA}}\right)\left(\frac{MM_{Char}}{MM_{CELLA}}\right) k_2 C_{CELLA}^{z+\Delta z} + \left(\frac{sn_{Char}}{sn_{CELL}}\right)\left(\frac{MM_{Char}}{MM_{CELL}}\right) k_4 C_{CELL}^{z+\Delta z} + \left(\frac{sn_{Char}}{sn_{HCE1}}\right)\left(\frac{MM_{Char}}{MM_{HCE1}}\right) k_6 C_{HCE1}^{z+\Delta z} + \left(\frac{sn_{Char}}{sn_{HCE1}}\right)\left(\frac{MM_{Char}}{MM_{HCE1}}\right) k_7 C_{HCE1}^{z+\Delta z} + \left(\frac{sn_{Char}}{sn_{HCE2}}\right)\left(\frac{MM_{Char}}{MM_{HCE2}}\right) k_9 C_{HCE2}^{z+\Delta z} + \left(\frac{sn_{Char}}{sn_{LIGC}}\right)\left(\frac{MM_{Char}}{MM_{LIGC}}\right) k_{10} C_{LIGC}^{z+\Delta z} + \left(\frac{sn_{Char}}{sn_{LIGCC}}\right)\left(\frac{MM_{Char}}{MM_{LIGCC}}\right) k_{13} C_{LIGCC}^{z+\Delta z} + \left(\frac{sn_{Char}}{sn_{LIGOH}}\right)\left(\frac{MM_{Char}}{MM_{LIGOH}}\right) k_{14} C_{LIGOH}^{z+\Delta z} + \left(\frac{sn_{Char}}{sn_{LIGOH}}\right)\left(\frac{MM_{Char}}{MM_{LIGOH}}\right) k_{15} C_{LIGOH}^{z+\Delta z} + \left(\frac{sn_{Char}}{sn_{LIG}}\right)\left(\frac{MM_{Char}}{MM_{LIG}}\right) k_{17} C_{LIG}^{z+\Delta z} + \left(\frac{sn_{Char}}{sn_{LIG}}\right)\left(\frac{MM_{Char}}{MM_{LIG}}\right) k_{18} C_{LIG}^{z+\Delta z} \right) \left(\frac{\Delta z}{u_i}\right) \left[\frac{kg\ Char}{m^3 biomass}\right]$$

H2OB (Biomass Component) – Moisture

$$C_{H2OB}^{z+\Delta z} = \frac{C_{H2OB}^{z}}{\left(1 + \frac{k_{26}\Delta z}{u_i}\right)} \qquad \left[\frac{kg\ H2OB}{m^3 biomass}\right]$$

G{CO2} (Biomass Component) – Trapped Carbon Dioxide

$$C_{G\{CO2\}}^{z+\Delta z} = \frac{C_{G\{CO2\}}^{z} + \left(\begin{array}{l} \left(\frac{sn_{G\{CO2\}}}{sn_{HCE1}}\right)\left(\frac{MM_{G\{CO2\}}}{MM_{HCE1}}\right) k_6 C_{HCE1}^{z+\Delta z} \\ + \left(\frac{sn_{G\{CO2\}}}{sn_{HCE1}}\right)\left(\frac{MM_{G\{CO2\}}}{MM_{HCE1}}\right) k_7 C_{HCE1}^{z+\Delta z} \\ + \left(\frac{sn_{G\{CO2\}}}{sn_{HCE2}}\right)\left(\frac{MM_{G\{CO2\}}}{MM_{HCE2}}\right) k_9 C_{HCE2}^{z+\Delta z} \\ + \left(\frac{sn_{G\{CO2\}}}{sn_{LIGO}}\right)\left(\frac{MM_{G\{CO2\}}}{MM_{LIGO}}\right) k_{12} C_{LIGO}^{z+\Delta z} \end{array} \right) \left(\frac{\Delta z}{u_i}\right)}{\left(1 + \frac{k_{19}\Delta z}{u_i}\right)} \left[\frac{kg\ G\{CO2\}}{m^3 biomass}\right]$$

G{CO} (Biomass Component) – Trapped Carbon Monoxide

$$C_{G\{CO\}}^{z+\Delta z} = C_{G\{CO\}}^{z} + \left(\begin{array}{l} \left(\frac{sn_{G\{CO\}}}{sn_{HCE1}}\right)\left(\frac{MM_{G\{CO\}}}{MM_{HCE1}}\right) k_7 C_{HCE1}^{z+\Delta z} + \left(\frac{sn_{G\{CO\}}}{sn_{LIGCC}}\right)\left(\frac{MM_{G\{CO\}}}{MM_{LIGCC}}\right) k_{13} C_{LIGCC}^{z+\Delta z} \\ + \left(\frac{sn_{G\{CO\}}}{sn_{LIGOH}}\right)\left(\frac{MM_{G\{CO\}}}{MM_{LIGOH}}\right) k_{14} C_{LIGOH}^{z+\Delta z} + \left(\frac{sn_{G\{CO\}}}{sn_{LIGOH}}\right)\left(\frac{MM_{G\{CO\}}}{MM_{LIGOH}}\right) k_{15} C_{LIGOH}^{z+\Delta z} \\ + \left(\frac{sn_{G\{CO\}}}{sn_{LIG}}\right)\left(\frac{MM_{G\{CO\}}}{MM_{LIG}}\right) k_{17} C_{LIG}^{z+\Delta z} + \left(\frac{sn_{G\{CO\}}}{sn_{LIG}}\right)\left(\frac{MM_{G\{CO\}}}{MM_{LIG}}\right) k_{18} C_{LIG}^{z+\Delta z} \end{array} \right) \left(\frac{\Delta z}{u_i}\right)}{\left(1 + \frac{k_{20}\Delta z}{u_i}\right)} \left[\frac{kg\ G\{CO\}}{m^3 biomass}\right]$$

G{COH2} (Biomass Component) – Trapped Formaldehyde

$$C_{G\{COH2\}}^{z+\Delta z} = \frac{C_{G\{COH2\}}^{z} + \left(\begin{array}{l} \left(\frac{sn_{G\{COH2\}}}{sn_{HCE1}}\right)\left(\frac{MM_{G\{COH2\}}}{MM_{HCE1}}\right) k_6 C_{HCE1}^{z+\Delta z} \\ + \left(\frac{sn_{G\{COH2\}}}{sn_{HCE1}}\right)\left(\frac{MM_{G\{COH2\}}}{MM_{HCE1}}\right) k_7 C_{HCE1}^{z+\Delta z} \\ + \left(\frac{sn_{G\{COH2\}}}{sn_{HCE2}}\right)\left(\frac{MM_{G\{COH2\}}}{MM_{HCE2}}\right) k_9 C_{HCE2}^{z+\Delta z} \\ + \left(\frac{sn_{G\{COH2\}}}{sn_{LIGC}}\right)\left(\frac{MM_{G\{COH2\}}}{MM_{LIGC}}\right) k_{10} C_{LIGC}^{z+\Delta z} \\ + \left(\frac{sn_{G\{COH2\}}}{sn_{LIGCC}}\right)\left(\frac{MM_{G\{COH2\}}}{MM_{LIGCC}}\right) k_{13} C_{LIGCC}^{z+\Delta z} \\ + \left(\frac{sn_{G\{COH2\}}}{sn_{LIGOH}}\right)\left(\frac{MM_{G\{COH2\}}}{MM_{LIGOH}}\right) k_{14} C_{LIGOH}^{z+\Delta z} \\ + \left(\frac{sn_{G\{COH2\}}}{sn_{LIGOH}}\right)\left(\frac{MM_{G\{COH2\}}}{MM_{LIGOH}}\right) k_{15} C_{LIGOH}^{z+\Delta z} \\ + \left(\frac{sn_{G\{COH2\}}}{sn_{LIG}}\right)\left(\frac{MM_{G\{COH2\}}}{MM_{LIG}}\right) k_{17} C_{LIG}^{z+\Delta z} \\ + \left(\frac{sn_{G\{COH2\}}}{sn_{LIG}}\right)\left(\frac{MM_{G\{COH2\}}}{MM_{LIG}}\right) k_{18} C_{LIG}^{z+\Delta z} \end{array} \right)\left(\frac{\Delta z}{u_i}\right)}{\left(1 + \frac{k_{21}\Delta z}{u_i}\right)} \left[\frac{kg\ G\{COH2\}}{m^3 biomass}\right]$$

G{H2} (Biomass Component) – Trapped Hydrogen

$$C_{G\{H2\}}^{z+\Delta z} = \frac{C_{G\{H2\}}^{z} + \left(\begin{array}{l} \left(\frac{sn_{G\{H2\}}}{sn_{HCE1}}\right)\left(\frac{MM_{G\{H2\}}}{MM_{HCE1}}\right) k_6 C_{HCE1}^{z+\Delta z} \\ + \left(\frac{sn_{G\{H2\}}}{sn_{LIGOH}}\right)\left(\frac{MM_{G\{H2\}}}{MM_{LIGOH}}\right) k_{14} C_{LIGOH}^{z+\Delta z} \\ + \left(\frac{sn_{G\{H2\}}}{sn_{LIGOH}}\right)\left(\frac{MM_{G\{H2\}}}{MM_{LIGOH}}\right) k_{15} C_{LIGOH}^{z+\Delta z} \end{array} \right)\left(\frac{\Delta z}{u_i}\right)}{\left(1 + \frac{k_{22}\Delta z}{u_i}\right)} \left[\frac{kg\ G\{H2\}}{m^3 biomass}\right]$$

G{CH4} (Biomass Component) – Trapped Methane

$$C_{G\{CH4\}}^{z+\Delta z} = \frac{C_{G\{CH4\}}^{z} + \left(\begin{array}{l} \left(\frac{sn_{G\{CH4\}}}{sn_{HCE1}}\right)\left(\frac{MM_{G\{CH4\}}}{MM_{HCE1}}\right) k_6 C_{HCE1}^{z+\Delta z} \\ + \left(\frac{sn_{G\{CH4\}}}{sn_{HCE1}}\right)\left(\frac{MM_{G\{CH4\}}}{MM_{HCE1}}\right) k_7 C_{HCE1}^{z+\Delta z} \\ + \left(\frac{sn_{G\{CH4\}}}{sn_{HCE2}}\right)\left(\frac{MM_{G\{CH4\}}}{MM_{HCE2}}\right) k_9 C_{HCE2}^{z+\Delta z} \\ + \left(\frac{sn_{G\{CH4\}}}{sn_{LIGC}}\right)\left(\frac{MM_{G\{CH4\}}}{MM_{LIGC}}\right) k_{10} C_{LIGC}^{z+\Delta z} \\ + \left(\frac{sn_{G\{CH4\}}}{sn_{LIGCC}}\right)\left(\frac{MM_{G\{CH4\}}}{MM_{LIGCC}}\right) k_{13} C_{LIGCC}^{z+\Delta z} \\ + \left(\frac{sn_{G\{CH4\}}}{sn_{LIGOH}}\right)\left(\frac{MM_{G\{CH4\}}}{MM_{LIGOH}}\right) k_{14} C_{LIGOH}^{z+\Delta z} \\ + \left(\frac{sn_{G\{CH4\}}}{sn_{LIGOH}}\right)\left(\frac{MM_{G\{CH4\}}}{MM_{LIGOH}}\right) k_{15} C_{LIGOH}^{z+\Delta z} \\ + \left(\frac{sn_{G\{CH4\}}}{sn_{LIG}}\right)\left(\frac{MM_{G\{CH4\}}}{MM_{LIG}}\right) k_{17} C_{LIG}^{z+\Delta z} \\ + \left(\frac{sn_{G\{CH4\}}}{sn_{LIG}}\right)\left(\frac{MM_{G\{CH4\}}}{MM_{LIG}}\right) k_{18} C_{LIG}^{z+\Delta z} \end{array} \right) \left(\frac{\Delta z}{u_i}\right)}{\left(1 + \frac{k_{23}\Delta z}{u_i}\right)} \left[\frac{kg\ G\{CH4\}}{m^3 biomass}\right]$$

G{C2H4} (Biomass Component) – Trapped Ethylene

$$C_{G\{C2H4\}}^{z+\Delta z} = \frac{C_{G\{C2H4\}}^{z} + \left(\begin{array}{l} \left(\frac{sn_{G\{C2H4\}}}{sn_{HCE1}}\right)\left(\frac{MM_{G\{C2H4\}}}{MM_{HCE1}}\right) k_7 C_{HCE1}^{z+\Delta z} \\ + \left(\frac{sn_{G\{C2H4\}}}{sn_{HCE2}}\right)\left(\frac{MM_{G\{C2H4\}}}{MM_{HCE2}}\right) k_9 C_{HCE2}^{z+\Delta z} \\ + \left(\frac{sn_{G\{C2H4\}}}{sn_{LIGCC}}\right)\left(\frac{MM_{G\{C2H4\}}}{MM_{LIGCC}}\right) k_{13} C_{LIGCC}^{z+\Delta z} \\ + \left(\frac{sn_{G\{C2H4\}}}{sn_{LIGOH}}\right)\left(\frac{MM_{G\{C2H4\}}}{MM_{LIGOH}}\right) k_{14} C_{LIGOH}^{z+\Delta z} \\ + \left(\frac{sn_{G\{C2H4\}}}{sn_{LIGOH}}\right)\left(\frac{MM_{G\{C2H4\}}}{MM_{LIGOH}}\right) k_{15} C_{LIGOH}^{z+\Delta z} \\ + \left(\frac{sn_{G\{C2H4\}}}{sn_{LIG}}\right)\left(\frac{MM_{G\{C2H4\}}}{MM_{LIG}}\right) k_{17} C_{LIG}^{z+\Delta z} \\ + \left(\frac{sn_{G\{C2H4\}}}{sn_{LIG}}\right)\left(\frac{MM_{G\{C2H4\}}}{MM_{LIG}}\right) k_{18} C_{LIG}^{z+\Delta z} \end{array} \right) \left(\frac{\Delta z}{u_i}\right)}{\left(1 + \frac{k_{24}\Delta z}{u_i}\right)} \left[\frac{kg\ G\{C2H4\}}{m^3 biomass}\right]$$

G{CH3OH} (Biomass Component) – Trapped Methanol

$$C_{G\{CH3OH\}}^{z+\Delta z} = \frac{C_{G\{CH3OH\}}^{z} + \left(\begin{array}{c} \left(\frac{sn_{G\{CH3OH\}}}{sn_{HCE1}}\right)\left(\frac{MM_{G\{CH3OH\}}}{MM_{HCE1}}\right) k_6 C_{HCE1}^{z+\Delta z} \\ + \left(\frac{sn_{G\{CH3OH\}}}{sn_{HCE2}}\right)\left(\frac{MM_{G\{CH3OH\}}}{MM_{HCE2}}\right) k_9 C_{HCE2}^{z+\Delta z} \\ + \left(\frac{sn_{G\{CH3OH\}}}{sn_{LIGOH}}\right)\left(\frac{MM_{G\{CH3OH\}}}{MM_{LIGOH}}\right) k_{14} C_{LIGOH}^{z+\Delta z} \\ + \left(\frac{sn_{G\{CH3OH\}}}{sn_{LIGOH}}\right)\left(\frac{MM_{G\{CH3OH\}}}{MM_{LIGOH}}\right) k_{15} C_{LIGOH}^{z+\Delta z} \\ + \left(\frac{sn_{G\{CH3OH\}}}{sn_{LIG}}\right)\left(\frac{MM_{G\{CH3OH\}}}{MM_{LIG}}\right) k_{18} C_{LIG}^{z+\Delta z} \end{array} \right)\left(\frac{\Delta z}{u_i}\right)}{\left(1 + \frac{k_{25}\Delta z}{u_i}\right)} \left[\frac{kg\ G\{CH3OH\}}{m^3 biomass}\right]$$

CO2 (Gas Component) – Carbon Dioxide

$$C_{CO2}^{z+\Delta z} = C_{CO2}^{z} + \left(\begin{array}{c} \left(\frac{sn_{CO2}}{sn_{CELLA}}\right)\left(\frac{MM_{CO2}}{MM_{CELLA}}\right) k_2 C_{CELLA}^{z+\Delta z} \\ + \left(\frac{sn_{CO2}}{sn_{HCE1}}\right)\left(\frac{MM_{CO2}}{MM_{HCE1}}\right) k_6 C_{HCE1}^{z+\Delta z} \\ + \left(\frac{sn_{CO2}}{sn_{HCE1}}\right)\left(\frac{MM_{CO2}}{MM_{HCE1}}\right) k_7 C_{HCE1}^{z+\Delta z} \\ + \left(\frac{sn_{CO2}}{sn_{HCE2}}\right)\left(\frac{MM_{CO2}}{MM_{HCE2}}\right) k_9 C_{HCE2}^{z+\Delta z} \\ + \left(\frac{sn_{CO2}}{sn_{LIGOH}}\right)\left(\frac{MM_{CO2}}{MM_{LIGOH}}\right) k_{14} C_{LIGOH}^{z+\Delta z} \\ + \left(\frac{sn_{CO2}}{sn_{G\{CO2\}}}\right)\left(\frac{MM_{CO2}}{MM_{G\{CO2\}}}\right) k_{19} C_{G\{CO2\}}^{z+\Delta z} \end{array} \right)\left(\frac{\Delta z}{u_i}\right)\left(\frac{\varepsilon_{bio}}{\varepsilon_{gas}}\right) \left[\frac{kg\ CO2}{m^3 gas}\right]$$

H2 (Gas Component) - Hydrogen

$$C_{H2}^{z+\Delta z} = C_{H2}^{z} + \left(\begin{array}{c} \left(\frac{sn_{H2}}{sn_{CELLA}}\right)\left(\frac{MM_{H2}}{MM_{CELLA}}\right) k_2 C_{CELLA}^{z+\Delta z} \\ + \left(\frac{sn_{CO2}}{sn_{G\{COH2\}}}\right)\left(\frac{MM_{CO2}}{MM_{G\{COH2\}}}\right) k_{21} C_{G\{COH2\}}^{z+\Delta z} \\ + \left(\frac{sn_{CO2}}{sn_{G\{H2\}}}\right)\left(\frac{MM_{CO2}}{MM_{G\{H2\}}}\right) k_{22} C_{G\{H2\}}^{z+\Delta z} \end{array} \right)\left(\frac{\Delta z}{u_i}\right)\left(\frac{\varepsilon_{bio}}{\varepsilon_{gas}}\right) \left[\frac{kg\ H2}{m^3 gas}\right]$$

CO (Gas Component) - Carbon Monoxide

$$C_{CO}^{z+\Delta z} = C_{CO}^{z} + \left(\begin{array}{c} \left(\frac{sn_{CO}}{sn_{CELLA}}\right)\left(\frac{MM_{CO}}{MM_{CELLA}}\right) k_2 C_{CELLA}^{z+\Delta z} \\ + \left(\frac{sn_{CO}}{sn_{HCE1}}\right)\left(\frac{MM_{CO}}{MM_{HCE1}}\right) k_6 C_{HCE1}^{z+\Delta z} \\ + \left(\frac{sn_{CO}}{sn_{HCE1}}\right)\left(\frac{MM_{CO}}{MM_{HCE1}}\right) k_7 C_{HCE1}^{z+\Delta z} \\ + \left(\frac{sn_{CO}}{sn_{HCE2}}\right)\left(\frac{MM_{CO}}{MM_{HCE2}}\right) k_9 C_{HCE2}^{z+\Delta z} \\ + \left(\frac{sn_{CO}}{sn_{LIGC}}\right)\left(\frac{MM_{CO}}{MM_{LIGC}}\right) k_{10} C_{LIGC}^{z+\Delta z} \\ + \left(\frac{sn_{CO}}{sn_{LIGCC}}\right)\left(\frac{MM_{CO}}{MM_{LIGCC}}\right) k_{13} C_{LIGCC}^{z+\Delta z} \\ + \left(\frac{sn_{CO}}{sn_{LIGOH}}\right)\left(\frac{MM_{CO}}{MM_{LIGOH}}\right) k_{14} C_{LIGOH}^{z+\Delta z} \\ + \left(\frac{sn_{CO}}{sn_{LIGOH}}\right)\left(\frac{MM_{CO}}{MM_{LIGOH}}\right) k_{15} C_{LIGOH}^{z+\Delta z} \\ + \left(\frac{sn_{CO}}{sn_{LIG}}\right)\left(\frac{MM_{CO}}{MM_{LIG}}\right) k_{17} C_{LIG}^{z+\Delta z} \\ + \left(\frac{sn_{CO}}{sn_{LIG}}\right)\left(\frac{MM_{CO}}{MM_{LIG}}\right) k_{18} C_{LIG}^{z+\Delta z} \\ + \left(\frac{sn_{CO}}{sn_{G\{CO\}}}\right)\left(\frac{MM_{CO}}{MM_{G\{CO\}}}\right) k_{20} C_{G\{CO\}}^{z+\Delta z} \\ + \left(\frac{sn_{CO}}{sn_{G\{COH2\}}}\right)\left(\frac{MM_{CO}}{MM_{G\{COH2\}}}\right) k_{21} C_{G\{COH2\}}^{z+\Delta z} \end{array} \right) \left(\frac{\Delta z}{u_i}\right)\left(\frac{\varepsilon_{bio}}{\varepsilon_{gas}}\right) \left[\frac{kg\ CO}{m^3 gas}\right]$$

CH4 (Gas Component) - Methane

$$C_{CH4}^{z+\Delta z} = C_{CH4}^{z} + \left(\begin{array}{c} \left(\frac{sn_{CH4}}{sn_{CELLA}}\right)\left(\frac{MM_{CH4}}{MM_{CELLA}}\right) k_2 C_{CELLA}^{z+\Delta z} \\ + \left(\frac{sn_{CH4}}{sn_{LIGOH}}\right)\left(\frac{MM_{CH4}}{MM_{LIGOH}}\right) k_{14} C_{LIGOH}^{z+\Delta z} \\ + \left(\frac{sn_{CH4}}{sn_{LIGOH}}\right)\left(\frac{MM_{CH4}}{MM_{LIGOH}}\right) k_{15} C_{LIGOH}^{z+\Delta z} \\ + \left(\frac{sn_{CH4}}{sn_{LIG}}\right)\left(\frac{MM_{CH4}}{MM_{LIG}}\right) k_{17} C_{LIG}^{z+\Delta z} \\ + \left(\frac{sn_{CH4}}{sn_{LIG}}\right)\left(\frac{MM_{CH4}}{MM_{LIG}}\right) k_{18} C_{LIG}^{z+\Delta z} \\ + \left(\frac{sn_{CH4}}{sn_{G\{CH4\}}}\right)\left(\frac{MM_{CH4}}{MM_{G\{CH4\}}}\right) k_{23} C_{G\{CH4\}}^{z+\Delta z} \end{array} \right) \left(\frac{\Delta z}{u_i}\right)\left(\frac{\varepsilon_{bio}}{\varepsilon_{gas}}\right) \left[\frac{kg\ CH4}{m^3 gas}\right]$$

CH2O (Gas Component) - Formaldehyde

$$C_{CH2O}^{z+\Delta z} = C_{CH2O}^{z} + \begin{pmatrix} \left(\frac{sn_{CH2O}}{sn_{CELLA}}\right)\left(\frac{MM_{CH2O}}{MM_{CELLA}}\right) k_2 C_{CELLA}^{z+\Delta z} \\ + \left(\frac{sn_{CH2O}}{sn_{HCE1}}\right)\left(\frac{MM_{CH2O}}{MM_{HCE1}}\right) k_6 C_{HCE1}^{z+\Delta z} \\ + \left(\frac{sn_{CH2O}}{sn_{HCE2}}\right)\left(\frac{MM_{CH2O}}{MM_{HCE2}}\right) k_9 C_{HCE2}^{z+\Delta z} \\ + \left(\frac{sn_{CH2O}}{sn_{LIGC}}\right)\left(\frac{MM_{CH2O}}{MM_{LIGC}}\right) k_{10} C_{LIGC}^{z+\Delta z} \\ + \left(\frac{sn_{CH2O}}{sn_{LIG}}\right)\left(\frac{MM_{CH2O}}{MM_{LIG}}\right) k_{17} C_{LIG}^{z+\Delta z} \\ + \left(\frac{sn_{CH2O}}{sn_{LIG}}\right)\left(\frac{MM_{CH2O}}{MM_{LIG}}\right) k_{18} C_{LIG}^{z+\Delta z} \end{pmatrix} \left(\frac{\Delta z}{u_i}\right)\left(\frac{\varepsilon_{bio}}{\varepsilon_{gas}}\right) \left[\frac{kg\ CH2O}{m^3 gas}\right]$$

C2H4 (Gas Component) - Ethylene

$$C_{C2H4}^{z+\Delta z} = C_{C2H4}^{z} + \begin{pmatrix} \left(\frac{sn_{C2H4}}{sn_{HCE1}}\right)\left(\frac{MM_{C2H4}}{MM_{HCE1}}\right) k_6 C_{HCE1}^{z+\Delta z} \\ + \left(\frac{sn_{C2H4}}{sn_{LIGC}}\right)\left(\frac{MM_{C2H4}}{MM_{LIGC}}\right) k_{10} C_{LIGC}^{z+\Delta z} \\ + \left(\frac{sn_{C2H4}}{sn_{G\{C2H4\}}}\right)\left(\frac{MM_{C2H4}}{MM_{G\{C2H4\}}}\right) k_{24} C_{G\{C2H4\}}^{z+\Delta z} \end{pmatrix} \left(\frac{\Delta z}{u_i}\right)\left(\frac{\varepsilon_{bio}}{\varepsilon_{gas}}\right) \left[\frac{kg\ C2H4}{m^3 gas}\right]$$

C2H4O (Gas Component) - Acetaldehyde

$$C_{C2H4O}^{z+\Delta z} = C_{C2H4O}^{z} + \begin{pmatrix} \left(\frac{sn_{C2H4O}}{sn_{CELLA}}\right)\left(\frac{MM_{C2H4O}}{MM_{CELLA}}\right) k_2 C_{CELLA}^{z+\Delta z} \\ + \left(\frac{sn_{C2H4O}}{sn_{LIG}}\right)\left(\frac{MM_{C2H4O}}{MM_{LIG}}\right) k_{17} C_{LIG}^{z+\Delta z} \end{pmatrix} \left(\frac{\Delta z}{u_i}\right)\left(\frac{\varepsilon_{bio}}{\varepsilon_{gas}}\right) \left[\frac{kg\ C2H4O}{m^3 gas}\right]$$

CH3OH (Tar Component) - Methanol

$$C_{CH3OH}^{z+\Delta z} = C_{CH3OH}^{z} + \begin{pmatrix} \left(\frac{sn_{CH3OH}}{sn_{HCE1}}\right)\left(\frac{MM_{CH3OH}}{MM_{HCE1}}\right) k_6 C_{HCE1}^{z+\Delta z} \\ + \left(\frac{sn_{CH3OH}}{sn_{LIGOH}}\right)\left(\frac{MM_{CH3OH}}{MM_{LIGOH}}\right) k_{14} C_{LIGOH}^{z+\Delta z} \\ + \left(\frac{sn_{CH3OH}}{sn_{LIG}}\right)\left(\frac{MM_{CH3OH}}{MM_{LIG}}\right) k_{17} C_{LIG}^{z+\Delta z} \\ + \left(\frac{sn_{CH3OH}}{sn_{G\{CH3OH\}}}\right)\left(\frac{MM_{CH3OH}}{MM_{G\{CH3OH\}}}\right) k_{25} C_{G\{CH3OH\}}^{z+\Delta z} \end{pmatrix} \left(\frac{\Delta z}{u_i}\right)\left(\frac{\varepsilon_{bio}}{\varepsilon_{gas}}\right) \left[\frac{kg\ CH3OH}{m^3 gas}\right]$$

C2H5OH (Tar Component) - Ethanol

$$C_{C2H5OH}^{z+\Delta z} = C_{C2H5OH}^{z} + \left(\begin{array}{l} \left(\frac{sn_{C2H5OH}}{sn_{HCE1}}\right)\left(\frac{MM_{C2H5OH}}{MM_{HCE1}}\right) k_6 C_{HCE1}^{z+\Delta z} \\ + \left(\frac{sn_{C2H5OH}}{sn_{HCE2}}\right)\left(\frac{MM_{C2H5OH}}{MM_{HCE2}}\right) k_9 C_{HCE1}^{z+\Delta z} \end{array} \right) \left(\frac{\Delta z}{u_i}\right)\left(\frac{\varepsilon_{bio}}{\varepsilon_{gas}}\right) \left[\frac{kg\ C2H5OH}{m^3 gas}\right]$$

HCOOH (Tar Component) – Formic Acid

$$C_{HCOOH}^{z+\Delta z} = C_{HCOOH}^{z} + \left(\begin{array}{l} \left(\frac{sn_{HCOOH}}{sn_{CELLA}}\right)\left(\frac{MM_{HCOOH}}{MM_{CELLA}}\right) k_2 C_{CELLA}^{z+\Delta z} \\ + \left(\frac{sn_{HCOOH}}{sn_{HCE1}}\right)\left(\frac{MM_{HCOOH}}{MM_{HCE1}}\right) k_6 C_{HCE1}^{z+\Delta z} \\ + \left(\frac{sn_{HCOOH}}{sn_{HCE1}}\right)\left(\frac{MM_{HCOOH}}{MM_{HCE1}}\right) k_7 C_{HCE1}^{z+\Delta z} \\ + \left(\frac{sn_{HCOOH}}{sn_{HCE2}}\right)\left(\frac{MM_{HCOOH}}{MM_{HCE2}}\right) k_9 C_{HCE2}^{z+\Delta z} \\ + \left(\frac{sn_{HCOOH}}{sn_{LIGOH}}\right)\left(\frac{MM_{HCOOH}}{MM_{LIGOH}}\right) k_{14} C_{LIGOH}^{z+\Delta z} \\ + \left(\frac{sn_{HCOOH}}{sn_{LIG}}\right)\left(\frac{MM_{HCOOH}}{MM_{LIG}}\right) k_{17} C_{LIG}^{z+\Delta z} \end{array} \right) \left(\frac{\Delta z}{u_i}\right)\left(\frac{\varepsilon_{bio}}{\varepsilon_{gas}}\right) \left[\frac{kg\ HCOOH}{m^3 gas}\right]$$

H2OG (Tar Component) – Generated Water

$$C_{H2OG}^{z+\Delta z} = C_{H2OG}^{z} + \left(\begin{array}{c} k_{26} C_{H2OB}^{z+\Delta z} \\ + \left(\frac{sn_{H2OG}}{sn_{CELLA}}\right)\left(\frac{MM_{H2OG}}{MM_{CELLA}}\right) k_2 C_{CELLA}^{z+\Delta z} \\ + \left(\frac{sn_{H2OG}}{sn_{CELL}}\right)\left(\frac{MM_{H2OG}}{MM_{CELL}}\right) k_4 C_{CELL}^{z+\Delta z} \\ + \left(\frac{sn_{H2OG}}{sn_{HCE1}}\right)\left(\frac{MM_{H2OG}}{MM_{HCE1}}\right) k_6 C_{HCE1}^{z+\Delta z} \\ + \left(\frac{sn_{H2OG}}{sn_{HCE1}}\right)\left(\frac{MM_{H2OG}}{MM_{HCE1}}\right) k_7 C_{HCE1}^{z+\Delta z} \\ + \left(\frac{sn_{H2OG}}{sn_{HCE2}}\right)\left(\frac{MM_{H2OG}}{MM_{HCE2}}\right) k_9 C_{HCE2}^{z+\Delta z} \\ + \left(\frac{sn_{H2OG}}{sn_{LIGC}}\right)\left(\frac{MM_{H2OG}}{MM_{LIGC}}\right) k_{10} C_{LIGC}^{z+\Delta z} \\ + \left(\frac{sn_{H2OG}}{sn_{LIGCC}}\right)\left(\frac{MM_{H2OG}}{MM_{LIGCC}}\right) k_{13} C_{LIGCC}^{z+\Delta z} \\ + \left(\frac{sn_{H2OG}}{sn_{LIGOH}}\right)\left(\frac{MM_{H2OG}}{MM_{LIGOH}}\right) k_{14} C_{LIGOH}^{z+\Delta z} \\ + \left(\frac{sn_{H2OG}}{sn_{LIGOH}}\right)\left(\frac{MM_{H2OG}}{MM_{LIGOH}}\right) k_{15} C_{LIGOH}^{z+\Delta z} \\ + \left(\frac{sn_{H2OG}}{sn_{LIG}}\right)\left(\frac{MM_{H2OG}}{MM_{LIG}}\right) k_{17} C_{LIG}^{z+\Delta z} \\ + \left(\frac{sn_{H2OG}}{sn_{LIG}}\right)\left(\frac{MM_{H2OG}}{MM_{LIG}}\right) k_{18} C_{LIG}^{z+\Delta z} \end{array} \right) \left(\frac{\Delta z}{u_i}\right)\left(\frac{\varepsilon_{bio}}{\varepsilon_{gas}}\right) \left[\frac{kg\ H2OG}{m^3 gas}\right]$$

HAA (Tar Component) – Hydroxy-Acetaldehyde (C2H4O2)

$$C_{HAA}^{z+\Delta z} = C_{HAA}^{z} + \left(\begin{array}{c} \left(\frac{sn_{HAA}}{sn_{CELLA}}\right)\left(\frac{MM_{HAA}}{MM_{CELLA}}\right) k_2 C_{CELLA}^{z+\Delta z} \\ + \left(\frac{sn_{HAA}}{sn_{HCE2}}\right)\left(\frac{MM_{HAA}}{MM_{HCE2}}\right) k_9 C_{HCE2}^{z+\Delta z} \\ + \left(\frac{sn_{HAA}}{sn_{LIGCC}}\right)\left(\frac{MM_{HAA}}{MM_{LIGCC}}\right) k_{13} C_{LIGCC}^{z+\Delta z} \end{array} \right) \left(\frac{\Delta z}{u_i}\right)\left(\frac{\varepsilon_{bio}}{\varepsilon_{gas}}\right) \left[\frac{kg\ HAA}{m^3 gas}\right]$$

GLYOX (Tar Component) - Glyoxal (C2H2O2)

$$C_{GLYOX}^{z+\Delta z} = C_{GLYOX}^{z} + \left(\left(\frac{sn_{GLYOX}}{sn_{CELLA}}\right)\left(\frac{MM_{GLYOX}}{MM_{CELLA}}\right) k_2 C_{CELLA}^{z+\Delta z}\right)\left(\frac{\Delta z}{u_i}\right)\left(\frac{\varepsilon_{bio}}{\varepsilon_{gas}}\right) \left[\frac{kg\ GLYOX}{m^3 gas}\right]$$

C3H6O (Tar Component) - Acetone/Propanal

$$C_{C3H6O}^{z+\Delta z} = C_{C3H6O}^{z} + \left(\left(\frac{sn_{C3H6O}}{sn_{CELLA}}\right)\left(\frac{MM_{C3H6O}}{MM_{CELLA}}\right) k_2 C_{CELLA}^{z+\Delta z}\right)\left(\frac{\Delta z}{u_i}\right)\left(\frac{\varepsilon_{bio}}{\varepsilon_{gas}}\right) \left[\frac{kg\ C3H6O}{m^3 gas}\right]$$

HMFU (Tar Component) - 5-hydroxymethyl-furfural (C6H6O3)

$$C_{HMFU}^{z+\Delta z} = C_{HMFU}^{z} + \left(\left(\frac{sn_{HMFU}}{sn_{CELLA}}\right)\left(\frac{MM_{HMFU}}{MM_{CELLA}}\right)k_2 C_{CELLA}^{z+\Delta z}\right)\left(\frac{\Delta z}{u_i}\right)\left(\frac{\varepsilon_{bio}}{\varepsilon_{gas}}\right)\ \left[\frac{kg\ HMFU}{m^3 gas}\right]$$

LVG (Tar Component) - Levoglucosan (C6H10O5)

$$C_{LVG}^{z+\Delta z} = C_{LVG}^{z} + \left(\left(\frac{sn_{LVG}}{sn_{CELLA}}\right)\left(\frac{MM_{LVG}}{MM_{CELLA}}\right)k_3 C_{CELLA}^{z+\Delta z}\right)\left(\frac{\Delta z}{u_i}\right)\left(\frac{\varepsilon_{bio}}{\varepsilon_{gas}}\right)\ \left[\frac{kg\ LVG}{m^3 gas}\right]$$

XYLAN (Tar Component) – Xylose Monomer (C5H8O4)

$$C_{XYLAN}^{z+\Delta z} = C_{XYLAN}^{z} + \left(\left(\frac{sn_{XYLAN}}{sn_{HCE1}}\right)\left(\frac{MM_{XYLAN}}{MM_{HCE1}}\right)k_8 C_{HCE1}^{z+\Delta z}\right)\left(\frac{\Delta z}{u_i}\right)\left(\frac{\varepsilon_{bio}}{\varepsilon_{gas}}\right)\ \left[\frac{kg\ XYLAN}{m^3 gas}\right]$$

COUMARYL (Tar Component) – Paracoumaryl Alcohol (C9H10O2)

$$C_{COUMARYL}^{z+\Delta z} = C_{COUMARYL}^{z} + \left(\begin{array}{l}\left(\frac{sn_{COUMARYL}}{sn_{LIGC}}\right)\left(\frac{MM_{COUMARYL}}{MM_{LIGC}}\right)k_{10} C_{LIGC}^{z+\Delta z} \\ +\left(\frac{sn_{COUMARYL}}{sn_{LIGCC}}\right)\left(\frac{MM_{COUMARYL}}{MM_{LIGCC}}\right)k_{13} C_{LIGCC}^{z+\Delta z}\end{array}\right)\left(\frac{\Delta z}{u_i}\right)\left(\frac{\varepsilon_{bio}}{\varepsilon_{gas}}\right)\ \left[\frac{kg\ COUMARYL}{m^3 gas}\right.$$

PHENOL (Tar Component) - Phenol (C6H6O)

$$C_{PHENOL}^{z+\Delta z} = C_{PHENOL}^{z} + \left(\begin{array}{l}\left(\frac{sn_{PHENOL}}{sn_{LIGC}}\right)\left(\frac{MM_{PHENOL}}{MM_{LIGC}}\right)k_{10} C_{LIGC}^{z+\Delta z} \\ +\left(\frac{sn_{PHENOL}}{sn_{LIGCC}}\right)\left(\frac{MM_{PHENOL}}{MM_{LIGCC}}\right)k_{13} C_{LIGCC}^{z+\Delta z}\end{array}\right)\left(\frac{\Delta z}{u_i}\right)\left(\frac{\varepsilon_{bio}}{\varepsilon_{gas}}\right)\ \left[\frac{kg\ PHENOL}{m^3 gas}\right.$$

FE2MACR (Tar Component) – Sinapaldehyde (C11H12O4)

$$C_{FE2MACR}^{z+\Delta z} = C_{FE2MACR}^{z} + \left(\left(\frac{sn_{FE2MACR}}{sn_{LIG}}\right)\left(\frac{MM_{FE2MACR}}{MM_{LIG}}\right)k_{16} C_{LIG}^{z+\Delta z}\right)\left(\frac{\Delta z}{u_i}\right)\left(\frac{\varepsilon_{bio}}{\varepsilon_{gas}}\right)\ \left[\frac{kg\ FE2MACR}{m^3 gas}\right.$$